STRUCTURAL CONSIDERATIONS FOR SUPERHYDROPHOBIC AND SUPEROLEOPHOBIC SURFACES

A Dissertation
Presented to
The Academic Faculty

by

Lester Li

In Partial Fulfillment
Of the Requirements for the Degree
Doctor of Philosophy in the
School of Chemical and Biomolecular Engineering

Georgia Institute of Technology
December 2013

STRUCTURAL CONSIDERATIONS FOR SUPERHYDROPHOBIC AND SUPEROLEOPHOBIC SURFACES

Approved by:

Professor Victor Breedveld,
Co-Advisor
School of Chemical and Biomolecular
Engineering
Georgia Institute of Technology

Professor Carson Meredith
School of Chemical and Biomolecular
Engineering
Georgia Institute of Technology

Professor Dennis Hess, Co-Advisor
School of Chemical and Biomolecular
Engineering
Georgia Institute of Technology

Professor Preet Singh
School of Material Science and
Engineering
Georgia Institute of Technology

Professor Yulin Deng
School of Chemical and Biomolecular
Engineering
Georgia Institute of Technology

Date Approved: 22nd of July, 2013

ACKNOWLEDGEMENTS

First and foremost, I would like to thank my advisors Dr. Dennis Hess and Dr. Victor Breedveld, for their constant support of not only my work, but more importantly my ideas. There was never a point during my time at Georgia Tech where I did not feel that I could stop by their office and sort out my problems. I will forever be grateful of the knowledge and expertise that I have gained from their advising. I would also like to thank my committee members, Dr. Preet Sing, Dr. Yulin Deng and Dr. Carson Meredith for their help both during and after our committee meetings.

Thanks to the Hess and Breeveld group members, Dr. Michael Casciato, Dr. Galit Levitin, Dr. Sonam Sherpa, Tae Seop Choi, Emily Peterson, Kyung Hee Oh and Sricharan Yarlagadda, for listening to my problems, and lending a helping hand whenever I needed it. Special thanks to Dr. Balamurali Balu, while our time at Georgia Tech only slightly overlapped, you were able to help get me quickly started on my thesis. I was very fortunate to have been the mentor of many talented, hardworking undergraduates. Adam Berry, Michael Hart, Justin Eisenberg, David Bentley and Sara Roethel, thanks for putting up with me and helping me to develop as a leader.

To my friends, thanks for lending your ears in rough times and for the far too infrequent out of school get-togethers.

I would like to thank my family for their unwavering support of my desire to get a Ph.D. Mom and Dad, thanks for being the supportive parents that I needed to make it this far. Amanda, your talent was what I always aspired for, thanks for being a great sister to look up to. And finally, to my loving wife Beckie, absolutely none of this would have been possible without you.

TABLE OF CONTENTS

LIST OF TABLES

LIST OF FIGURES

SUMMARY

As a writing medium, cellulose based products have been a crucial component of civilization for hundreds of years. As society has evolved, paper has taken on many novel roles beyond a writing medium, becoming a mainstay for packaging and advertisement. Even more recently, paper has found further use in advanced applications such as microfluidics and biological test strips. The combination of biodegradability, low cost and worldwide abundance has thrust paper into these new endeavors. However, paper based products continue to remain hindered by the inherent hydrophilic and oleophilic properties of cellulose. In this thesis we utilize plasma based processes to create superhydrophobic paper. Superhydrophobicity is defined by a very high static water contact angle of $>150^{\circ}$ and requires the specific combination of low surface energy and physical surface roughness. An oxygen plasma is used to selectively etch the amorphous phase of cellulose and create nanoscale roughness. Subsequent plasma fluoropolymer deposition is used to attain a low surface energy. By printing wax dots onto these superhydrophobic paper substrates, microfluidic devices are created, capable of accurately and reproducibly collecting samples from a bulk liquid droplet. Further, it is demonstrated that the volume of fluid that is sampled from the bulk droplet can be controlled via contact angle hysteresis. The hysteresis of the wax dots is modified both physically, through surface roughening of the wax, and chemically by using waxes with different chemical compositions.

While superhydrophobic paper surfaces have been developed by several research groups and demonstrated applicability in fields such as disposable antibacterial surfaces, the oleophilicity of cellulose remains a major technological challenge. To attain

the same high contact angles that superhydrophobic surfaces exhibit with water, much stricter physical and chemical requirements must be satisfied. Physically, in order for a surface to be superoleophobic (i.e., exhibit oil contact angles >150°) the surface structures must have reentrant angles that are correctly spaced and sized. To attain the required spacing, the same plasma processing that was used to create superhydrophobic paper is combined with a solvent exchange during the paper forming process. This method modifies fiber-fiber hydrogen bonding and yielding increases in the spacing. Through these processing steps, paper substrates can be formed that exhibit contact angles >150° for multiple fluids: water, ethylene glycol, motor oil and *n*-hexadecane. While yielding high contact angles, the solvent processing step detrimentally affects the strength of the paper. In order to maintain strength and still achieve the desired fiber structure, another approach is pursued in which a porous, low weight layer of fibers is laminated on top of a regular paper sheet. This process increases the average roughness of the sheet, and in conjunction with the same plasma treatment, demonstrates a substantial increase in *n*-hexadecane contact angles over a standard piece of paper.

The effect of changes in surface chemistry on the superhydrophobicity of paper is also studied. Hydrophilic diamond-like-carbon is coated onto oxygen plasma etched paper. Although the surface coating is hydrophilic, a low hysteresis superhydrophobic surface is attained that is comparable to fluoropolymer coated surfaces. This suprising wetting behavior results from the formation of dual scale surface roughness after oxygen plasma etching, which is able to compensate for the less than ideal surface chemistry.

Applying the same fundamental knowledge gained from studies of superhydrophobic paper, superhydrophobic surfaces were created on stainless steel (304 and 316 grades). The stainless steels were etched in hydrofluoric acid, effectively roughening the surface and creating physical structure. Subsequently, a passivation step was

employed with nitric acid to restore the chemical passivity for which stainless steel is known. Finally, a plasma fluoropolymer deposition was used to coat the substrate and yield superhydrophobic stainless steel.

CHAPTER I

INTRODUCTION

Paper remains an essential material in modern day society. Primarily composed of wood fibers, paper is a renewable, biodegradable, inexpensive product that is manufactured and used worldwide. The term paper generally encompasses the whole gamut of products that are manufactured from cellulosic wood fibers, including linerboard, corrugated fiber board, newsprint and copy paper. Although it is a relatively mature product, modern technological advances have forced innovation in the paper industry. To meet the ever changing technical demands, different grades of paper have been optimized for strength, brightness, gloss, opacity and cost. The mass production of these grades has evolved into a diverse multi-billion dollar industry, extending paper well beyond its original use as a writing medium.

Industrially, paper is widely applied as a packaging material, providing primary containment while simultaneously acting as an advertising medium. Without further treatment, paper is extremely hydrophilic. Some applications, such as paper towels, take advantage of the strong absorptive properties afforded by capillary action. However, the absorption of water into the fiber web interferes with the hydrogen bonding between fibers, resulting in weakening of the bonds and, consequently, compromising the overall strength of the paper product. [1, 2] Excessive rapid wetting can cause the paper to fall apart before its job is complete. Even for paper applications that require high absorptivity, fibers are often treated with chemicals to control the hydrophilicity. While loss of strength may not be critical for disposable, single-use products, it is extremely detrimental for applications such as packaging, where strength is imperative. Paper packaging products are rated to withstand a certain amount of force

before failure. When wet, the sustainable force is greatly reduced, possibly leading to product damage. Moreover, paper is often also the face or advertising medium of products. With billions of dollars spent each year on advertising, companies do not want the printed images on packaging to run or deform when exposed to moisture. To mitigate these concerns, and others, the industry has been driven to design water resistant paper substrates.

A current technique used to increase water resistance is called sizing and involves the addition of chemicals during the paper making process to yield hydrophobic properties. [3, 4] Through modifications in hydrophobicity, companies are able to control the wicking of fluid into the paper. The degree to which a fluid wicks is a critical parameter in many printing techniques, because it determines the degree to which inks spread. [2] If the paper is made too hydrophobic, the ink will not absorb well into the paper; if it is too hydrophilic, the ink will spread excessively and leach beyond its intended area. Therefore, a significant amount of research has been carried out within the paper industry with the aim to control this spreading behavior. It has been reported that certain commercial grades of copy paper exhibit near hydrophobic properties as a result of sizing treatment alone. [5] Two technical approaches towards sizing exist: internal sizing, where the sizing agents are added to the wet pulp, and surface sizing, where the chemicals are added to the surface of the paper after it is dried. [6] The sizing agents, such as rosin, alkylketene dimer and alkyl succinic anhydride, are amphiphilic; their hydrophilic ends bond to the fiber, while the hydrophobic ends face outward, away from the surface. By coating fibers with these sizing agents, a non-polar layer is formed that hinders water penetration into the pores. Small concentrations of less than 0.5 wt.% (of the dried paper product) can modify the bulk hydrophobicity sufficiently to control the spreading of inks. By increasing the chemical loading, sized paper products can be used to prevent water

wicking in packaging, although these substrates are insufficiently hydrophobic to provide primary containment of liquids. Overall, the sizing of paper can only provide a marginal degree of water resistance, providing no protection against the effects of water vapor [7] or the complete submersion of paper in water. [8]

Applications in which paper acts as the primary fluid barrier demand higher water resistance. To further increase hydrophobicity, paper companies have applied wax and polymer coatings to their products. Use of both of these coatings requires relatively thick layers (>50 μm) [9] which in turn leads to high cost. If not properly removed, excess amounts of wax also build up when the coated paper is recycled, accumulating on heated rollers and eventually forcing a premature process shutdown for cleaning. As the paper industry continues to expand the use of recycled pulp in final products, this accumulation becomes a greater concern. Thus, coatings are still pursued that combine high water repellency with low cost and good recyclability. Paper with increased water resistance would enable value-added applications that are currently not feasible, for example in food packaging, self-cleaning packaging, and biomedical test and microfluidic devices. Superhydrophobic surface modification of paper products offers a unique solution to limitations in traditional paper products that would greatly expand the possible applications of paper into novel areas.

1.1 Superhydrophobic Surfaces

Superhydrophobic surfaces, modeled after the oft-mentioned self-cleaning properties of the lotus leaf, have a plethora of industrial applications, for example as anti-icing, fluid drag reducing, self-cleaning and stain-resistant surfaces. [10–17] superhydrophobic surfaces are defined as having a static contact angle of greater than 150°. In order to attain these elevated contact angles, surfaces require a specific combination of surface roughness and low surface energy. Commonly, fluoropolymers are used to satisfy the low surface energy condition. Many techniques exist to increase the

surface roughness, including plasma treatment [18], sol-gel methods [19], physical vapor deposition [20] and dip coating [21, 22]. Along with the multitude of deposition techniques, there exist an equally vast number of substrates that can be made superhydrophobic, including glass [23], metals [22, 24–26], silicon wafers [12, 20, 27–29], polymers [30, 31] and fabric [32]. However, the requirement of a high contact angle is not sufficient to fully describe the properties of the surface; it is also necessary to characterize the adhesion of liquids to the substrate. This property is commonly quantified through contact angle hysteresis measurements, which determine the difference between the advancing and the receding contact angles of a liquid interface when moving across the surface. In literature, superhydrophobic surfaces are commonly associated with low-adhesive properties, which cause water droplets to readily roll off the surface at low tilt angles. Nonetheless, researchers have fabricated surfaces with both low and high hysteresis properties, while still maintaining a static contact angle above 150°. To delineate between these classes of observed properties, we adopt a previously used terminology of sticky (contact angle hysteresis >10°) and roll-off (contact angle hysteresis >10°) superhydrophobic surfaces. [18]

The transition from a high to a low hysteresis superhydrophobic surface is associated with a transition from a Wenzel [33] to a Cassie-Baxter [34] wetting state. [35] In the Wenzel state, the droplet completely wets all features of the rough surface, creating a larger solid-liquid interface, whereas in the Cassie-Baxter state the droplet rests on trapped air pockets, minimizing direct surface interactions; both cases are depicted in Figure 1.1. More information regarding these wetting states can be found elsewhere. [10, 11, 13]

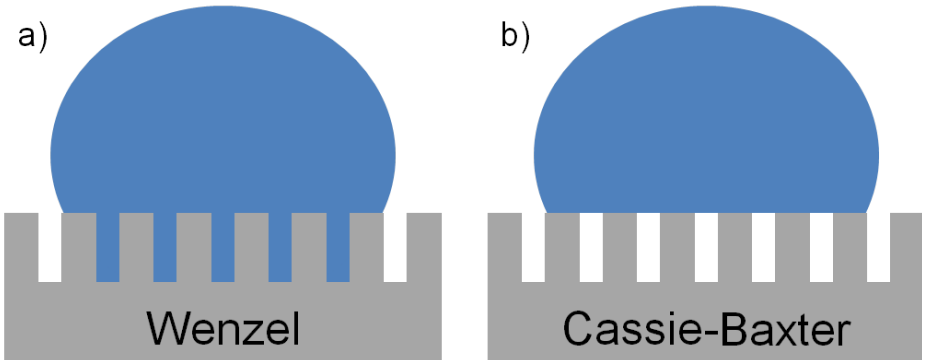

Figure 1.1: a) Wenzel and b) Cassie-Baxter wetting states

1.2 Fabrication of Superhydrophobic Paper

While relying on the same principles, superhydrophobic surfaces on paper and other cellulose-based products are distinctly different from surfaces formed on inorganic substrates such as silicon and metals. Cellulose's sensitivity to thermal and chemical damage restricts the techniques that can be applied to form superhydrophobic surfaces. The natural cellulose fibers in paper also impart a mechanical flexibility not commonly observed for inorganic superhydrophobic surfaces. Simultaneously, the fiber web creates a complex, randomly oriented structure dissimilar to the manufactured structures of many inorganic superhydrophobic substrates. Despite these differences, the creation of superhydrophobic paper requires the same fundamental, bio-inspired, combination of parameters as inorganic substrates: surface roughness and low surface energy. The overlapping network of wood fibers in untreated paper inherently contains the necessary micron-scale surface roughness, with fiber diameters in the range of 10-50 μm depending upon the wood type and species. [36] As a consequence, deposition of a thin layer of a low surface energy material onto an untreated paper substrate can yield a relatively high static contact angle (>140°). [37,38] However, due to the spacing of the fibers and the lack of small scale roughness, superhydrophobic properties (contact angle>150°) are not attained. To increase the

water contact angle and reduce adhesion, sub-micron and nano-scale roughness must be imparted to the fiber surfaces. As with inorganic substrates, the methods used for the incorporation of this roughness on paper can be divided into two categories, bottom-up and top-down techniques. [10] Bottom-up approaches invoke deposition of a secondary material to create the surface roughness, whereas top-down methods employ etching processes. Both types of techniques will be discussed in the following sections. In addition, we will highlight the challenges associated with fabrication of durable superhydrophobic paper surfaces, and characterization techniques that provide insight beyond the simple contact angle measurement.

1.2.1 Bottom-up Techniques

As previously stated, the fibers that compose paper substrates already create micro-scale roughness. In order to both increase the contact angle and decrease the hysteresis, roughness is required at a smaller scale. The addition of this roughness can occur through the deposition of particles or through in-situ growth of nanostructures. A major concern with both approaches is the bonding between the added material and the underlying fiber surface. Poorly bonded surface features will result in a mechanically weak structure that can easily be damaged and is unable to withstand wear. In order to deposit the required structures, the hydroxyl groups on cellulose surfaces provide readily accessible reactive sites for bonding chemical groups onto the wood fibers. The addition of material to create roughness can be carried out either in the pulping phase before the sheet is fabricated, or as a post-fabrication procedure after the paper is already formed. Both methods have their advantages and disadvantages. Depending on the chemical properties and surface coverage of the added materials that impart roughness, subsequent deposition of a low surface energy layer may be required to achieve superhydrophobicity.

1.2.1.1 Particle Deposition

Multi-layer deposition, or layer-by-layer deposition, was developed in the 1990s by Decher and Hong [39, 40] and recently has been applied to the fabrication of superhydrophobic surfaces. The layer-by-layer deposition technique provides a simple and inexpensive method of attaching thin layers of particles to a surface, without shape restrictions. Through the use of this method, Yang and Deng have achieved superhydrophobic properties on paper. [9] Their method utilizes a commercial linerboard made from unbleached kraft softwood fibers as substrate. By repeatedly dipping the prefabricated linerboard into a cationic polydiallyldimethylammonium chloride (polyDADMAC) solution and a silica particle suspension, a multilayer thin film of silica particles is formed. Chemical vapor deposition of 1H,1H,2H,2H-perfluorooctyltriethyoxysilane (POTS) was then performed to attain a lowered surface energy. The roughness added by the silica particles, along with the reduced surface energy from the fluoropolymer, yielded a static contact angle of 155° when 220 nm particles were used. The multilayer coated linerboard also exhibited low hysteresis, with a roll-off angle under 5°. The low hysteresis superhydrophobic properties provided by the particle and fluoropolymer deposition increased the moisture resistance in a humid environment, as illustrated in Figure 1.2a). Samples of untreated paper (UP), hydrophobic paper treated with only POTS (HP) and superhydrophobic paper treated with both silica and POTS (SHP) were placed in a humidity chamber. After exposure, the moisture content of the SHP and HP samples was dramatically lower than that of the UP samples at high humidity. Furthermore, Figure 1.2b) shows that the treated samples retained their tensile strength at high relative humidity. The demonstrated resistance to moisture is due to the complete fiber coverage from the chemical vapor deposition of POTS. Since water was unable to penetrate into the fiber web and interfere with fiber-fiber bonding, the effect of moisture on the tensile strength in the HP and SHP samples is reduced. These results indicate that even

with increased ambient moisture and water exposure, the linerboard samples maintain their structural integrity. Thus, layer-by-layer deposition of particles in combination with fluoropolymer deposition can create superhydrophobic surfaces on paper and increase resistance to liquid water and water vapor. However, questions still remain regarding the durability of the added surface roughness and the industrial applicability of process, which is energy and time intensive; these issues must be addressed before the method can be implemented by the paper industry.

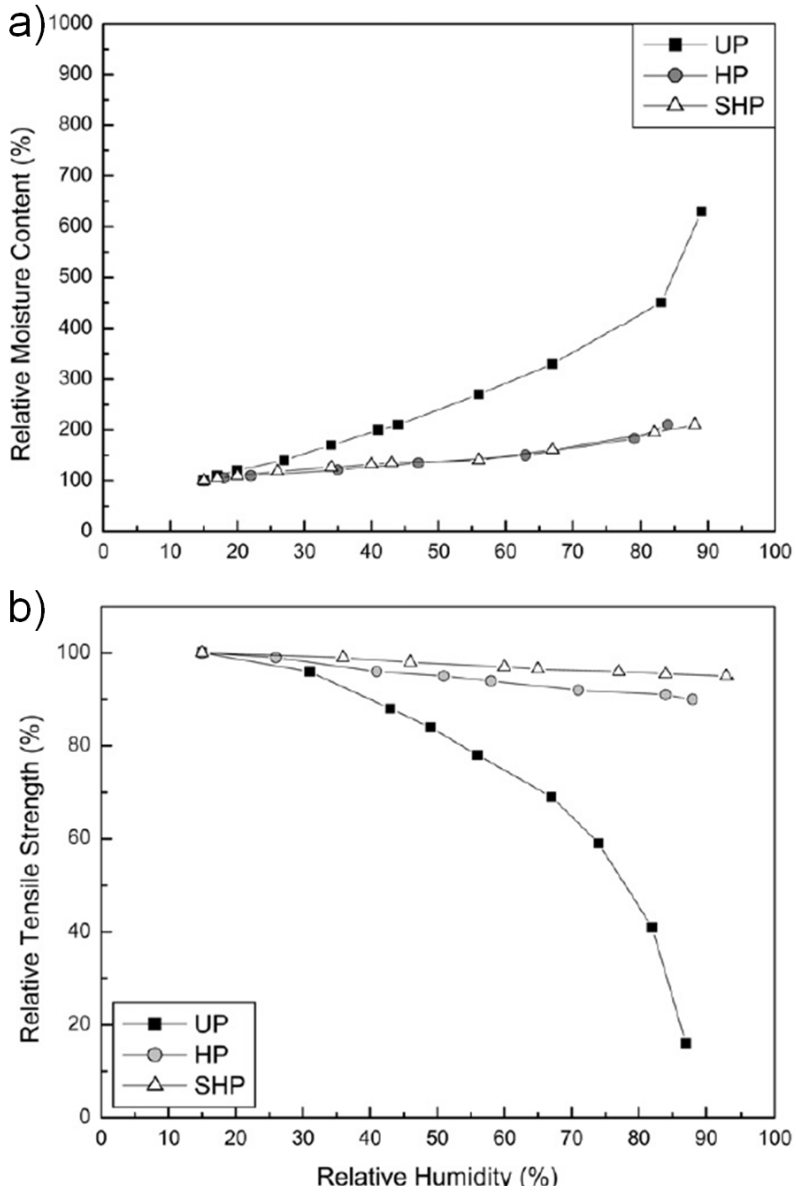

Figure 1.2: Plots of (a) relative moisture content and (b) relative tensile strength vs relative humidity for UP (untreated linerboard), HP (hydrophobic paper treated by POTS only), and SHP (superhydrophobic paper) samples. [9]

The majority of paper that is produced on an industrial scale is not composed solely of cellulose fibers; mineral fillers often make up between 15-35% of the paper. Commonly used fillers include clay, precipitated calcium carbonate, talc, heavy spar,

calcium sulphate and titanium dioxide. [41] These fillers are generally cheaper than wood fibers and their incorporation into paper therefore decreases the manufacturing cost. The addition of fillers can also improve properties such as printability and smoothness, when added in adequate concentrations, by partially filling the vacancies between fibers. In order to yield the correct optical properties in a paper product, filler particles are often also of a suitable size (micron and submicron) to induce superhydrophobic properties. Much of the technology to incorporate and bind fillers to paper has already been developed and implemented at the industrial scale, thus making the extension of filler use towards roughness creation for superhydrophobic paper relatively straightforward. It should be noted, however, that there are drawbacks to the use of high filler content within paper. An increase in filler content often correlates with loss in strength due to interference with the hydrogen bonding between fibers.

Precipitated calcium carbonate (PCC) is a widely used additive, with applications ranging from the construction industry, as an ingredient in cement, to the health industry, as an antacid. Thus, processes have been developed to create well-defined particle geometries, allowing a wide variety of shapes and sizes for specific applications. As a filler in paper, it serves to not only decrease the surface porosity, but also to increase brightness and opacity. Hu *et al.* attained superhydrophobic properties through the binding of PCC to linerboard with a latex slurry and subsequent dipcoating of the sample in a potassium stearate solution to alter the surface chemistry. [42] To quantify the effect of their coating process on water absorption, the Cobb test was employed, which measures the mass of water absorbed per surface area (expressed in g/m^2). As described earlier, fluid absorption generally correlates to a loss in strength; by demonstrating resistance to water absorption, strength retention is implied. In their study, paper samples were exposed to a 10 mm column of water for

10 minutes. Figure 1.3 shows that dipcoating of the paper samples increases the resistance of the paperboard to water absorption, as indicated by the lowered Cobb value. This result is attributed to the uniform coating of stearate salts that are adsorbed onto the individual fibers, protecting them from water and covering the hydrophilic latex used to bind the PCC to the paperboard.

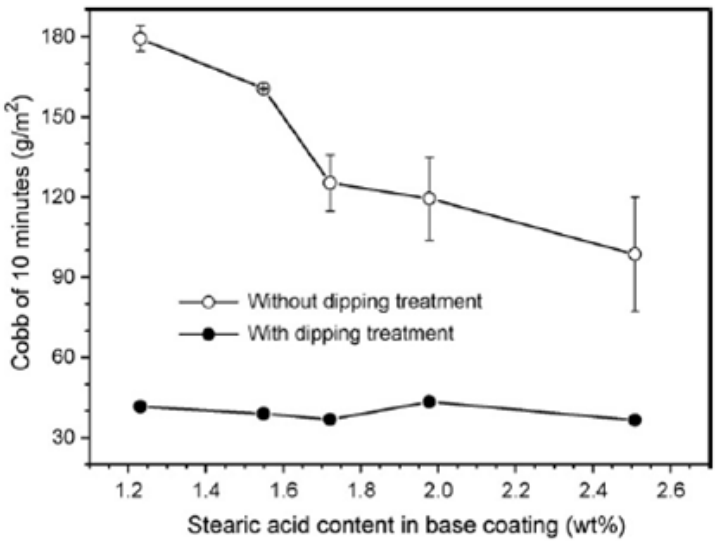

Figure 1.3: Cobb values vs stearic acid concentration of untreated paper board and paper board dipcoated with potassium stearate. [42]

Clay is another globally abundant and commonly used filler. In the paper industry, it has been largely replaced by PCC because of clays lower brightness. [3] Currently, its use is primarily restricted to coated papers for products such as magazines and catalogues. [43] Using an internal mixing airbrush, Barona and Amirfazli sprayed a mixture of organoclay nanocomposite with fluoro-methacrylic latex and a commercial thread locking adhesive onto copy paper. [5] This technique produced roll-off superhydrophobic surfaces that have been shown to be compatible with a variety of other non-paper substrates. Avoiding the use of fluoropolymers, Mesic *et al.* applied hydrophobic clay to the surface of a two-layer linerboard to yield superhydrophobic

properties. [44] Their hydrophobic clay was a commercial kaolin clay that had been modified by calcification and subsequent attachment of amino-functionalized moieties. As shown in Figure 1.4a), the clay particles have a flake-like shape, with an average particle size of 1.5 μm. The clay was mixed in a slurry with starch and a styrene-butadiene latex binder, and then coated onto the linerboard using a bench coater. Comparison of the water resistance of hydrophobic clay coated linerboard (HC) and linerboard coated with conventional clay (CC) is presented in Figure 1.4b) and c). Water absorption was again quantified via the Cobb test, which shows a decrease in water absorption when the linerboard is coated with HC and a further decrease when the HC samples are coated with paraffin wax. For the same set of samples, Figure 1.4c) presents the water vapor transmission rate (WVTR), which measures the amount of vapor that can pass through the coated linerboards per unit area per unit time. The WVTR and Cobb tests quantify two different fundamental processes: the WVTR measures vapor transmission whereas the Cobb test measures water absorption. Figure 1.4c) shows that the HC and HC-wax coated linerboards have a greater WVTR, or vapor breathability, than the CC coated samples. This apparent discrepancy can be explained by the fact that the different particle shapes of CC and HC yield different tortuosities of the porous substrates, thereby affecting vapor transmission rates. A further WVTR increase is observed when the wax coating is applied. This observation was attributed to a change in clay particle shape, since the coating causes a rounding of the flake edges, thus decreasing the tortuosity.

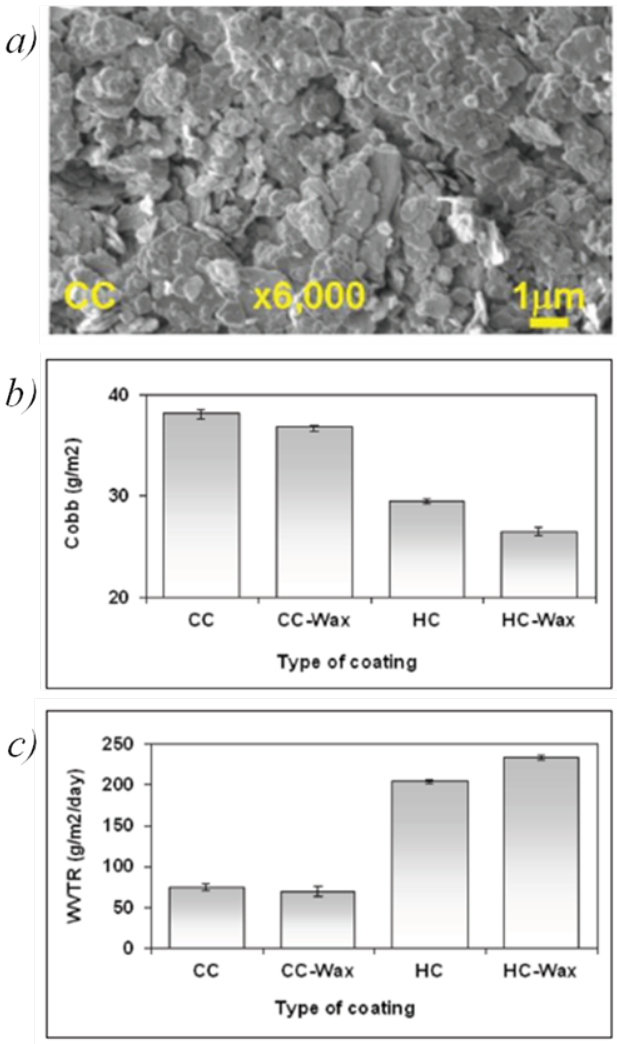

Figure 1.4: a) SEM images of conventional clay (CC) particles b) Cobb values and c) Water vapor transmission rate (WVTR) for linerboards coating with CC and HC with and without wax. [44]

Titanium dioxide is extensively used as a pigment due to its high brightness and refractive index. In the paper industry, titanium dioxide (TiO_2) fillers improve optical properties, such as brightness and opacity. Unlike the other fillers highlighted above, TiO_2 is more expensive than wood fibers, thus limiting its usage to higher grade, value-added products. But, due to its higher brightness when compared to

clay and PCC, TiO_2 can be added in much smaller amounts, increasing the opacity of paper from 50 to 60% with only a 2 wt% percent addition. [45] Tiesala *et al.* demonstrated the use of liquid flame spray (LFS) of TiO_2 particles to create superhydrophobic paperboard surfaces. [46] Titanium tetraisopropoxide (TTIP) was used as the precursor and H_2 and O_2 as the combustion gases in the flame. By expelling the precursor and combustion gases through a nozzle at a high-velocity, the reactions of the precursor vapor result in the formation of nanoparticles, as shown in Figure 1.5. The LFS deposition and particle formation is dependent upon four key parameters: distance between the burner and paper, line speed, concentration of precursor and precursor feed rate. These parameters have been demonstrated to affect both the size of the TiO_2 particles and the uniformity of the deposition. When optimized, a maximum contact angle of $166.6 \pm 1.7^\circ$ was observed. Although a high static contact angle was achieved, all samples exhibited a strong droplet adhesion (high contact angle hysteresis). Wear testing revealed compromised durability, showing a loss of superhydrophobic properties after applying and removing tape from the surface, and after wiping the surface with a microfiber tissue. Unfortunately, this study did not characterize the chemical properties of the modified surface in detail. As discussed above, superhydrophobic surfaces require both appropriately sized surface structures and low surface energy. Untreated TiO_2 is a hydrophilic solid [47]; as a consequence, in order to account for the measured superhydrophobic properties a surface coating must exist on the LFS-generated nanoparticles. The authors demonstrate later that the coating on these particles is a spontaneously formed carbonaceous layer. [48]

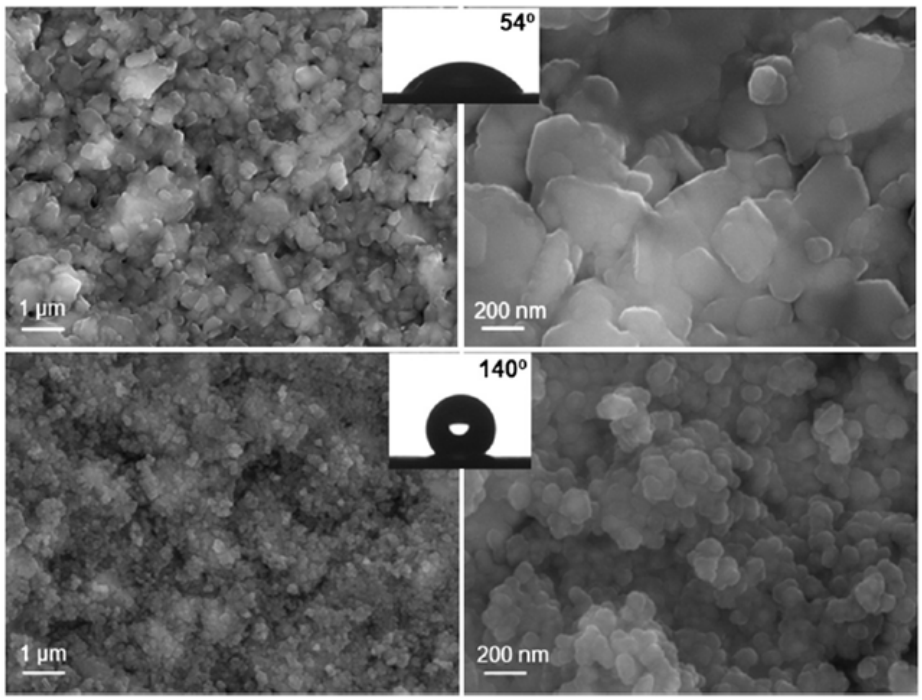

Figure 1.5: FE-SEM images of the pigment coated paperboard surface before (top row) and after (bottom row) the nanocoating. [46]

Huang *et al.* also prepared superhydrophobic paper via the addition of TiO_2 nanoparticles. Their particles, 10-20 nm in size, were modified through a silane grafting reaction of 3-(trimethoxysilyl) propyl methacrylate (MPS), yielding a lowered surface energy. [49] While the previously mentioned techniques apply surface roughness to premade paper products, particles in this study were added to the pulp before the paper was formed and then mechanically dispersed to prevent agglomeration. After agitation, the pulp was formed into handsheets. By varying the nanoparticle concentration, and thus the fiber coverage, the contact angle was modified. Figure 1.6 shows an increase in contact angle as the nanoparticle concentration is increased, reaching a maximum static contact angle of 154.2° for 13 wt% MPS-modified TiO_2. In addition, it was noted that these surfaces exhibit low contact angle hysteresis.

Due to the beneficial optical properties of the TiO_2 particles, the increase in concentration also correlated to enhanced opacity of the handsheet. For the same loading concentrations, the MPS modified TiO_2 causes a greater increase in opacity than the unmodified TiO_2, which was attributed to a more uniform particle distribution with the MPS modified TiO_2. However, consistent with other fillers, it was shown that the increased TiO_2 loading correlates with a decrease in tensile strength. Again, particles added to pulp get trapped between fibers, which inhibits fiber-fiber hydrogen bonding. While a more easily scalable process when compared to some surface techniques, the addition of filler to the bulk pulp inherently requires more material since it is dispersed throughout the paper, instead of being confined to the topmost surface. Furthermore, the high percentage of filler required to attain superhydrophobic properties makes the process difficult to justify due to high cost of TiO_2.

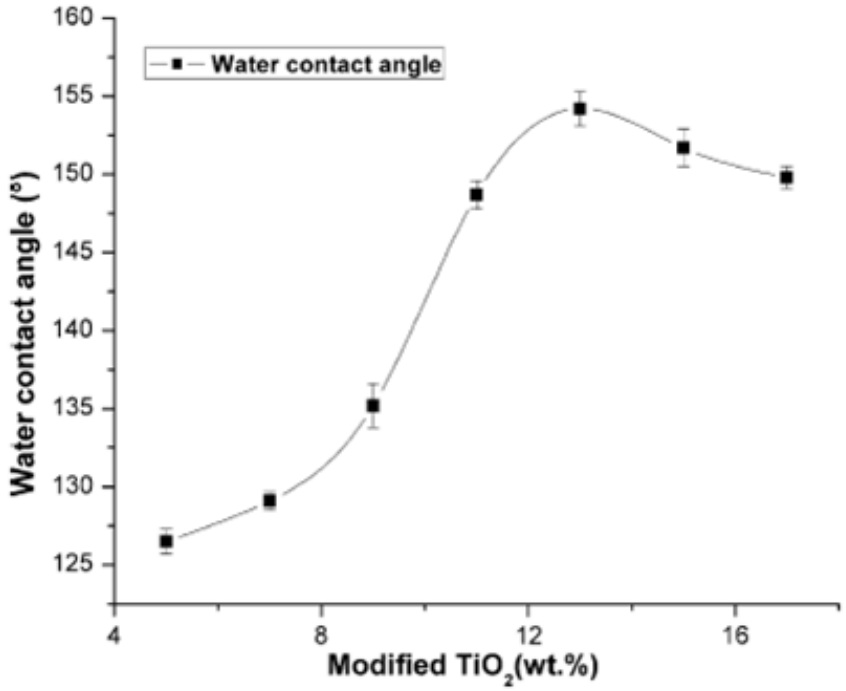

Figure 1.6: Water contact angle of sheets modified with TiO_2[49]

1.2.1.2 Surface Silanation

While the majority of bottom-up techniques involve the deposition of particles to create surface roughness, researchers have also developed techniques to deposit non-fluorinated surface coatings that create roughness in-situ. Li *et al.* have done extensive research on the use of trichloromethylsilane (TCMS) to create surface roughness on paper and other cellulose-based substrates. [50–52] Their studies take advantage of the formation of silicon nanofilaments during chemical vapor deposition, which was first observed and used to create superhydrophobic surfaces by Seeger *et al.* [53] In their primary study, Li *et al.* used chemical vapor deposition (CVD) of TCMS to coat cotton fabric samples. [50] The CVD process entirely coats the cellulose fibers and, when heated, produces a layer of polymethylsiloxane on the fiber surface. Exposure to the CVD process for five minutes increases the contact angle to >155°, while hysteresis values were unreported. Examination of these coatings under FE-SEM in Figure 1.7a) shows that the fibers are individually covered by the TCMS-generated coating. Calcination of the samples at 500°C for 6 hrs further demonstrates that the coatings create replicas of individual fibers, as shown in Figure 1.7b). The hollow shells of polymethylsiloxane also possess nano-scale roughness on top of the microscale roughness of the fibers. Simply put, the coating process uses the fiber structure as a template to create tubular structures. These structures are inherently more stable than particles that are bound to the surface. The surface coating was tested for durability and superhydrophobic properties were retained even after 20 laundry cycles. While this is a promising approach, the authors note that the CVD process damages the cellulose fibers and affects their mechanical properties. For example, the hydrogen chloride byproduct from reaction of TCMS with hydroxyl groups [54], results in chemical attack and destruction of the cellulose fibers.

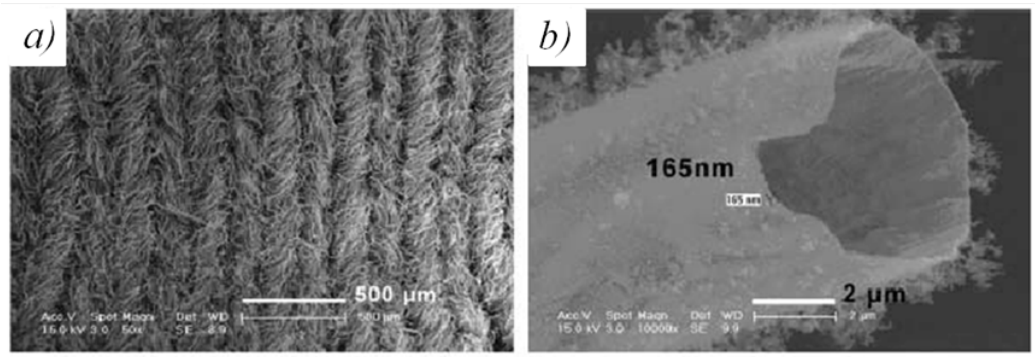

Figure 1.7: Images of a) modified cotton textile b) single hollow silica wire. [50]

In a follow-up study, the same authors applied a commercial waterproofing reagent, potassium methyl siliconate (PMS), in order to avoid the detrimental effects of TCMS grafting. [51] The process effectiveness of coating both paper and cotton substrates was demonstrated by placing samples into the PMS solution and then lowering the pH; uniform siloxane coatings were created on the fibers, similar to those formed from TCMS. The PMS coated surfaces also exhibited superhydrophobic properties and resistance to 20 wash cycles. In addition, the coating deposited was transparent, as demonstrated on cotton fabric and paper shown in Figure 1.8a) and b). This property makes application of this process to textiles and prefabricated paper products attractive.

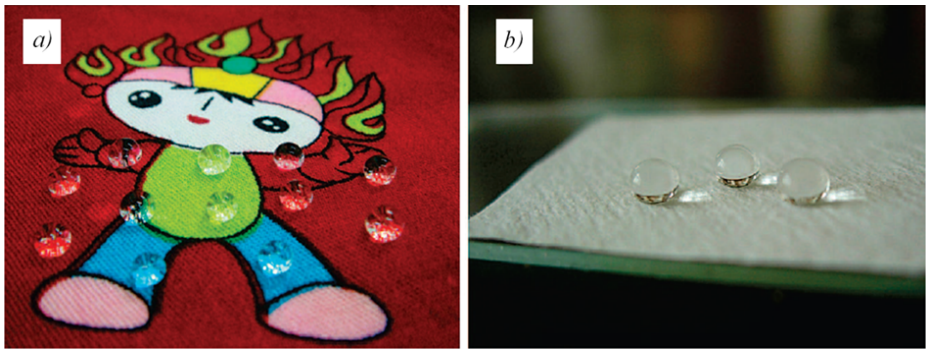

Figure 1.8: Optically transparent superhydrophobic siloxane coatings on a) cotton fabric and b) paper. [51]

1.2.1.3 Waxes

As discussed previously, the use of waxes as hydrophobic coatings on paper has already been investigated and implemented by the paper industry. The low surface energy properties and environmental friendliness of waxes make them attractive candidates for surface coatings. In order to waterproof a paper product, thick layers of wax are often needed to ensure complete pore coverage. The majority of paper products that are currently produced contain some recycled fiber, with some grades of paper fabricated entirely of recycled fiber. If waxes, also referred to as stickies, are not fully removed during the recycling process, they can agglomerate, resulting in defects in the final product. Removal of stickies requires the use of either centrifugal cleaners or chemical dispersants, both of which add to the overall manufacturing cost. The amount of wax required to prevent fluid absorption can be reduced by attaining a Cassie-Baxter wetting state, in which air pockets are used to support the droplet, differing from current methods that prevent water penetration into the paper by blocking them with thick layers of wax. Combining the use of low surface energy waxes and roughness, Turner *et al.* produced superhydrophobic wax surfaces on paper from alkylketene dimer (AKD). [55,56] On a flat surface, AKD has a Youngs

contact angle of 109°, rivaling many fluoropolymers. Within the paper industry, AKD is commonly used as a sizing agent, providing marginal hydrophobicity at common loadings. Previous research has demonstrated that AKD can spontaneously form a fractal structure upon solidification. When combined with the intrinsic low surface energy of AKD a superhydrophobic surface is produced without further modifications. [57, 58] Applying the same methodology, Turner *et al.* used rapidly expanding supercritical carbon dioxide (RESS) to apply AKD to filter paper, also forming a fractal structure as seen in Figure 1.9a)-d). [55] By dissolving small particles of AKD in supercritical-carbon dioxide (CO_2) and spraying the solution onto substrates, small fractal particles with a narrow size distribution can be formed without the need for additional chemicals or solvents. The size and uniformity of the particles is dependent on the pre-expansion pressure, pre-expansion temperature and spraying distance. An increase in the pre-expansion pressure and temperature decreases the particle size, while increasing the spraying distance increases the average size. The particle sizes ranged from <1 μm to 5 μm, with the majority between 1 and 2 μm. Using the RESS process, Turner *et al.* sprayed AKD onto filter paper at conditions of 40°C, 300 bar and a spraying distance of 10mm, with a resulting water contact angle of 153.0°. Pre-roughening the filter paper by rubbing with emery cloth and then performing the RESS process increased the contact angle to 172.0°. This is likely due to the addition of micro-scale roughness through abrasion. The authors also mention that the same process can be performed with other fatty acids such as stearic acid and stearine. While the process produces superhydrophobic surfaces on paper, their stability is of concern. Waxes are typically malleable, making the intricate surface structures susceptible to deformation and loss of superhydrophobic properties when pressure is applied.

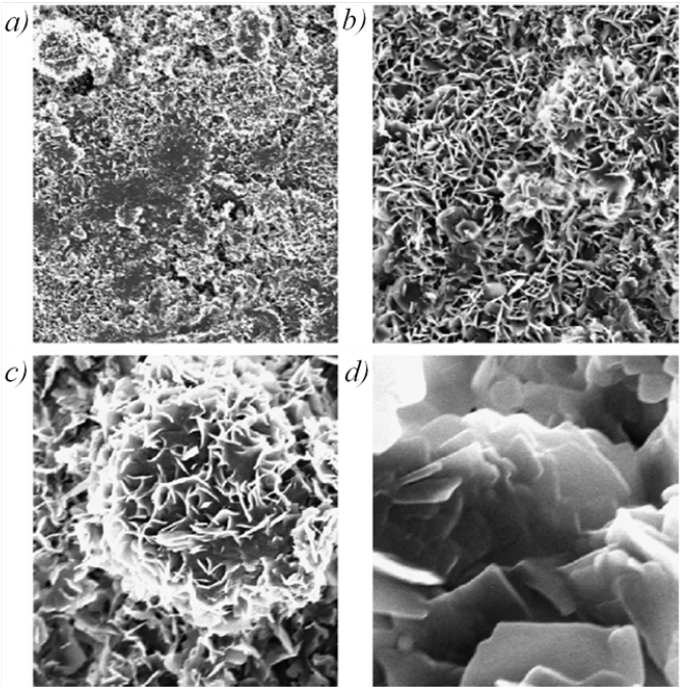

Figure 1.9: SEM micrographs of AKD structures formed by a RESS process at (a) 2000x; (b) 5000x; (c) 10,000x; and (d) 50,000x. [55]

1.2.2 Top-Down Techniques

The selective etching of surfaces is the most commonly exploited top-down technique and is most frequently applied to inorganic surfaces, where etching takes advantage of natural grain boundaries or lithographically fabricated masks. [25] Selective etches remove chemically less stable or more reactive material, and generally enhance roughness. Unlike surface addition, where the strength of the bond between particles and surface is of concern, selective etching has the advantage of maintaining the inherent mechanical stability of the substrate. Many polymers contain both crystalline and amorphous phases, and exposure to an oxygen plasma has been shown to selectively etch the less strongly bonded amorphous phase. [59] Balu *et al.* applied this mechanism to standard copy paper and to handsheets made according to TAPPI standard T205 sp-02. [18,37,60,61] Cellulose, a biopolymer, contains both crystalline

and amorphous domains. When exposed to an oxygen plasma, the amorphous cellulose is etched away at a faster rate, leaving the crystalline domains. This process creates nanoscale roughness, as shown in Figure 1.10. If unetched paper surfaces are coated with a 100 nm crosslinked fluoropolymer film, a nearly superhydrophobic, high hysteresis (sticky) state is attained, with a static contact angle of 144.8° and a high hysteresis of 79.1°. Etching in the oxygen plasma for 30 min followed by deposition of 100 nm of fluoropolymer from a pentafluoroethane (PFE) precursor, yields a roll-off (low hysteresis) superhydrophobic surface on both commercial copy paper and handsheets.

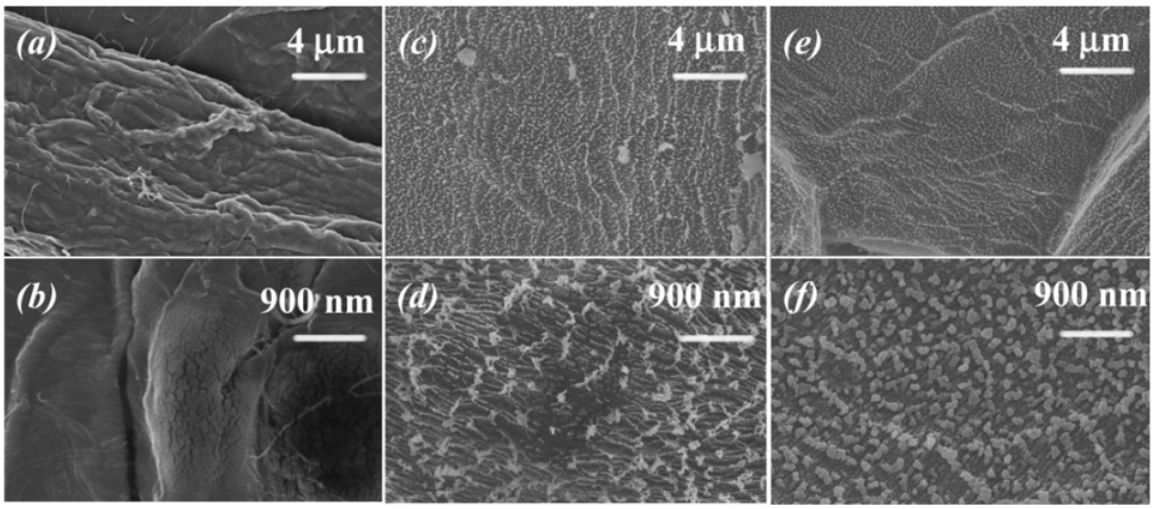

Figure 1.10: High-magnification SEM images (5000x and 20,000x) of (a,b) untreated handsheet fiber, (c,d) oxygen-etched handsheet fiber, and (e,f) oxygen-etched and PFE-coated handsheet fiber (superhydrophobic treatment). [18]

Balu *et al.* further studied the effects of oxygen plasma on cellulose fibers by varying the etch time. Through this study it was demonstrated that the sample hysteresis can be tuned by the etch process. Figure 1.11 shows that as etch time is increased, the receding contact angle increases, while the advancing contact angle remains nearly constant; the result is a decreasing hysteresis. The observed phenomenon is believed

to be due to a change from a Wenzel wetting state to a Cassie-Baxter state at the nano-scale, as depicted in Figure 1.12. The high hysteresis values observed at the lower etch times are caused by pinning of the water droplet at the three phase contact line. The increased etch time correlates to an increase in nano-scale roughness, allowing the wetting state to change and reducing the contact area of the paper with water. While systematic measurements have yet to be performed, preliminary mechanical stability tests suggest that the etching process does not degrade the superhydrophobic properties substantially. These observations indicate that since the roughness is uncovered from the fiber itself, the durability of these plasma etched surfaces should depend more on the fiber-fiber bonding strength than on the mechanical integrity of the roughness, that is generated by the etch process.

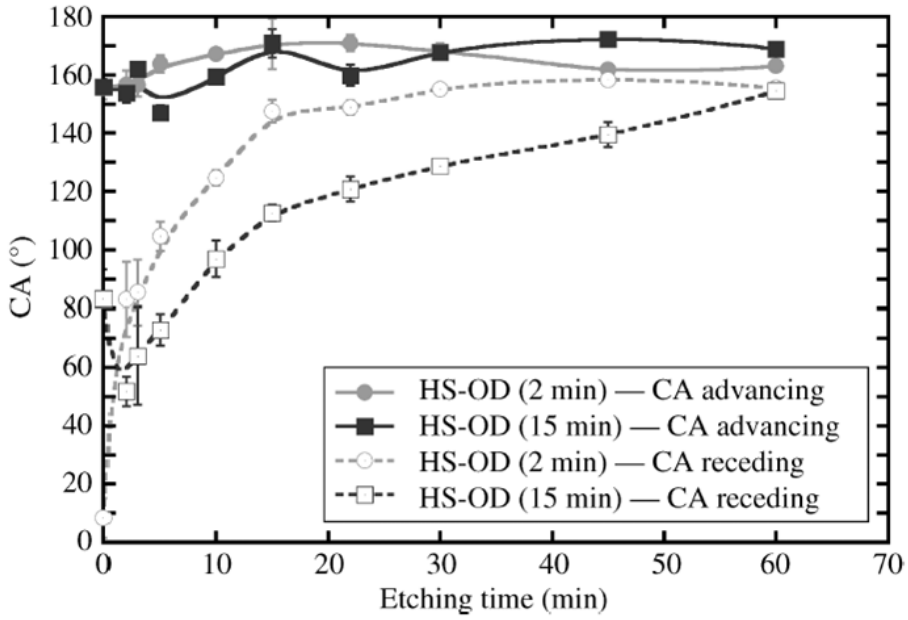

Figure 1.11: Plot of advancing contact angle and receding contact angle of handsheets that were dried overnight (HS-OD) with respect to oxygen plasma etching time for 2 min and 15 min PFE depositions. [37]

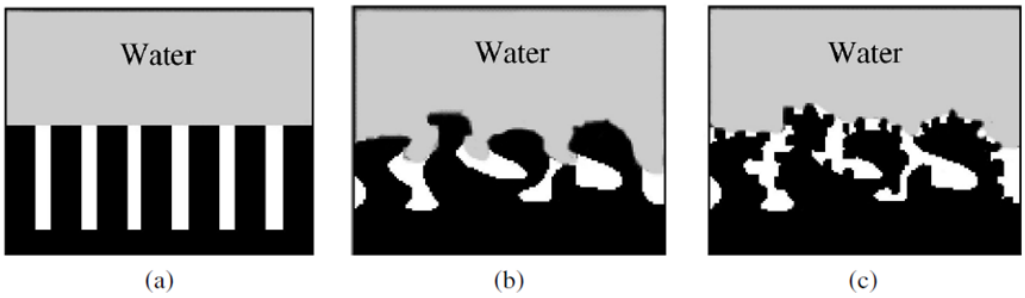

Figure 1.12: Schematics of interactions of water with surfaces in a) an ideal Cassie state , b) a sticky superhydrophobic state and c) a roll-off superhydrophobic state. [37]

1.3 Alternative Uses for Superhydrophobic Paper

The previous section have indicated that the fabrication of superhydrophobic surfaces on paper stands to be industrially beneficial, preventing water absorption and loss of strength in the underlying bulk paper. However, the capabilities of superhydrophobic paper extend far beyond its use as a packaging medium. The vast worldwide infrastructure of paper manufacture has resulted in many commercial applications as a single-use, disposable commodity product. The availability of paper, combined with the previously mentioned physical properties, in particular mechanical flexibility, renewability and low cost makes paper a unique substrate that differs from inorganic substrates. As demonstrated in Section 1.1, the fabrication of superhydrophobic paper does not require expensive, cleanroom techniques. Moreover, several authors have applied superhydrophobic surfaces to commercially available paper grades, demonstrating real world applicability of their techniques. The combination of these factors have led to the proposal of disposable cellulose-based superhydrophobic surfaces. These surfaces would not only be applicable to any current application of paper that requires low water adhesion, but they also stand to replace non-cellulose based materials in a plethora of fields. In the following section we describe several novel applications that

can only be realized through the generation of superhydrophobic properties on paper.

1.3.1 Antibacterial

Control of bacterial and cellular adhesion onto surfaces has been of great interest to the bio-engineering field. Studies have demonstrated that certain levels of surface roughness can increase and improve the quality of bone growth on implants. [62, 63] Antithetically, the same roughness has been studied for the prevention of cellular growth and bacterial adhesion. [64,65] Anti-fouling and self-cleaning properties of superhydrophobic surfaces are of great interest for biomedical applications. A droplet in the Cassie-Baxter wetting state, by definition, has a greatly reduced contact area compared to a droplet in the fully wetted Wenzel state. As the contact angle increases, the contact area of the droplet decreases; droplets in a superhydrophobic Cassie-Baxter state thus have a decreased likelihood for bacterial deposition. Also, the self-cleaning properties of low hysteresis superhydrophobic surfaces facilitate the removal of bacterial surface contamination. Finally, surface roughness itself has been hypothesized to prevent mechanical adhesion of bacteria to the surface, thus inhibiting growth. [64]

Antibacterial surfaces from paper and other fibrous cellulose based products such as cotton, offer great potential in a number of applications, such as paper based bacterially resistant packaging for meats. Yang and Deng studied the adhesion of bacteria to their layer-by-layer deposited superhydrophobic surface on linerboard. [9] After spraying the surfaces of the sheets with E. Coli (Escherichia coli), samples were either inclined by 5° after 5 seconds, or dipped into a water bath after 1 second. Figure 1.13 shows the adhesion of bacteria to untreated paper (UP), paper treated with only POTS fluoropoylmer (HP) and paper treated with both the silica and POTS fluoropolymer (SHP) (see also Figure 1.2). Due to the roll-off properties of the SHP, bacteria contaminated water droplets rolled off readily, removing most of the bacteria.

In comparison, the UP absorbed the fluid along with the bacteria into the paper bulk, making removal of the bacteria impossible. Similarly, low hysteresis superhydrophobic surfaces on cotton have also exhibited low bacterial adhesion properties. [66]

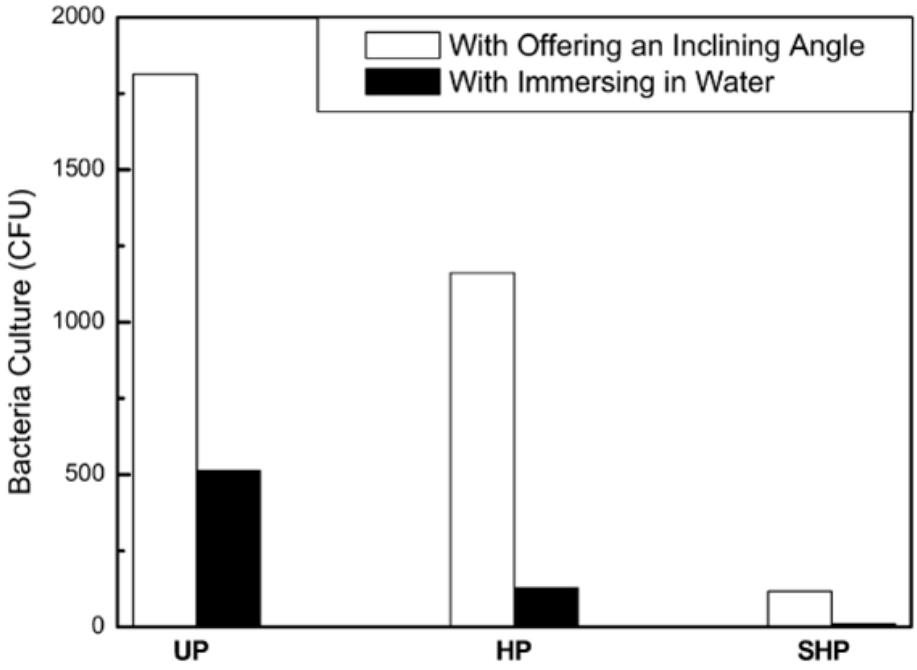

Figure 1.13: Bacteria culture density, measured in colony forming units (CFU), on UP (untreated paper), HP (hydrophobic paper treated by POTS only), and SHP (superhydrophobic paper) specimens after offering an inclining angle of 5° for 5 s and with fully immersing in water for 1 s. [9]

While roll-off superhydrophobic surfaces resist bacterial adhesion, they do not actively kill bacteria. Silver nano-particles have demonstrated strong toxicity towards cells, and for this reason have been applied to surfaces as a bactericide. [67–69] Incorporation of these particles into cellulose-based substrates has been combined with a low surface energy surface coating in order to simultaneously maximize the resistance of the surfaces to bacterial adhesion and growth. [70, 71] However, as discussed in Section 1.1, these bottom-up fabricated surfaces are subject to concerns about

mechanical stability (e.g., robustness during washing cycles for textiles). Tomsic *et al.* showed that cotton samples coated with silver nano-particles and a fluoroalkyl-functional water-born siloxane demonstrated >95% reduction of both E. Coli and S. aureus (Staphylococcus aureus) bacteria. [70] However, after 10 wash cycles, the reduction decreased to 41%. Kahlil-Abad and Yazdanshenas showed similar properties on woven cotton textiles. [72] Through the in-situ formation of silver nano-particles directly on the fiber surface followed by coating with octyltriethoxysilane, anti-bacterial properties along with a static contact angle of 151° were attained. Figure 1.14 shows the zones of bacterial inhibition around cotton fabric samples in agar plates inoculated with E. Coli and S. aureus. In order to demonstrate the durability of these samples, sheets were immersed in ethanol and washed in a sonication bath for 30 min. The washed cotton samples exhibited the same contact angles and antibacterial properties as the unwashed samples.

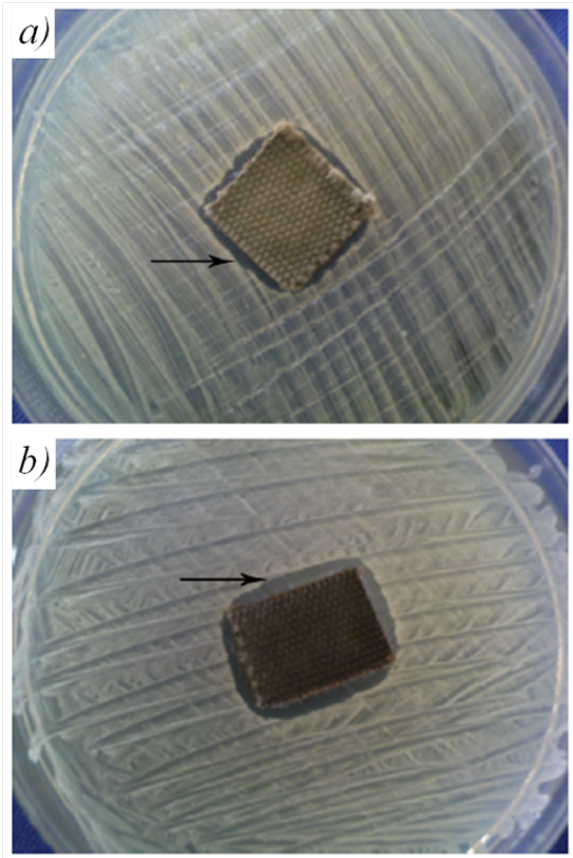

Figure 1.14: Antibacterial activity of modified cotton textiles. Zone of inhibition is indicated by arrows. a) Modified cotton fabric placed on the agar plate inoculated with Escherichia coli showing a comparatively small zone of inhibition (1.5 mm) and b) modified cotton fabric placed on the agar plate inoculated with Staphylococcus aureus showing a comparatively large zone of inhibition (3 mm). [69]

1.3.2 Paper Based Microfluidics

The hydrophilic nature of untreated paper has proven to be beneficial in several industries and applications. The strong capillary forces that exist between fibers allows water to be absorbed and held in the fiber web. Beyond its wide use as an absorptive wipe, the ability to functionalize paper by binding chemicals to the paper web has been exploited to yield colorimetric tests, such as pH and glucose level dipstick tests.

Through the functionalization of paper, fluid transport can be controlled within the bulk much like microfluidic devices do. However, instead of using pumps, the capillary forces within paper can transport fluids without the application of external forces or energy. Whitesides *et al.* have applied this idea and developed microfluidic devices on paper substrates that are capable of testing for multiple diseases simultaneously. [73, 74] Their procedure utilizes a wax binding technique to make most of a paper substrate hydrophobic, except for hydrophilic channels and reservoirs with the desired connectivity. Fluid wicked into the paper then follows the channels, eventually reaching colorimetric reagents that have been incorporated into the reservoirs, where colorimetric reactions can be used to measure relative concentrations of chemicals or to identify diseases. [73] For example, colorimetric tests have been designed and demonstrated that quantify levels of glucose and bovine serum albumin (BSA) through variations in color intensities.

Superhydrophobic paper can be functionalized to perform similar techniques on top of the paper surface, rather than inside the bulk paper. The devices described above wick the fluid into the paper, which has distinct disadvantages. For example, splitting a single droplet of test fluid into multiple samples of well-defined volume is impossible in the channel-based devices. Also, extraction of the fluid for further testing after the initial screening is difficult to achieve. In contrast, superhydrophobic paper confines fluids to the paper surface, and through manipulations, permits splitting and sampling of a single droplet. Balu *et al.*, using roll-off superhydrophobic paper substrates, fabricated lab-on-paper (LOP) devices by creating wax patterns on a commercial Xerox printer. [37] The printer utilizes a solid wax cartridge as its ink source, which yields hydrophobic wax patterns on the surface of the paper. While all techniques discussed in previous sections focused on homogeneous surface modification, the wax printing purposely generates carefully designed heterogeneous patterns to enable manipulate of droplets. The difference in hydrophobicity between the wax

and the superhydrophobic paper surface (both with regards to contact angle and contact angle hysteresis) yields preferential adhesion of the droplet to the wax, as seen in Figure 1.15. Water droplets on the proprietary Xerox wax, which has both higher hysteresis and lower contact angle than the superhydrophobic paper, experienced a higher adhesive force, thereby pinning them to the printed designs. The commercial printer, in combination with standard drawing software enables simple, reproducible and flexible generation of printed patterns of highly customizable designs. These functionalized sheets have been used to perform many common fluid manipulation operations that are also employed in microfluidics. Because of the adhesion dependence on hysteresis, this concept was referred to as Hysteresis Enabled Lab-on-Paper (HELP) devices.

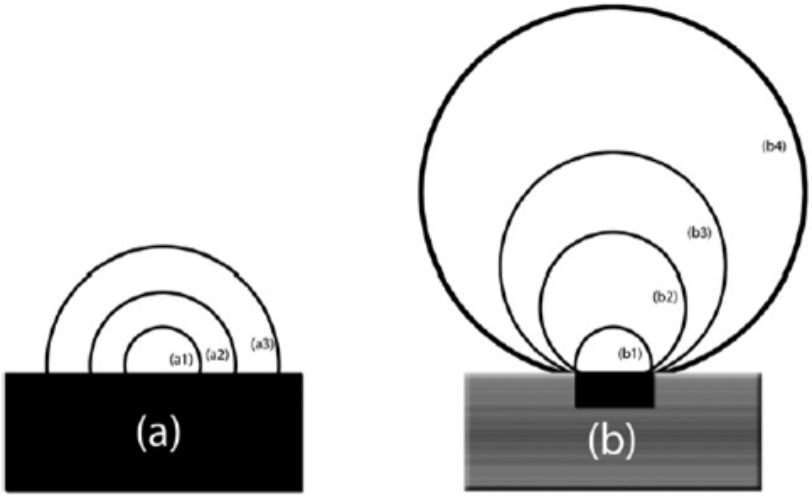

Figure 1.15: Schematics of side view profiles for various drop volumes a) on a homogenous hydrophobic surface (contact angle >90°) and b) on a superhydrophobic surface (contact angle >150°) with hydrophobic (contact angle >90°) pattern. [60]

Figure 1.16 highlights some of the unit operations made possible by printing wax patterns on superhydrophobic paper. Figure 1.16 shows a) droplets that preferentially adhere to arrays of printed wax dots, allowing the storage of the droplets, b) controlled droplet transfer between two sheets that both have printed wax dots, c) droplet mixing and coalescence using dots and lines to contain the droplets, and d) droplet sampling to generate small sample volumes from a bulk droplet. The operational functionality of these microfluidic capabilities strongly depends on the geometry of the printed patterns. For example, in Figure 1.16a), the maximum droplet volume that can be supported at a 90° angle is a function of the area of the printed dot. Also, for Figure 1.16b), the size of the printed dot on the top sheet must be larger in area to apply sufficient adhesive force to overcome gravity and pick up the droplet; its size determines the maximum volume that can be transferred.

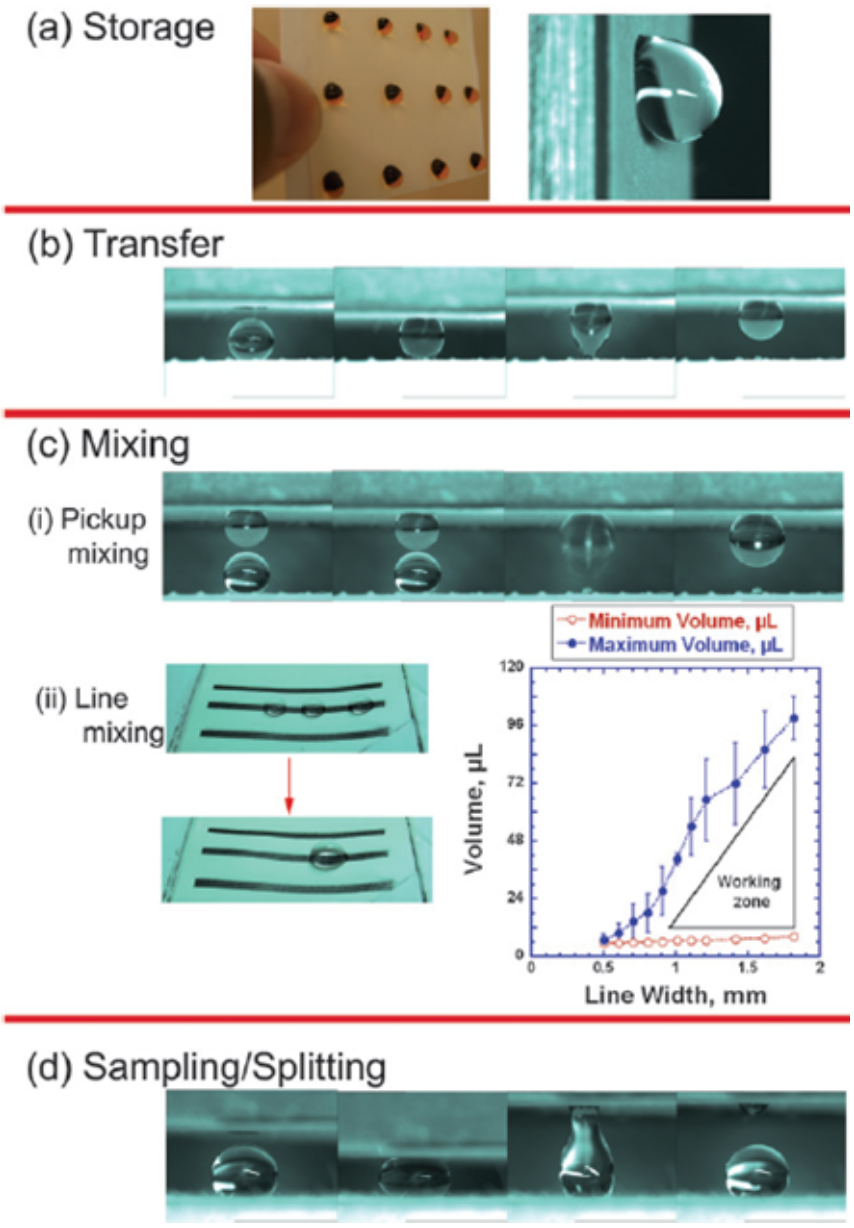

Figure 1.16: a) Photographs of an array of drops (food coloring was added to enhance contrast) and a high magnification image of a single drop stored on a vertical substrate, b) series of snapshots of a drop being transferred between two substrates, c) photographs of merging and mixing: (i) via pickup mixing (two drops), (ii) line mixing (three drops) and plot that shows the working zone of drop volumes suitable for line mixing, d) photographs of drop splitting between two substrates. [60]

These printed designs can also provide anisotropic adhesion of droplets to a surface. [61] Much like the wings of a butterfly exhibit low hysteresis properties in one direction and high hysteresis properties in the other, specific printed designs were found to have direction dependent properties. [75] An example is the semi-circular design shown in Figure 1.17, which again was printed in wax onto low hysteresis superhydrophobic paper. When a droplet of sufficient size was placed on the design, the force of adhesion differed significantly in the convex and concave directions. An increased force was observed in the concave direction due to the greater contact of the receding contact line with the edges of the patterns during separation. When the paper is tilted in the convex direction, the receding contact line detaches from the line more gradually. Other designs and droplet volumes were also investigated, with similar results and conclusions regarding directional adhesion.

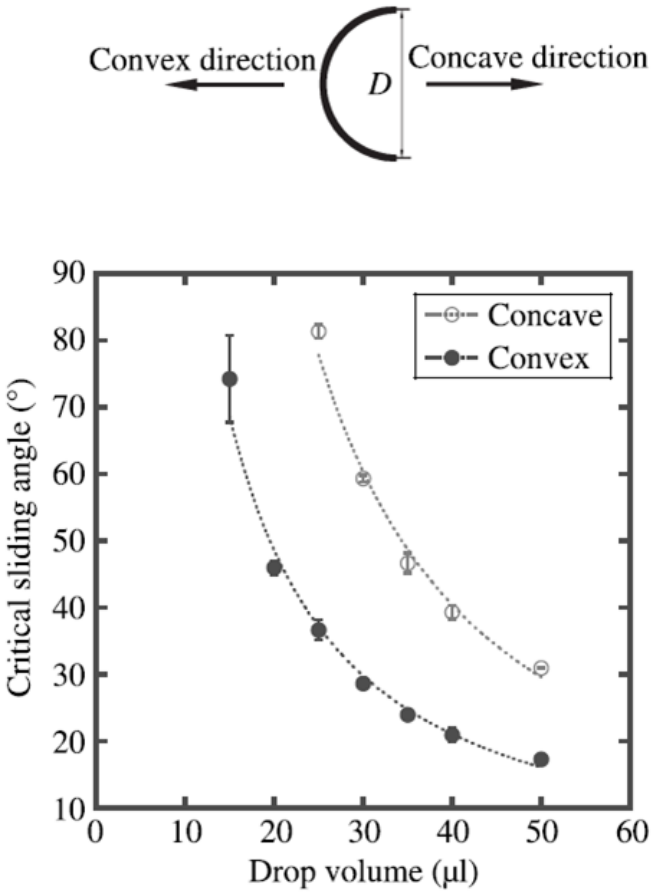

Figure 1.17: Critical sliding angles in different sliding directions vs drop volume for a semi-circular ink pattern printed on superhydrophobic paper substrate (diameter D = 2.55 mm); the slide directions are defined at the top of the figure. [61]

In addition to using specific shapes to control adhesion of droplets to a superhydrophobic surface at a specific point, large surface areas have also been modified. Wax dot arrays were printed onto superhydrophobic paper substrates as shown in Figure 1.18, with each individual dot being significantly smaller than the droplet. Array dimensions are given in Table 1. Previously, Chen *et al.* demonstrated that the specific shape and size of surface structures affects the three phase contact line of liquids on solid substrates. [58] Alteration of this contact line resulted in a modified hysteresis. The printing of wax dot arrays on paper accomplishes the same effect.

While meaningful hysteresis values could not be collected due to the inhomogeneity of the surface, droplet sliding angles were found to increase from pattern d) to a). The sliding angle values for the patterned surfaces were intermediate between that of a superhydrophobic sheet and a uniform wax film (minimum and maximum values, respectively).

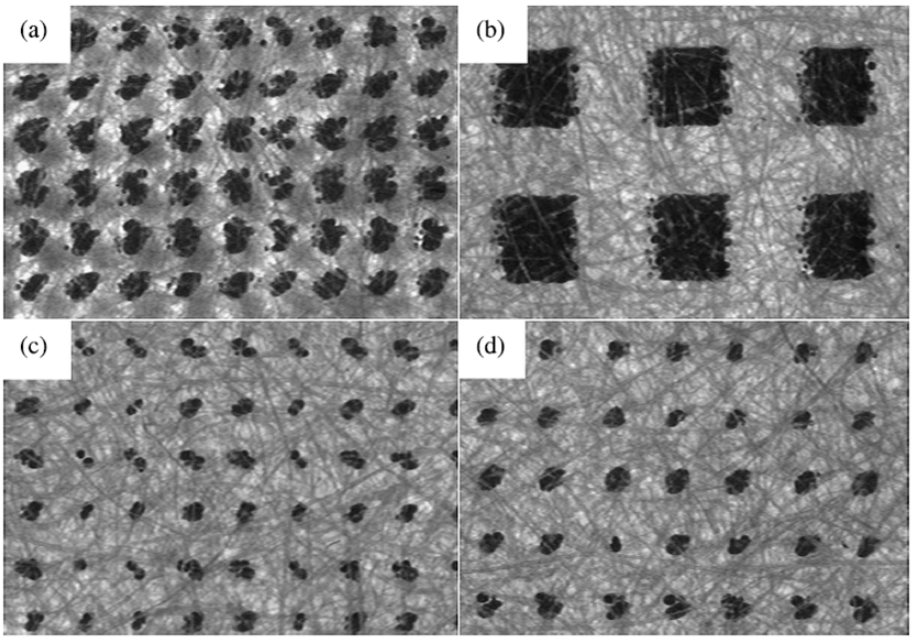

Figure 1.18: Bright field microscope images of checker patterns printed on superhydrophobic paper surfaces. Sizes of features are given in 1.1. [61]

Table 1.1: Area fraction and dimensions of the ink features in checker patterns printed on superhydrophobic paper surfaces. [61]

Pattern	Area fraction (%)	Feature size (μm)	Distance between features (μm)
a	25.4 ± 0.9	176.3 ± 3.4	346.8 ± 4.6
b	25.7 ± 1.2	532.9 ± 8.1	1041.5 ± 6.0
c	8.1 ± 0.2	107.2 ± 1.7	371.2 ± 1.2
d	7.9 ± 0.4	123.4 ± 2.7	431.7 ± 0.4

Barona and Amirfazli conducted a similar study using nano-clay sprayed superhydrophobic surfaces and a commercial ink-jet printer, varying the coverage of the print from 0% (unprinted) to 100% (maximum coverage). [5] Their results, summarized in Figure 1.19, showed 3 regimes of wetting: 1) low hysteresis and high water contact angle between 0% and 30% coverage, 2) increasing hysteresis and nearly constant, high water contact angle from 30% to 85%, and 3) high hysteresis and decreasing contact angle from 85% to 100% coverage. The studies by Bala *et al.* and Barona and Amirfazili both demonstrated the tunability of hysteresis, and therefore adhesion, of water droplets on superhydrophobic paper substrates through the use of commercial printing methods for pattern generation. The functionality added by surface patterning to enable the selective adhesion and directional control of fluids show a great deal of promise for application as a multifunctional substrate for droplet manipulation.

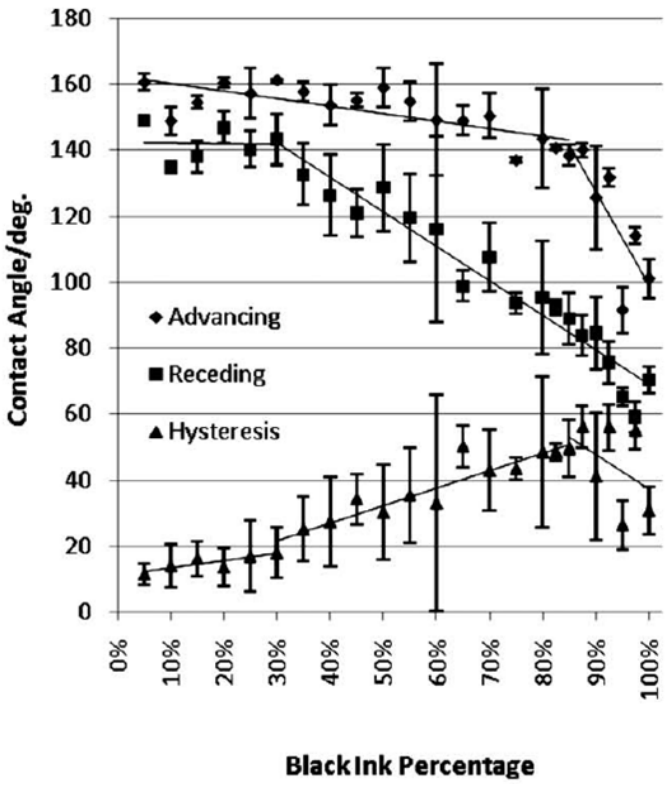

Figure 1.19: Wetting data for printed samples of superhydrophobic paper printed with checkered pattern. Three different wetting regimes are observed: 0 to 30%, 30 to 85% and 85 to 100% (lines are to guide the eyes). There is little change in the advancing contact angle up to 85% while the receding contact angles start to steadily decrease after 30%. [5]

1.3.3 Water and Oil Separation

The separation of oil and water fluid mixtures is an industrially relevant process that is often plagued by low efficiency operations. Specially designed superhydrophobic surfaces offer a unique solution to this problem. Due to the significant differences in fluid surface tension between water and oils, superhydrophobic surfaces often exhibit low contact angles for oils, classifying them as oleophilic. This fact has been exploited to fabricate surfaces that are superhydrophobic while also being superoleophilic. [76–

79] The majority of these studies utilize commercially available metallic wire mesh as a base substrate. Deposition of smaller scale roughness to the wires, along with a fluoropolymer, results in a highly porous (100-1000 μm pore width) superhydrophobic surface. [13] The superhydrophobic properties cause water to bead up and roll off the mesh surface, while oils are readily wet. The porous structure of the mesh in combination with the oleophilic properties allows oil to pass through the mesh, while supporting water on the surface, effectively separating the two fluids with no energy input.

The absorptive properties of paper can be exploited in a similar manner. By creating superhydrophobic papers that are oleophilic, water can be repelled while oil is selectively absorbed. Wang *et al.* have demonstrated a superhydrophobic surface on paper that exhibits absorption selectivity of fluids based on surface tension. [80] Using filter paper as a substrate, superhydrophobic properties were attained by binding silica nanoparticles to the fiber surfaces with polystyrene. The resulting substrate exhibited a water contact angle of $\sim 158^\circ$ and a roll-off angle of $>5^\circ$, allowing the paper to be submerged in water without water absorption. The polar/nonpolar fluid separation capabilities of superhydrophobic treated paper were demonstrated by placing the treated sheet into a mixture of water and diesel oil, as seen in Figure 1.20. The filter paper selectively absorbed the diesel oil (dyed red), leaving behind the water when the sheet was removed from the reservoir. Similar results were observed with other nonpolar solvents, such as hexane, octane and dodecane. By drying the sheets in an oven at 80°C, the sheets could be regenerated, absorbing nearly the same amount of nonpolar fluids after 5 absorption/dry cycles. It was also demonstrated that the filter paper is capable of separating water and diesel oil in an emulsified mixture, performing better than two commercial membranes. [80] When fluid mixtures of water and oil were poured onto the sheet at an angle, the nonpolar components pass through the sheet, while water is repelled and flows off the surface. By weighing

the oil that passes through the sheet, a separation efficiency of >95% was observed for several water/diesel oil ratios. Furthermore, even the separation of miscible fluids was demonstrated with ethanol-water mixtures. While incapable of achieving high separation efficiencies, the superhydrophobic treated filter paper allows droplets with high ethanol concentrations to pass through, decreasing the ethanol in the repelled fluid.

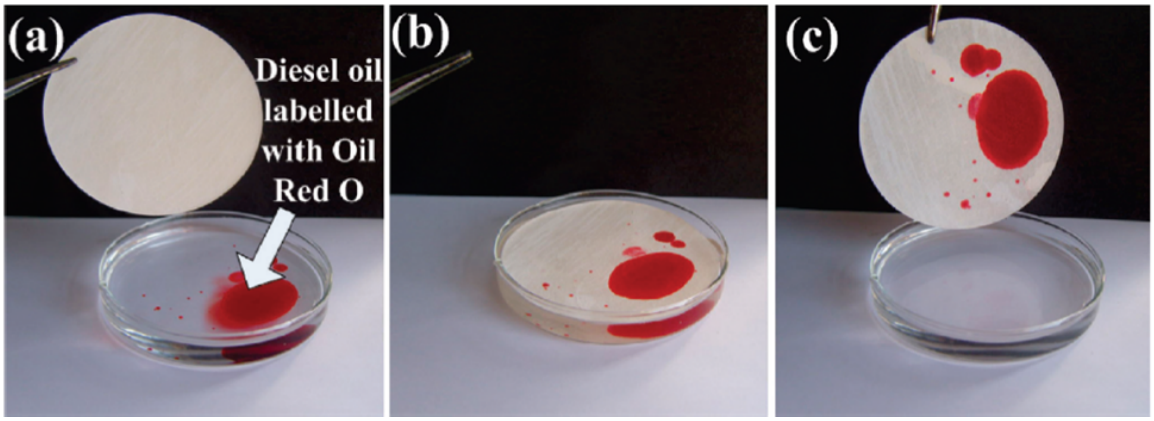

Figure 1.20: Removal of diesel oil from a water surface. The oil was labeled with Oil Red O for easy observation. [80]

1.3.4 Template for Other Superhydrophobic Surfaces

As a final application, paper has also found industrial use as a roughness template due to its low cost and durability. During the manufacture of certain vinyl surfaces and synthetic leathers, the hot plastics are pressed against a casting release paper. The paper transfers its roughness to the plastic, imparting the product with the specific roughness of the paper. [81] The roughness that is transferred is a function of the surface morphology of the release paper, which can be controlled through processing techniques. Using a similar methodology, Hou and Wang fabricated superhydrophobic polytetrafluoroethylene (PTFE) surfaces by pressing the polymer against filter

paper and then calcining the sample to remove the cellulosic material. [82] A variation in contact angle is observed for different calcining temperatures, with higher temperatures (400°C) reducing the static contact angle. Due to the properties of PTFE, the superhydrophobic surfaces created are chemically stable in a variety of solvents.

1.4 Outlook

Due to the range of potential benefits that superhydrophobic surfaces provide, potential applications have received considerable interest from both industry and academia. For the paper industry, wetting is a vital parameter in packaging, where fluid absorption leads to strength failure. superhydrophobic surfaces can prevent fluid absorption into the fiber web without the need for thick, expensive coating layers. The unique mechanical and renewable properties of cellulose-based substrates are uncommon in more popular inorganic superhydrophobic surfaces, making paper an attractive substrate. The application of superhydrophobic functionality to paper products has only recently been investigated, with the first report published in 2006. [38] Since then, researchers have applied a plethora of methods to attain the two principle requirements of all superhydrophobic surfaces: surface roughness of the right lengthscale and low surface energy. The roughness has been added through either bottom-up techniques, where roughness is deposited on fibers, or top-down methods, where surfaces are etched to expose roughness. Regardless of technique, the robustness of the roughened substrates is an important factor for industrial applications. Further development of these techniques to meet both the structural and scalability requirements of the paper industry is needed. Along with concerns regarding the structural integrity of the added roughness, the paper industry has shown interest in avoiding the use of fluoropolymer chemistries in their products, which has spurred interest in alternative polymer and wax chemistries that attain the low surface energy requirement. The

creation of superhydrophobic surfaces on paper has expanded their use into novel areas such as micofluidics and water/oil separations. Further, there is increased interest in the development of robust paper surfaces that are able to repel low surface tension fluids as well as water. As superhydrophobic fabrication techniques continue improve, paper has great potential to make its appearance in real world applications as a disposable, robust superhydrophobic substrate.

1.5 Thesis Outline

The goal of this thesis is to control fluid surface interactions through modifications and control of the physical and chemical surface properties.

Chapter 2 focuses on the printing of wax dots onto superhydrophobic paper to yield advanced microfluidic devices that can control the volume of fluid that is sampled. *Chapter 3* forms highly oleophobic paper by using a solvent exchange processing to increase the physical spacing between fibers. When combined with plasma etching and fluoropolymer deposition, superoleophobic paper is formed. *Chapter 4* creates highly oleophobic paper without using a solvent, thus allowing for the strength of the paper to be retained. Highly porous layers of paper were layered on regular paper to get the correct surface porosity. *Chapter 5* investigates the effect of the chemical surface energy on the contact angle. Superhydrophobicity is demonstrated with a hydrophilic surface coating of DLC when combined with oxygen plasma etching. *Chapter 6* applies the same requirements of physical roughness and low surface energy to stainless steel to create superhydorphobic stainless steel. *Chapter 7* discusses the conclusions of this thesis along with future recommendations for research.

CHAPTER II

HYSTERESIS CONTROLLED WATER DROPLET SPLITTING ON SUPERHYDROPHOBIC PAPER

Reproduced from L.Li, V. Breedveld and D.W. Hess, *Colloid and Polymer Science*, 2013, 291(2) pp. 417-426

2.1 Introduction

As previously mentioned in Section 1.3.2, superhydrophobic paper surfaces can combined with the printing of hydrophobic wax designs to create inexpensive, disposable microfluidic devices. In this section, we expand on previous work, showing the ability to sample volumes from droplets and control the volume sampled based on the contact angle hysteresis of the wax design.

Contact angle hysteresis occurs when the energy needed to separate a liquid and a solid interface exceeds the energy required to form a new interface. [83] Thus, manipulation of the hysteresis of a substrate is dependent on the ability to tune the interfacial interactions between the solid and the liquid phases through either chemical or physical surface modifications. Chemically, hysteresis is defined as an interaction that causes molecules at the interface to arrange differently when in contact with the liquid. [83, 84] This form of hysteresis typically occurs on surfaces that have both polar and non-polar groups, such as surfactants. Physical or mechanical hysteresis occurs by increasing the contact area between a surface and liquid. The most common approach is the addition of roughness to a surface, which increases the overall surface area. If the liquid wets the additional surface area, the increased interaction results in higher hysteresis. However, the combination of surface roughness at both micro and

nano-length scales can decrease wetting as well, in which case hysteresis is reduced.

By combining areas of high and low hysteresis on a single heterogeneous substrate, preferential adhesion of droplets to specific areas on the substrate can be achieved, and droplet mobility can be manipulated. [5] Wang *et al.* fabricated heterogeneous superhydrophobic surfaces using carbon nanotubes. Subsequently, they showed that they could preferentially adhere droplets to specific areas of the superhydrophobic surface by drawing patterns on it with a pencil, thus effectively covering the nanotubes with graphite. [85] Leopoldes *et al.* demonstrated preferential adherence of liquid jetted onto a chemically heterogeneous matrix of hydrophobic and hydrophilic areas [86]; based on their report, it appears that they not only varied contact angle, but also varied hysteresis by terminating the surface with either hydrophilic carboxyl groups (high hysteresis) or hydrophobic methyl groups (low hysteresis). Our research group has demonstrated control of droplet mobility on a surface by printing high hysteresis wax islands onto low hysteresis superhydrophobic paper. [60, 61] The preferential adhesion of droplets to the high hysteresis islands makes it possible to store, mix and sample droplets. It was proposed that controlled manipulation of droplets on the surface of superhydrophobic paper through wax pattern designs could yield two-dimensional microfluidic devices that are particularly attractive due to the versatility and ease of the printing method. Termed Hysteresis Enabled Lab on Paper (HELP), the proposed devices could enable inexpensive point-of-care diagnostics that would allow further off-site testing of liquid samples if needed. In order to perform accurate biomedical testing, it is crucial that sample volumes are well-defined and reproducible so that quantitative reactions with chemical reagents are possible, in particular if concentrations of analytes must be determined with high confidence levels. For example, there has recently been increased interest in the simultaneous testing for multiple illnesses from one droplet of bodily liquid on a single device. [87] In order to facilitate such characterizations, a bulk droplet must be split into several smaller droplets prior

to the analytical reactions; lack of droplet volume reproducibility will directly affect the outcomes of the testing.

In this paper, we present an approach to the sampling of small droplets from a larger bulk droplet by controlling contact angle hysteresis. Fabrication of a high hysteresis pattern on low hysteresis superhydrophobic paper enables control of the volume of the sampled droplet depending on the magnitude of the hysteresis. We control hysteresis, and thus volume sampled, through both chemical and physical surface modifications and show that the result of both approaches is fundamentally the same. This level of control will enable extraction of single and multiple sample droplets from a bulk droplet for biomedical testing.

2.2 Methodology

2.2.1 Fabrication of Superhydrophobic Paper

Paper handsheets were prepared according to the TAPPI standardized method T205 sp-02 using a 50/50 mixture of southern softwood kraft and southern hardwood kraft pulp. Superhydrophobic properties were established by etching the handsheets using oxygen in a parallel plate RF (13.56 MHz) plasma reactor for 45 minutes, followed by the deposition of 100 nm of fluorocarbon from a pentafluoroethane precursor (Praxair). Further details regarding the process parameters and reactor configuration during the fabrication of superhydrophobic paper substrates can be found elsewhere. [18]

2.2.2 Printed Patterns

Printing of the desired patterns was performed via a thermal transfer printing technique, using paraffin wax (Spectrum Chemical Mfg Corp., New Brunswick, NJ), carnauba wax (Alfa Aesar), stearic acid (Fluka, >97.0%) and mixtures thereof. Carnauba wax was selected due to its low apparent contact angle (97.3± 2.3°) relative to other waxes to help maximize adhesion; paraffin wax and stearic acid were chosen

based on their degree of polarity, lower and higher than carnauba wax, respectively. A transfer sheet was prepared by melting the wax of choice and then dip-coating a slip of standard copy paper into the liquid wax. Machined aluminum stamps with single dot and multiple dot patterns were created as shown in Figures 2.1 and 2.2. The dimensions of the patterns were chosen such that compression of a typical bulk droplet (50-100 μL) between the paper sheets results in an expansion of its diameter well beyond the edges of the printed pattern; the longest (diagonal) dimension of the largest pattern, the multiple dot design, was 5.65 mm. Figure 2.3 shows the transfer printing procedure using the stamp and transfer sheet. The wax dip coated sheet and the superhydrophobic sheet that needed to be printed were stacked on top of a glass slide with the superhydrophobic side facing down, away from the wax-impregnated sheet. The metal stamp, heated to a temperature above the melting point of the wax, was then pressed onto the stack and held down for 3-4 seconds, while the wax melted, absorbed into the superhydrophobic sheet and solidified in the shape of the stamp on the glass side of the printed sheet. The procedure resulted in a uniform wax coating throughout the depth of the sheet, with a coating of 10 μm covering the surface fibers (based on SEM images).

The insolubility of the waxes in water made it possible to reuse samples for 10 water droplet sampling experiments, so that reproducibility statistics and experimental error estimates could be established. However, stearic acids solubility in water limited use of those substrates to no more than two experiments, with further sampling resulting in small but noticeable droplet volume inconsistencies.

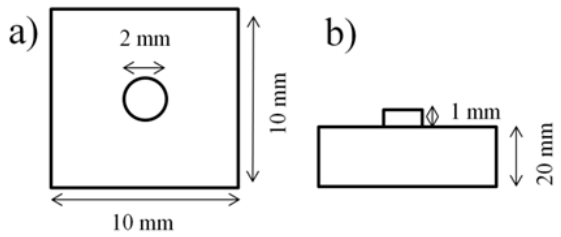

Figure 2.1: Single dot stamp design dimensions a) vertical view b) side view.

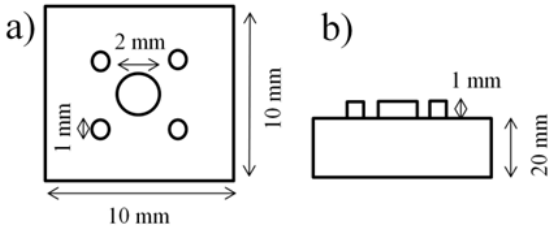

Figure 2.2: Multiple dot stamp design dimensions a) vertical view b) side view.

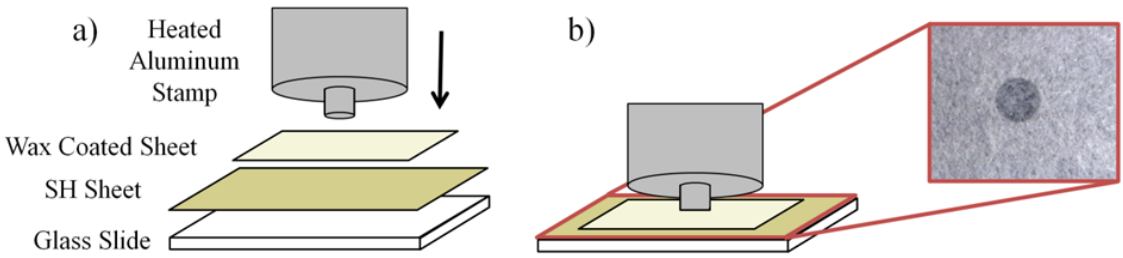

Figure 2.3: Stamping procedure a) Wax coated sheet and superhydrophobic sheet stack on top of a glass slide b) heated stamp pressed into the stack, wax melts through the superhydrophobic paper in the shape of the stamp.

Physical roughness was added to the wax surface on the printed substrates by pressing the cooled wax onto various grades of sandpaper. Sandpaper roughness is

characterized via the grit number that is specified through the Coated Abrasive Manufacturers Institute (CAMI) standards, with higher grit numbers corresponding to finer particles. The sheets we used (Norton brand; Saint-Gobain Abrasives, Stephenville, TX) were manufactured using aluminum oxide particles (with grit numbers of 100, 150, 220, 320, 400 and 600) and silicon particles (for the 1200 grit paper). X-ray photoelectron spectroscopy was performed on the patterned superhydrophobic paper samples before and after pressing with sandpaper to ensure that no transfer of grit particles to the wax had occurred; in these tests, no presence of Si or Al could be detected on the roughened wax surfaces.

2.2.3 Droplet Sampling

Sampling tests were conducted using a squeeze testing unit that moves a platform vertically to compress a 100 μl bulk droplet between two superhydrophobic sheets, as illustrated in Figure 2.4. An important component with regards to the consistency of droplet transfer is the parallelism of the two sheets, which is needed to avoid uneven droplet compression and release. In order to achieve the necessary parallelism, the vertical slide is attached to a base plate with three adjustable screws that enable adjustment of the top plate in relation to the bottom platform on which the bulk droplet rests. The rebound of the vertical slide occurs in 0.5s and is controlled by a spring that is compressed as the slide is moved downward. Droplet splitting is observed to occur in three steps: 1) compression of the droplet, 2) necking of the droplet and 3) pinch-off. These steps can be seen in Figure 2.4b), c) and d) respectively.

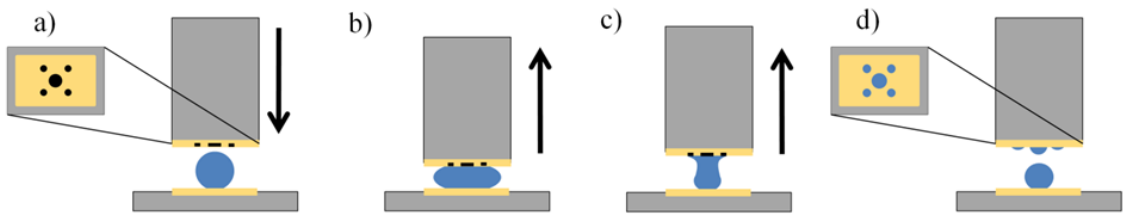

Figure 2.4: Squeeze test procedure a) droplet between two superhydrophobic pieces of paper; the top paper has a printed design b) droplet is compressed and released c) droplet forms a neck d) droplet splits and water samples are transferred onto printed pattern.

2.2.4 Image Analysis

After the transfer is complete, the top plate, along with the vertical slide and patterned sheet are inverted and an image taken of the sample droplets using a Lumenera LU135c camera, equipped with a Leica A6 APO zoom lens. Images are taken at an angle of 15° relative to the horizontal plane, so that it is possible to view all the droplets at once on a multi-dot design array, while obtaining accurate data on the droplet dimensions. The resulting image is analyzed using the image analysis software package IDL (ITT Visual Information Solutions, Boulder, CO), which measures the lengths of the major and minor axes of the drop through user inputs. From the lengths of the major and minor axes of the droplet, its volume can be calculated using Equation 2.1; V is the volume, h the height of the droplet and c the radius of the contact line between droplet and paper.

$$V = \frac{\pi}{6} h(3c^2 + h^2) \tag{2.1}$$

Calibration tests with droplets of known volumes established the accuracy of this image analysis procedure for droplets of various sizes and contact angles as ± 0.03 μL. Each data point presented in this paper is the average of 40-80 droplet splitting

experiments and error bars in the graphs represent the standard deviation.

2.2.5 Contact Angle Measurement

Apparent (static) contact angles were measured with a Rame-Hart contact angle goniometer (Model 100, Netcong, NJ) using 4 μL water droplets. Advancing contact angles were measured using a 2 μL droplet and increasing the volume by 1 μL increments until the volume reached 10 μL. Receding contact angles were measured using a 5 μL droplet and decreasing the volume by 0.5 μL until the volume reached 2 μL.

Substrates for contact angle measurements of the various wax materials were prepared by melting the pure and mixed solid waxes and dip-coating slips of standard copy paper. For the measurement of physically modified hysteresis, the wax-coated slips of paper were pressed against sandpaper after cooling.

2.2.6 SEM Images

Scanning electron microscope (SEM) micrographs were obtained with a Hitachi S-3700N VP-SEM, using the variable pressure mode at a pressure of 80 Pa and an operating voltage of 15 kV.

2.2.7 Profilometry

Roughness data were obtained using a Wyko Optical Profilometer NT2000. Four measurements were taken for each sample and analyzed using the Vison32 (Vecco Instruments Inc.) analysis software. The average roughness, R_a, is calculated as per the ANSI B46.1 standard and the mean peak spacing, S_m, is defined as the mean spacing between peaks along the measured line profile.

2.2.8 Glucose Experiments

The reagents for colorimetric glucose experiments were prepared by pipetting 1 μL of 645 U/mL glucose oxidase (Sigma Aldrich), 1 μL of 339 U/mL horseradish peroxidase (Sigma Aldrich) and 0.5 μL of a 2:1 molar mixture of 3,5 dichloro-2-hydroxybenzenesulfonate (Sigma Aldrich) and 4-aminoantipyrine (Sigma Aldrich) onto each of the four perimeter islands of the multi-dot design. The reagents were allowed to dry overnight on the islands in a dry box. Sampling experiments were conducted using the procedure outlined above with 100 μl droplets of 0.0015M and 0.005M glucose solutions prepared by dissolving d-glucose (Sigma Aldrich) in DI water.

2.3 Results and Discussion

2.3.1 Chemical Hysteresis

Figure 2.5 presents the dynamic contact angles and the contact angle hysteresis for homogeneous substrates of five different waxes: pure paraffin wax, a 1:1 mixture (by mass) of carnauba and paraffin wax, pure carnauba wax, a 1:1 mixture of carnauba wax and stearic acid, and pure stearic acid. While the advancing contact angle of each of the solids is similar, the hysteresis varies widely. The variation in hysteresis is due to differences in the chemical compositions of the materials. Paraffin wax is largely composed of straight chain saturated alkanes ranging from 20 to 40 carbons in length. [88] Carnauba wax, on the other hand, is composed of alkanes, along with aliphatic esters, monohydric alcohols and acids 25 to 30 carbons in length. [89] The esters, alcohols and acids found in carnauba wax have a stronger interaction with water than do the non-polar alkanes that make up paraffin wax. This enhanced interaction results in a chemically increased contact angle hysteresis for carnauba wax relative to paraffin wax. The 1:1 mixture of carnauba and paraffin waxes exhibits a higher than expected hysteresis close to that of pure carnauba wax. Due to the amorphous and crystalline structures of carnauba and paraffin waxes, respectively,

and the differences in melting points, 82-86°C for carnauba and 47-65°C for paraffin, phase separation of the waxes could occur upon solidification. Alternatively, it is expected that the addition of paraffin wax alkanes to carnauba wax will result in a change in packing of surface groups, which may influence the hysteresis. While the exact cause of the increased contact angle hysteresis is unclear, the low variability observed in hysteresis measurements suggests that if surface heterogeneity exists, it must be at a length scale much smaller than that of the droplet. Stearic acid not only has the shortest chain length of the pure substances, 18 carbons in length, but also is entirely composed of molecules with polar groups. These factors cause stearic acid to have the strongest interaction with water, and thus the highest hysteresis.

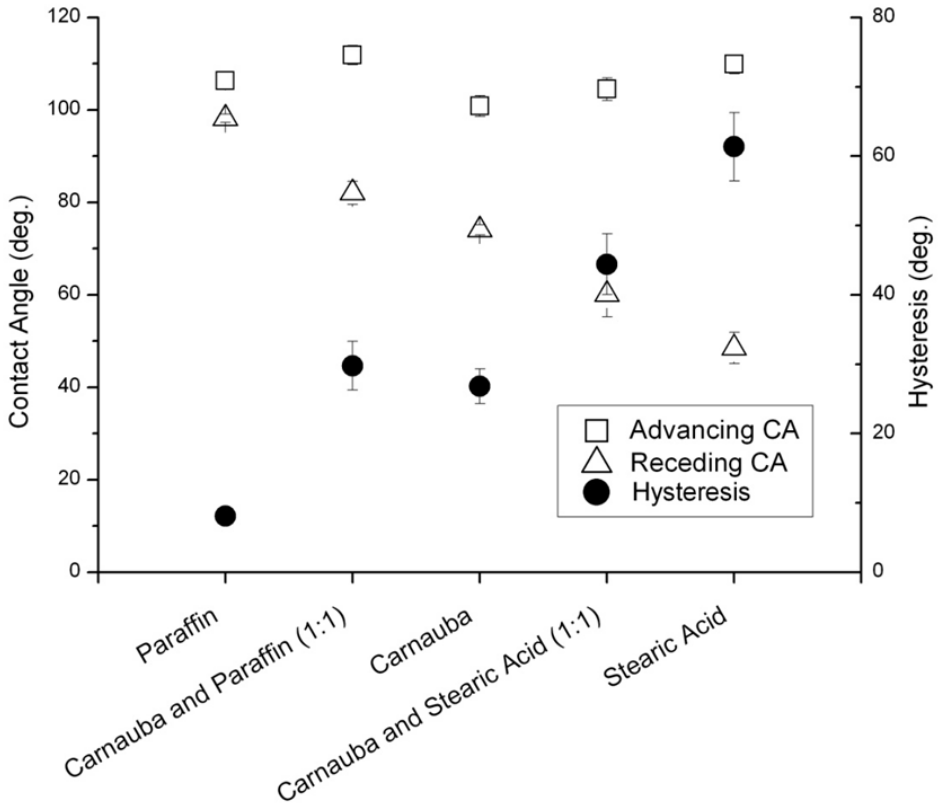

Figure 2.5: Plots of advancing and receding contact angles and contact angle hysteresis of several sample types.

Using the wax materials indicated in Figure 2.5, single dot designs were fabricated on low hysteresis superhydrophobic paper and droplet splitting was used to extract samples from bulk droplets of DI water. The sampled volumes are presented in Figure 2.6; clearly, the droplet volume depends upon the chemical hysteresis, with increasing droplet sizes for larger hysteresis values. To illustrate the difference in sampled droplets more clearly, images from the droplet splitting experiments are shown in Figure 2.6. As hysteresis is increased, both the lateral and vertical dimensions of the sampled droplet increase.

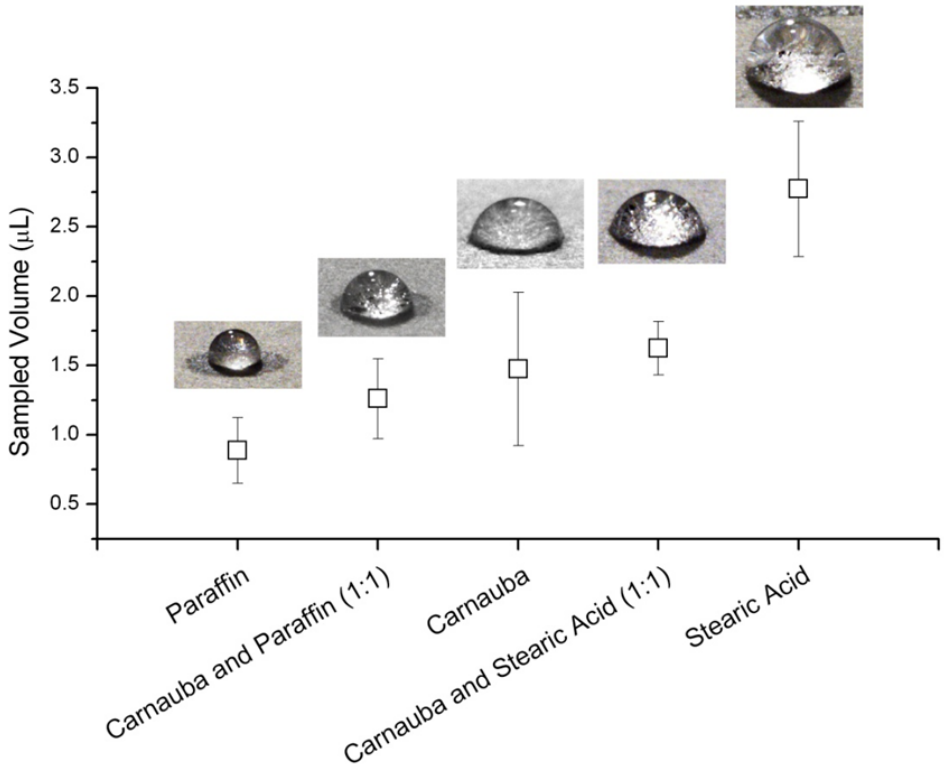

Figure 2.6: Sampled volumes for several types of waxes used for printing; pattern was a 2 mm diameter circle.

2.3.2 Physical Hysteresis

In order to modify the physical hysteresis of printed substrates, surface roughness was added to the printed wax dots. The substrates for studying physical hysteresis were fabricated using pure carnauba wax. By pressing the cooled wax designs against various grades of sandpaper, the wax deformed and generated a range of physical surface roughness. Figure 2.7 shows SEM images of a selection of carnauba wax designs on superhydrophobic paper before and after pressing against various grades of sandpaper. The correlation between grit number and CAMI average particle size on the sandpaper surface can be found in Table 2.7. For the larger particles, corresponding to lower grit numbers (100-220), the pressing not only deforms the wax, but also significantly deforms the fibers (Figure 2.7b) and c)).

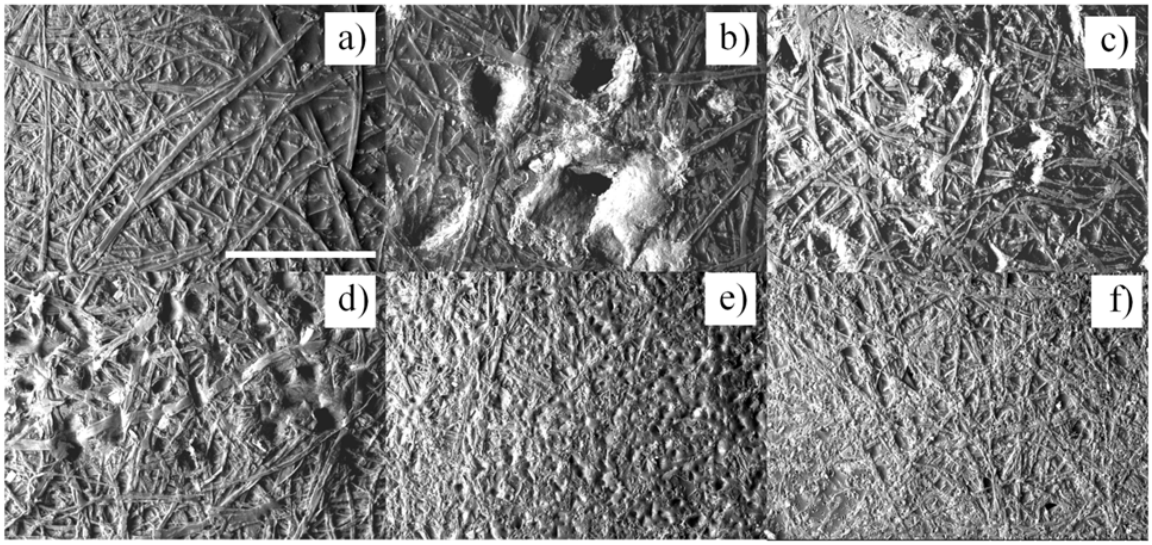

Figure 2.7: SEM images of carnauba wax on low hysteresis superhydrophobic paper after being imprinted with various grades of sand paper: a) untreated reference, b) 100 grit, c) 150 grit, d) 220 grit, e) 600 grit, f) 1200 grit. Scale bar represents 500 μm.

Table 2.1: Correlation of sandpaper grit designation to average particle size (according to CAMI standard), and the average roughness (R_a) and mean spacing (S_m) measured via profilometry.

CAMI Grit Designation	100	150	220	320	400	600	1200
Average Particle Size (µm)	140	92	68	36	23	16	6.5
R_a (µm)	24.1	13.8	13.7	10.5	7.5	5.6	3.6
S_m (µm)	57.6	56.8	17.3	16.7	15.1	14	11.3

Figure 2.8 shows that the hysteresis increases as the grit number increases and particle size decreases, while advancing contact angles remain approximately constant. This indicates that the scale of the physical roughness is an important factor in the increase of hysteresis. Johnson and Dettre have performed detailed analysis on the effect of surface roughness on contact angle hysteresis. [90] Their findings suggested that at certain length scales, increased surface roughness yields an increase in hysteresis. Bhushan *et al.* studied contact angle hysteresis on an array of silicon pillars. [91] These authors found that hysteresis was dependent on a non-dimensional spacing factor $S_(f)$, which was defined as the ratio of the pillar diameter to the distance between the pillar centers. With the sandpaper, not only is the size of the particle changed as the grit number changes, thus changing the amplitude of the roughness, but the mean distance between the particles is varied as well. The average roughness (R_a), along with the mean peak spacing (S_m) for the tested sandpaper grades, is shown in Table **??**. Initially, with coarser grits of sandpaper, the distance between the particle peaks, and therefore the indentations, is too large to have an effect on the contact angle hysteresis. As the particles become smaller, the spacing between indentations

decreases. At this lowered length scale, the added physical roughness starts to affect contact angle hysteresis. Much like the case of increasing chemical hysteresis (Figure 2.6), the increase of physical hysteresis also increases the sampled volume, as seen in Figure 2.9.

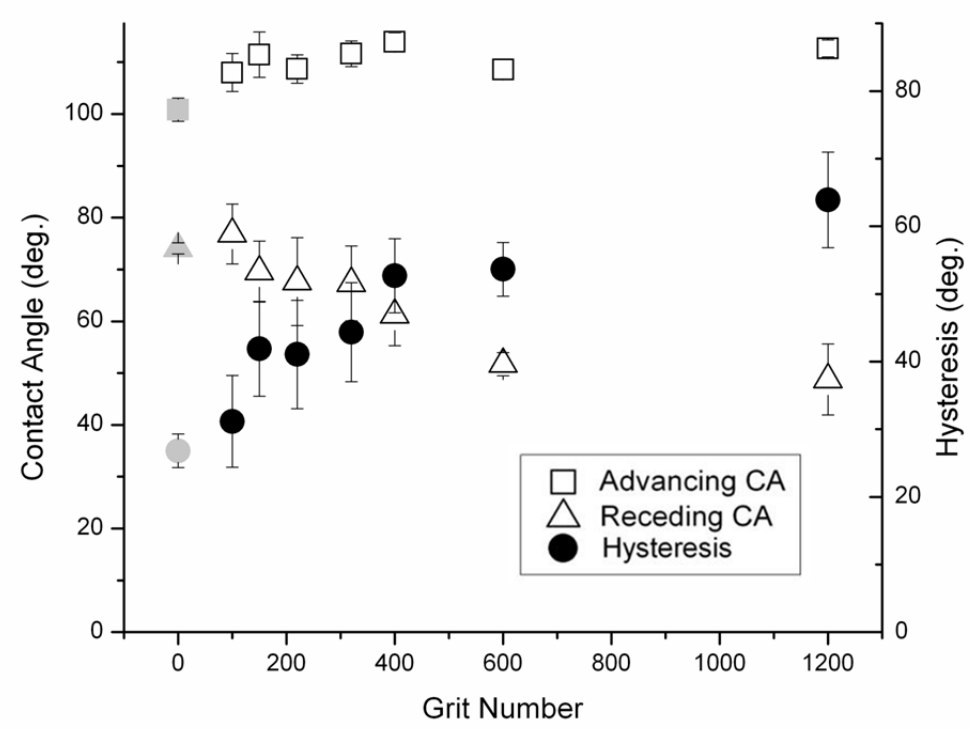

Figure 2.8: Advancing and receding contact angles, along with contact angle hysteresis of carnauba wax impregnated substrates that were pressed onto various grades of sandpaper. Gray data points represent measurements made on unmodified carnauba samples.

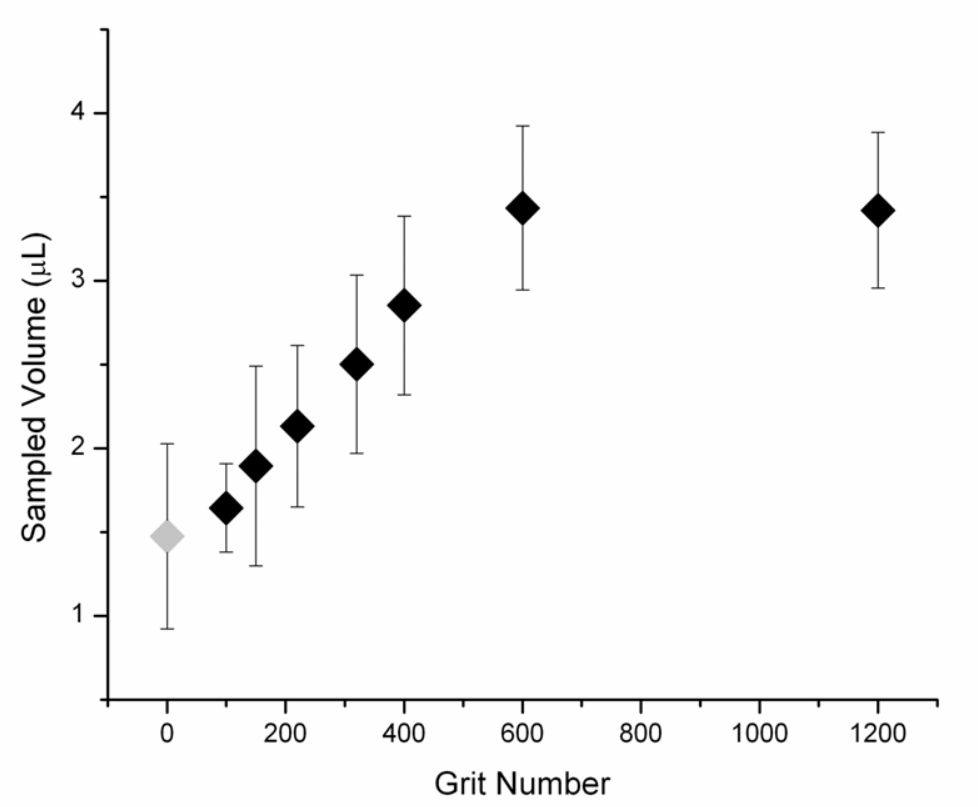

Figure 2.9: Sampled droplet volume as a function of the grit number of the sandpaper used to impart roughness. Gray data point represent measurement made on unmodified carnauba sample. Wax dots of 2 mm diameter were used for these experiments.

2.3.3 Relationship Between Sampled Volume and Hysteresis

Comparison of Figure 2.6 and Figure 2.9 indicates that the sampled droplet volume increases with hysteresis, independent of the method used to modify this surface property. To further test this hypothesis, Figure 2.10 presents the volume of sampled droplets obtained through splitting for both chemical and physical surface modification methods against the wax substrate hysteresis. Good agreement is observed between the two sets of data. A least squared linear regression line is also shown in Figure 2.10, further demonstrating the strong correlation between the sampled volume and the hysteresis.

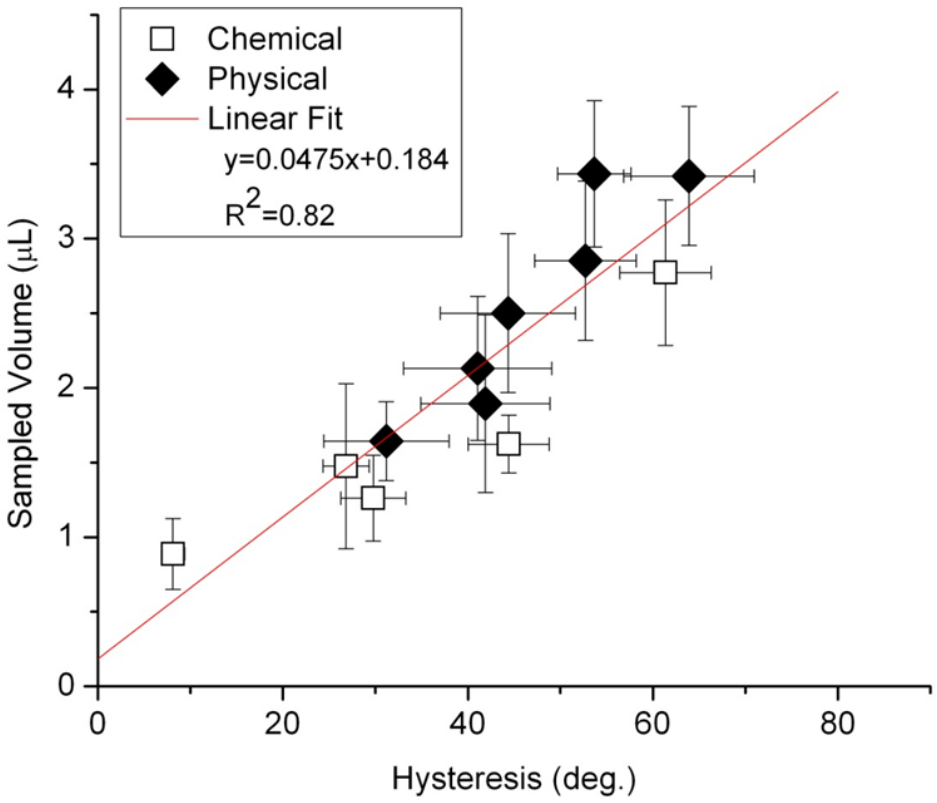

Figure 2.10: Plot of sampled volume versus hysteresis of chemically and physically modified samples.

The similarity between the two methods of hysteresis control is a result of the underlying physics that governs the splitting of a bulk droplet. During the droplet release phase (Figure 2.4 b) and c)), the bulk droplet effectively recedes across the top sheet. On a zero hysteresis upper surface, the droplet continues receding unhindered, and no splitting is expected to occur due to gravity and surface tension. By adding patterned wax islands with high hysteresis to a low hysteresis surface, the droplet is able to recede easily across the top surface until it encounters the edges of the printed wax dots. The difference in hysteresis between the surrounding superhydrophobic paper and the wax pattern results in an additional force that enables droplet splitting. While gravity pulls the droplet downward, away from the top surface, and surface

tension resists the deformation of the bulk droplet from its spherical ground state, the adhesion force due to the hysteresis of the wax pattern favors droplet splitting. The end result of this force balance depends on the remaining contact area, i.e. size of the wax pattern and location of droplet breakup. Previous study showed that during transfer of bulk droplets between low hysteresis surfaces and high hysteresis wax islands, the droplets were always pinned at the circumference of the printed dot. Furthermore, the maximum droplet volume that could be transferred was a function of the dot size, as predicted through a simple force balance. [60] In this investigation, however, we study the splitting of bulk droplets and show that the contact angle hysteresis of the printed patterns also plays a critical role in this case. On a low hysteresis island, for example pure paraffin, the droplet can continue to recede past the edge of the pattern and droplet splitting occurs in a small contact area. By increasing the hysteresis of the pattern, droplet pinning is promoted across a larger surface area of the printed dot, which leads to greater adhesion forces, and thus larger droplet volumes after splitting. The images in Figure 2.6 show an increase in the droplet contact area as the hysteresis increases due to the pinning action of the increased hysteresis. While the contact angle hysteresis of the printed dots can theoretically be increased to 180°, its effect on the sampled volume is limited. At a hysteresis of 60°, the sampled droplet is already pinned at the circumference of the wax pattern, as seen in Figure 2.6. Without increasing the area of the printed dot, no additional force can be applied by the island to promote droplet sampling. Figure 2.9 shows that although the hysteresis is increased from 53.6 ± 3.9° to 63.9 ± 7.0°, the sampled volume is not increased between 600 and 1200 grit pressed samples.

Similarly, it is anticipated that as the dot size is decreased, a limit will be reached where the droplet cannot be split, since the dot does not provide sufficient adhesion force to overcome the surface tension force of the bulk droplet as it deforms. Below this minimum radius, regardless of the hysteresis, the dot is unable to sufficiently

deform the droplet to cause sampling. Experimentally, this minimum could not be determined using carnauba wax due to resolution limitations of the printing technique and stamp fabrication. Calculation of the minimum dot size is a nontrivial task due to the complexity of the droplet breakup dynamics, which strongly depends on the shape and curvature of the deformed drop prior to breakup. Nevertheless, the existence of a minimum dot size was proven by using higher resolution printed wax dots created with a Xerox Phaser 8650 printer; in these experiments with a commercial, proprietary wax mixture, it was observed that a dot size of 150 μm was too small to enable fluid sampling.

2.3.4 Multi-dot Stamping

The ability to control sampled droplet volume by printing high hysteresis patterns onto low hysteresis superhydrophobic paper is not limited to the relatively simple single dot designs presented above. Adjusting the design to include five dots by using the stamp in Figure 2.2, bulk droplets can be split into five samples, as shown in Figure 2.11. The multiple-dot wax design has a larger 2 mm diameter wax island in the center, and four smaller 1 mm diameter wax islands surrounding it. The size difference between the central and surrounding islands is important for the uniformity and reproducibility of the droplet splitting process. As the patterned substrate is pulled away from the bulk droplet, the liquid recedes along the top surface. Further separation between the sheets causes the droplet to become pinned and split at each printed dot, one at a time, until the droplet is only attached to top substrate in one location. After this point, any further separation between the substrates will cause a final split that fully detaches the bulk droplet from the patterned substrate. The receding liquid will release last from the printed wax feature on the top substrate that provides the strongest adhesion; by purposely placing a larger dot in the center of the multi-dot design, the release process is stabilized and uniform droplet splitting

is realized from the outer islands. As expected, adding physical roughness to the wax islands by pressing the multi-dot patterns onto sandpaper again correlates to an increase in sampled volume, as shown in Figure 2.12.

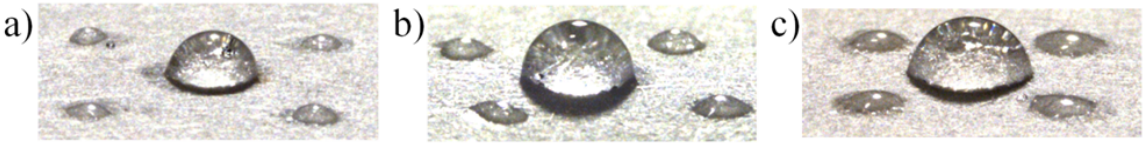

Figure 2.11: Images of multiple dot designs fabricated with carnauba wax and a) unmodified, b) pressed with 320 grit sandpaper and c) pressed with 600 grit sandpaper.

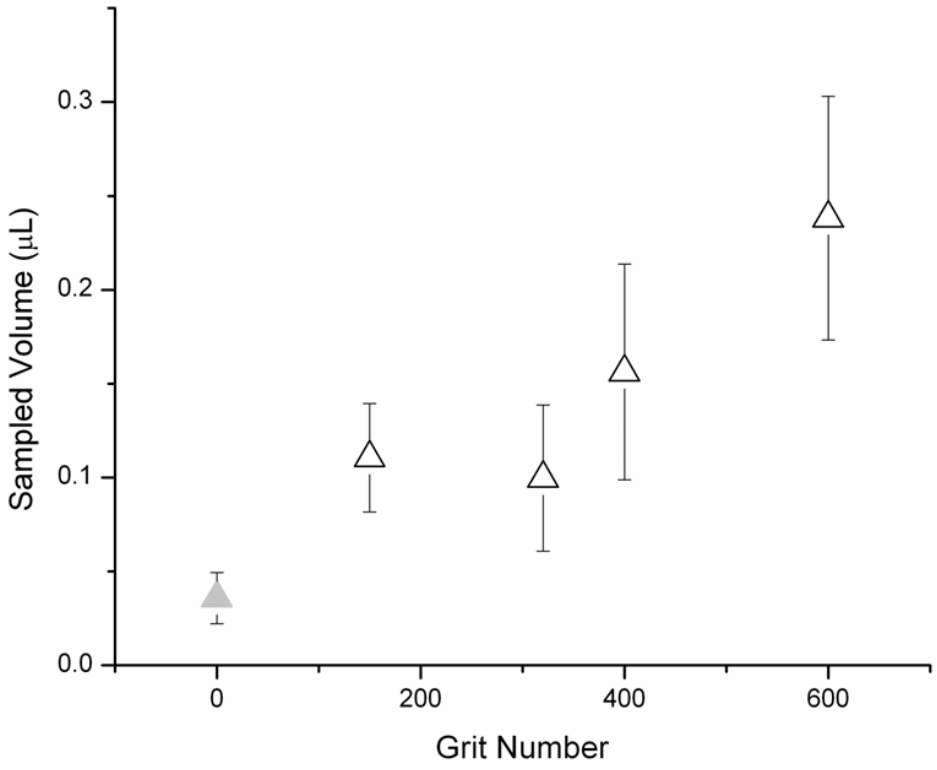

Figure 2.12: Plot of volume sampled versus grit for the 4 perimeter island in a multiple dot design. Gray data point represents measurement made on unmodified carnauba sample.

The ability to split single bulk droplets into several smaller sample droplets of well-defined volume permits the use of paper substrates in HELP applications. Martinez and coworkers have investigated the use of paper substrates for point-of-care biomedical testing [73, 74] through the fabrication of microfluidic devices. In these studies, lithographic techniques were used to create isolated hydrophilic cellulose channels with hydrophobic barriers between them. Fluids were then wicked into the paper via capillary flow towards reagents at the ends of the channels. Paper is inexpensive, biodegradable and available worldwide, making it an attractive substrate for these one-time-use biomedical applications. Using HELP techniques, colorimetric reagents can be either deposited on the high hysteresis islands or chemically incorporated into the islands themselves. Incorporation of the reagents into the island, for example via grafting or noncovalent specific binding interactions, would enable testing of non-transparent liquids, such as blood, because a post-test washing step can be performed. Figure 2.13 shows a proposed procedure for the splitting and testing of a blood sample. If the colorimetric reagents are not incorporated into the island, step e) would be impossible and a transparent liquid would be needed to properly gauge a colorimetric change.

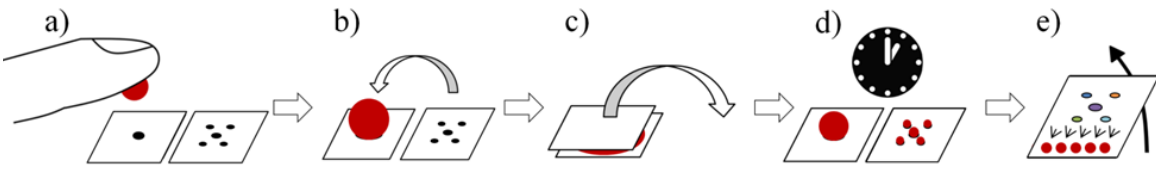

Figure 2.13: Procedure for HELP biomedical testing: a) patient places droplet of blood on superhydrophobic sheet, b) compress blood droplet using another superhydrophobic sheet with a colorimetric design array, c) remove colorimetric sheet (difference in contact angle hysteresis allows sampling), d) wait for reaction to occur, e) remove blood droplets from design array and view diagnosis through colorimetric changes.

To demonstrate the capacity of HELP techniques to enable colorimetric biochemical tests, a glucose immunoassay was conducted. The testing of glucose concentrations in blood and urine is a well developed technique, extensively studied in the 1940s. [92] The immunoassay uses chemical reagents that result in a change in color intensity, the magnitude of which can be correlated to glucose concentration. By drying glucose colorimetric reagents on each perimeter island and then sampling from bulk droplets of our test liquids (DI water, and glucose solutions at 0.0015M and 0.005M; see Figure 2.14), the ability of the HELP technique to perform colorimetric tests can be assessed. This technique can easily be extended to other immunoassays with the advantage that each island of the multi-dot pattern can be treated with a different reagent, thus enabling different tests to be simultaneously performed on a single substrate. Additionally, with the ability to control the volume of the sampled droplets through hysteresis, it is possible to tune the volumes of the droplets sampled by each island separately, depending upon the requirements of the biological test.

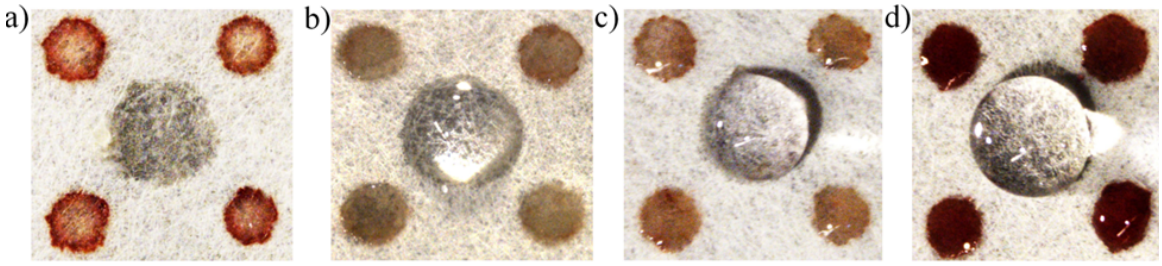

Figure 2.14: Procedure for HELP biomedical testing: a) patient places droplet of blood on superhydrophobic sheet, b) compress blood droplet using another superhydrophobic sheet with a colorimetric design array, c) remove colorimetric sheet (difference in contact angle hysteresis allows sampling), d) wait for reaction to occur, e) remove blood droplets from design array and view diagnosis through colorimetric changes.

2.4 Conclusions

The ability to control the volume of water droplets split from a bulk drop using high hysteresis wax islands printed on low hysteresis superhydrophobic paper has been demonstrated. The volume sampled is dependent on the magnitude of the wax island hysteresis. Chemically, hysteresis was adjusted through control of the active chemical groups present on the surface of the printed island. Physical hysteresis was controlled through the addition of surface roughness by pressing various grades of sandpaper into the wax surface without affecting the surface chemistry. A good correlation was observed between the sampled volume and the hysteresis, independent of the method of hysteresis modification. The increase in sampled volume with increasing hysteresis is due to the force balance that evolves during the droplet splitting process. By increasing the hysteresis the droplet is pinned to a higher surface area of the wax island, resulting in stronger adhesion and a higher sampled volume.

Control of the volume of sample droplets through physical hysteresis modification

was extended to the simultaneous extraction of multiple sample droplets from a single bulk droplet by using a more complicated multi-dot array on the top substrate. The reproducibility of this technique for splitting off droplets with a well-defined volume from a bulk droplet of test liquid enables quantitative colorimetric biomedical tests, as we demonstrated by performing a colorimetric glucose immunoassay. These studies indicate that by applying different colorimetric reagents to each island, it will be possible to perform multiple biomedical tests simultaneously on a single lab-on-paper device. The ability to control volume also enables the integration of immunoassays with varying volume requirements, thereby allowing multiple quantitative analyses to be performed on the same substrate.

CHAPTER III

DESIGN AND FABRICATION OF SUPERAMPHIPHOBIC PAPER SURFACES

Reproduced from L.Li, V. Breedveld and D.W. Hess, *ACS Applied Materials & Interfaces*, 2013, 5(11) pp. 5381-5386

3.1 Superoleophobic Properties on Paper

While significant research has been conducted on the highly water repellent surfaces utilized in Chapter 2, the ability to support oil contact angles of >150° has only recently been realized. The difficulty of creating these highly oil repellent surfaces remains the difference in surface tensions between water and oils. The majority of superhydrophobic surfaces are unable to support elevated contact angles for reduced surface tension fluids such as oils; as a result, highly oil repellent (superoleophobic) surfaces with static oil contact angles greater than 150° are generally difficult to achieve unless carefully engineered surface structures are used. [21, 57, 93]

Our investigation focuses on the development of paper substrates that simultaneously exhibit superhydrophobic and superoleophobic properties; such universally non-wetting substrates are often referred to as superamphiphobic. [94] The critical parameters for these superamphiphobic surfaces are a specific combination of low surface energy and reentrant surface structures. [21] Such surfaces have been constructed on rigid inorganic substrates through nanoscale fabrication techniques, commonly resulting in delicate, brittle structures. [93, 95–97] Figure 3.1a shows these reentrant angle containing structures, where α is the reentrant angle.

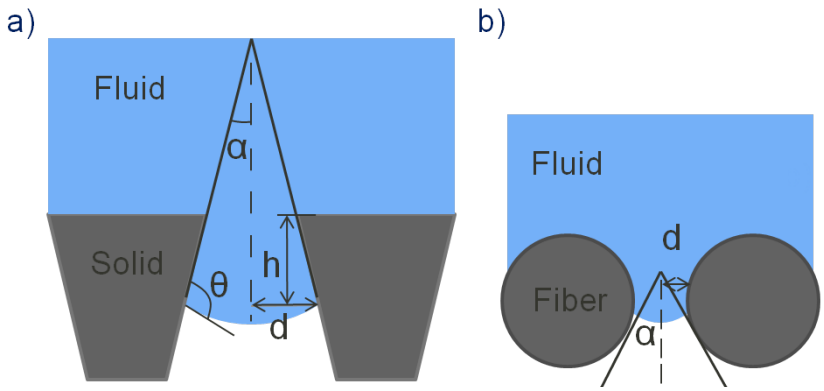

Figure 3.1: a) Structured surface showing reentrant angle and b) the same reentrant angle on a fiber based structure. α is the reentrant angle, θ is the equilibrium contact angle, h is the depth of fluid penetration and d is half the distance between the structures

In contrast, paper is a biodegradable, renewable, inexpensive material that is produced worldwide on an industrial scale. The aforementioned properties and broad availability of paper have led to expansion of its use in novel, technologically advanced fields, such as paper-based microfluidics in the biomedical industry. [74, 98] However, the naturally occurring hydrophilic and oleophilic properties of cellulose-based paper continue to greatly restrict the scope of its applications. In order to inhibit water absorption, our group [18, 60] and others [9, 51] have developed surface modifications of common paper substrates to attain superhydrophobic properties. Despite the advances made through these studies, superoleophobic fiber based paper has yet to be reported. Cellulose-based superoleophobic surfaces have been reported in the form of aerogels [99, 100] and cellulose-coated structured silicon, [101] but these substrates lack the availability and manufacturability of traditional paper. Spray coating of paper has also been utilized to create superoleophobic surfaces, but this approach relies entirely on the coating properties rather than exploiting the inherent properties of the fiber network. [102] Jin *et al.* have demonstrated amphiphobicity on filter paper

using liquid treatments to generate the necessary roughness and hydrophobic surface chemistry; however, fiber structure requirements were not described nor discussed, and the study was limited to filter paper, which is a specialty paper in the sense that it is designed to withstand prolonged exposure to liquids. [103] Oil repellent paper products that can be manufactured via scalable processes are of great interest for the paper industry, with applications in fluid and materials packaging. Perhaps even more important is the opportunity to expand the use of paper products into other fields such as the biomedical industry where disposable, bacteria resistant surfaces and test strips can be envisioned. [103]

Past studies have demonstrated that attainment of superoleophobicity relies heavily on distinct roughness geometries. [21, 104–107] Specifically, the contact angles of low surface tension fluids are enhanced by surface structures with reentrant angles. To simplify the manufacturing process for creating reentrant structures and expand the scope of available substrate materials, researchers have turned their attention to fiber and wire based substrates with well-defined, uniform, ordered repeat structures. The salient aspect here is that the bottom half of a cylindrical fiber offers reentrant angles or overhang constructs that are similar to lithographically created structures, seen in 3.1b. Exploiting this concept, superoleophobic surfaces have been developed on highly ordered, uniform mesh screens and woven fabrics. [21, 108–113] These studies have highlighted the fact that the critical physical parameters of superoleophobic substrates are the dimensions and spacing of the structures.

The most commonly cited models to describe wetting behavior on roughened surfaces are the Wenzel [33] and Cassie-Baxter [34] models. In the Wenzel model, fluid is assumed to be in complete contact with the enhanced surface area generated by roughness, whereas in the Cassie-Baxter state the droplet is supported by air pockets trapped between the surface structures, thus reducing the liquid-solid contact area. In

order to attain high oil contact angles on a surface, the fluid must maintain a Cassie-Baxter wetting state. [21,93,97] To model fiber-based substrates, modifications to the Cassie-Baxter equation have been made to yield:

$$cos\theta^* = \frac{D(\pi - \theta^e)}{L} cos\theta^e + \frac{D}{L} sin\theta^e - 1 \tag{3.1}$$

where the apparent contact angle (θ^*) is a function of the center-to-center distance between two fibers (L), the fiber diameter (D) and equilibrium contact angle (θ^e). [109, 114, 115] The size and spacing of surface structures can easily be varied when produced lithographically, while for fiber based mesh screens and woven fabrics, L and D are established by the manufacturing process, fiber size, and weave. However, many surfaces of significant scientific and technological interest do not have such well-defined structures.

Herein we present an approach to the design and fabrication of superamphiphobic paper substrates that exploits the physical properties of the heterogeneous fiber web. This novel achievement is accomplished by systematically altering the average fiber size and inter-fiber spacing through a combination of techniques: fiber refining prior to paper formation, solvent exchange during paper formation, and plasma processing post-treatment of the paper. Beyond the inherent hydrophilicity and oleophilicity of cellulose fibers, the greatest challenge in fabricating superamphiphobic paper remains the creation of fibrous structures with the correct length scales. At the micrometer scale, paper is composed of cellulose fibers that are heterogeneously spaced and randomly oriented. Highly oleophobic substrates made from randomly oriented fibers have proven non-trivial to produce. [21, 104, 116] Unlike previous reports, which utilize uniform polymeric fibers, nature constrains our options by supplying cellulosic fibers for paper production only in specific size ranges. To compound the difficulties, processed fibers are often not circular in shape, but ellipsoidal (see inset in Figure 3.4a). These factors combine to define paper as a complex material with randomly

oriented and sized fibers that that display a surface structure that contrasts greatly with the carefully crafted, highly ordered superoleophobic surface geometries that have been reported to date.

3.2 Experimental Methods

3.2.1 Pulp Refining

For this chapter two fiber types were used: southern hardwood Kraft (Alabama River Pulp Co.) and southern softwood Kraft (North Carolina International Paper). The fibers were refined according to TAPPI standardized method T 248 sp-08, [117] whereby dry fiber sheets were soaked in deionized water overnight and then loaded in a PFI (Pulp and Fiber Research Institute) refiner (Test Machines Inc.) and exposed to different levels of refining as defined by the number of revolutions.

3.2.2 Handsheet Formation

Handsheets were formed using two different methods. When processed with water, handsheets were formed following TAPPI standardized method T 205 sp-02, whereby the refined pulp is lowered in consistency and then drained under gravity onto a mesh screen. The handsheet is subsequently pressed and dried overnight on a stainless steel plate. For handsheets made using sec-butanol (Alfa Aesar, anhydrous, 99%), the refined pulp is first drained through a 75 μm pore mesh screen. The water filtrate is discarded and sec-butanol (100 mL) is added to the drained pulp. The pulp is then remixed for 2 min. and again drained through a 75 μm screen. After the sec-butanol/water mixture has drained from the pulp, the sheet is pressed and then dried overnight on a stainless steel plate.

3.2.3 Plasma Etching and Fluoropolymer Deposition

Paper samples were etched and subsequently exposed to fluorocarbon film deposition in a parallel plate (13.56 MHz) vacuum plasma reactor. Both steps were conducted

at 110°C using a power of 120W. To etch the paper, oxygen was introduced to the reactor at 75 standard cubic centimeters per minute (SCCM), and allowed to reach an equilibrium pressure of $5.0\text{x}10^{-1}$ torr. The fluoropolymer coating was deposited using a plasma composed of 40 SCCM Ar and 20 SCCM pentafluoroethane (Praxair) at an operating pressure of 1.0 torr. While etch times were varied, the deposition step was constant at 2 min, for all studies described below, yielding a coating thickness of 400 nm. More detailed descriptions regarding the procedure and reactor configuration can be found in previous publications. [18]

3.2.4 Contact Angle Measurements

All static contact angle measurements were performed by placing a 4 μL droplet of the selected fluid (DI water, ethylene glycol (BDH, reagent grade), motor oil (SAE 10W-30, MotoTech) or n-hexadecane (Sigma-Aldrich Co., 99%)) onto the paper surface and then recording an image using a Lumenera LU135c camera equipped with a Leica A6 APO zoom lens. Contact angle analysis was performed using the DropSnake program in ImageJ image analysis software (NIH). This method was used in lieu of a standard goniometers fitting program largely due to poor modeling of droplets of low surface tension fluids which, even at the relatively small volumes analyzed in this study, become aspherical at high contact angles.

3.2.5 SEM Imaging

All samples subjected to scanning electron microscopy (SEM) imaging were sputter coated with Ag/Pd to mitigate charging effects. Images were taken with a Zeiss Ultra60 FE-SEM at an electron energy of 5.0 keV.

3.2.6 Profilometer Measurements

Measurements were conducted using a Wyko NT2000 Optical Profilometer. R_a values were analyzed using the Vison32 sofware (Veeco Instruments Inc.), calculated per the

ANSI B46.1 standard. Surface coverage analysis was conducted by processing the raw profilometer height profiles in MATLAB (The Mathworks, Inc.) by applying filtering and thresholding procedures on the height profile data to identify the top fiber layer.

3.3 Results and Discussion

3.3.1 Fiber Types

One of the most basic ways to modify the properties of paper, such as strength and porosity, is to change the type of fiber that is used. The two primary types of wood pulp have different physical dimensions, with fibers from softwood trees having a greater fiber length and diameter when compared to fibers from hardwood trees. Figure 3.2 shows SEM images of a) hardwood and b) softwood fibers, highlighting the discrepancy in their diameters. Softwood pulp is most commonly found in paper products where strength is imperative, while hardwood fibers are more commonly used to ensure a smooth interface.

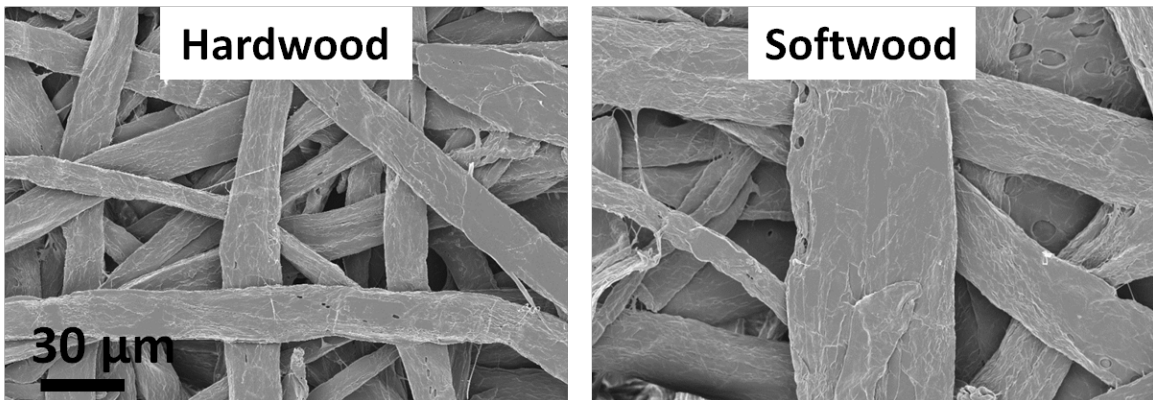

Figure 3.2: Comparison of a)hardwood and b) softwood fibers

To probe the effect that fiber diameter (parameter D in Equation 3.1) has on the oleophobic property of paper, handsheets were made using pulp from softwood and hardwood trees. Previously our group has demonstrated superhydrophobic properties by plasma etching and coating paper substrates of equal mixture of softwood and

hardwood fibers. [60] Handsheets made from an even mixture of pulps, along with handsheets made from only hardwood and softwood fibers were also created and tested for oleophobic properties. Figure 3.3 shows the change in a) water, b) motor oil and c) n-hexadecane contact angles, respectively, against etch times. All samples appear to attain their maximum contact angles at lower etch times, and decrease as etch time is increased, with the HW and HW/SW handsheets absorbing oil after 90 minutes of etching. This failure of the HW containing sheets is due to the damage that the extended etch causes to the fiber after 90 minutes. SEM images (not included) demonstrate that the HW fibers are more susceptible to destruction than the SW fibers. With enough etching, fibers eventually weaken to a point where they collapse under the weight of the fluid droplet, causing the wetting to switch to the Wenzel state. While, there is a difference between the etch time to failure, Figure 3.3 demonstrates that natural fiber radius differences alone cannot provide a large enough change the paper porosity to significantly effect the n-hexadecane contact angle.

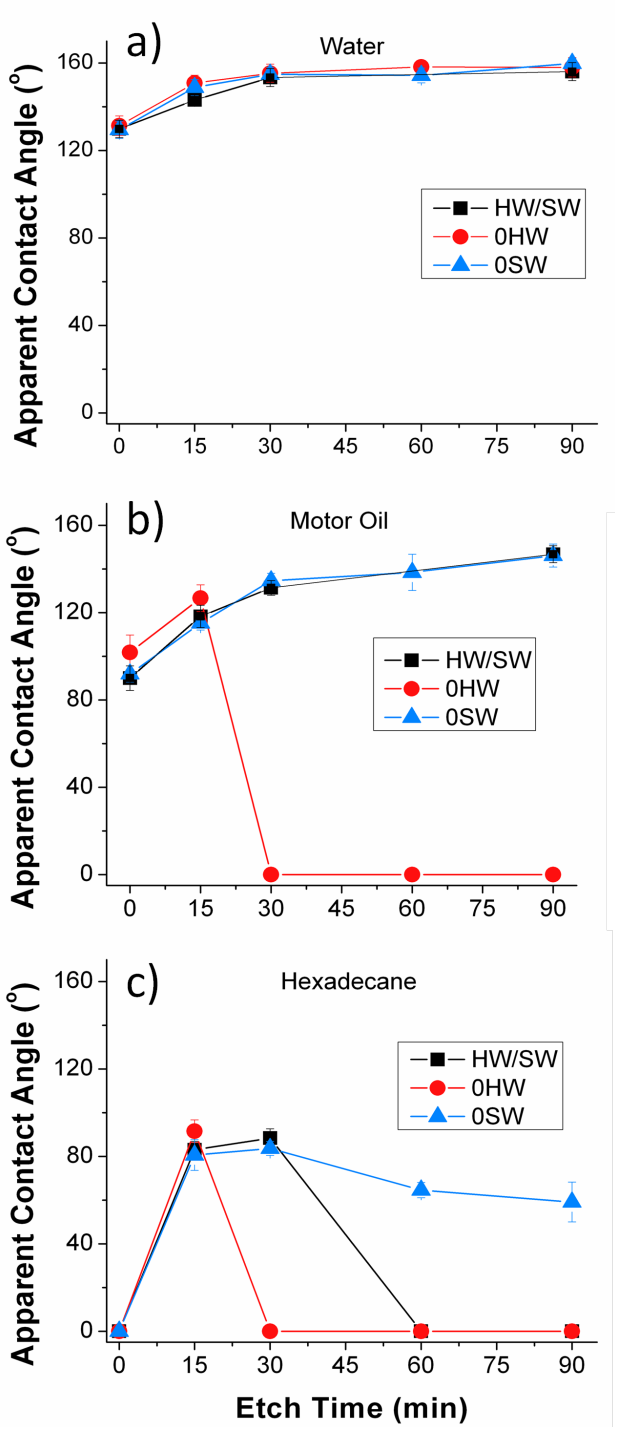

Figure 3.3: Contact angles of a) water, b) motor oil and c) *n*-hexadecane on handsheets made from hardwood (0HW), softwood (0SW) and a 50/50 mixture of the two (HW/SW)

3.3.2 Fiber Refining

To gain further control of the fiber spacing (L) and diameter (D) parameters of paper, pulp refining was applied. Industrially, refining is a commonly practiced technique used to increase the uniformity and strength of paper products; fibrous pulp is ground between metal gears, thereby shearing or fibrillating the individual fibers. Figures 3.4a and b show scanning electron micrograph (SEM) images of an unrefined and refined hardwood fiber, respectively. The refined fiber shown in Figure 3.4b was processed using the special solvent exchange process discussed below to illustrate the effect of refining on an individual fiber. An increase in refining intensity ultimately separates fibers into their elementary components, so-called fibrils (see Figure 3.4b), much like a braided rope can be deconstructed into many smaller diameter cords. In order to ensure that our studies solely investigate the physical effects of the fibers, and not the properties of chemical modifiers and fillers present in commercial paper products, we create our own paper substrates without additives. Our paper substrates, composed of only natural wood fibers, are termed handsheets in this manuscript. Figures 3.5a to f present SEM images and roughness profiles measured with optical profilometry for handsheets made from hardwood pulp subjected to varying levels of refining. In the following discussion, we will classify the substrates by designations that contain the number of revolutions (in thousands) experienced in the PFI refiner and wood type (i.e., handsheets made from hardwood pulp exposed to 3,000 revolutions are denoted 3HW). SEM and profilometer data indicate that increased refining intensity leads to less porous handsheets, in which individual fibers become difficult to identify. At high refining levels, hydrogen bonding between fibrils (seen in Figure 3.4b) creates agglomerates that fill interstitial pore spaces in the fibrous network, leading to a smoother appearance of the handsheet. Refining thus offers control over the size distribution of the fibers, characterized by parameter L in Equation (3.1).

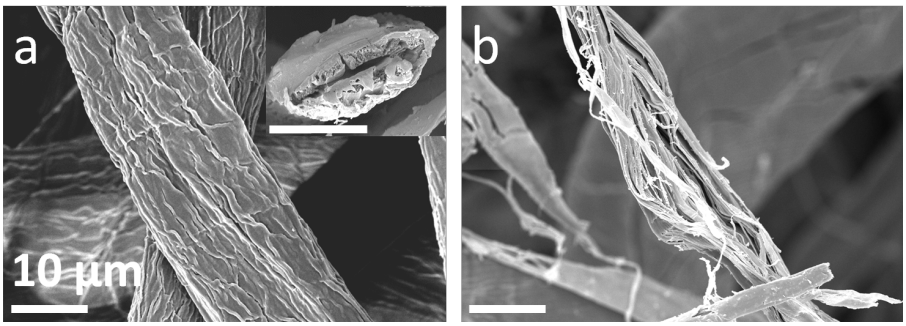

Figure 3.4: SEM images of a) unrefined and b) refined fibers, highlighting the effects of refining on the fiber structure. Inset in a) depicts the cross-section of an unrefined fiber. Scale bars represent 10 μm.

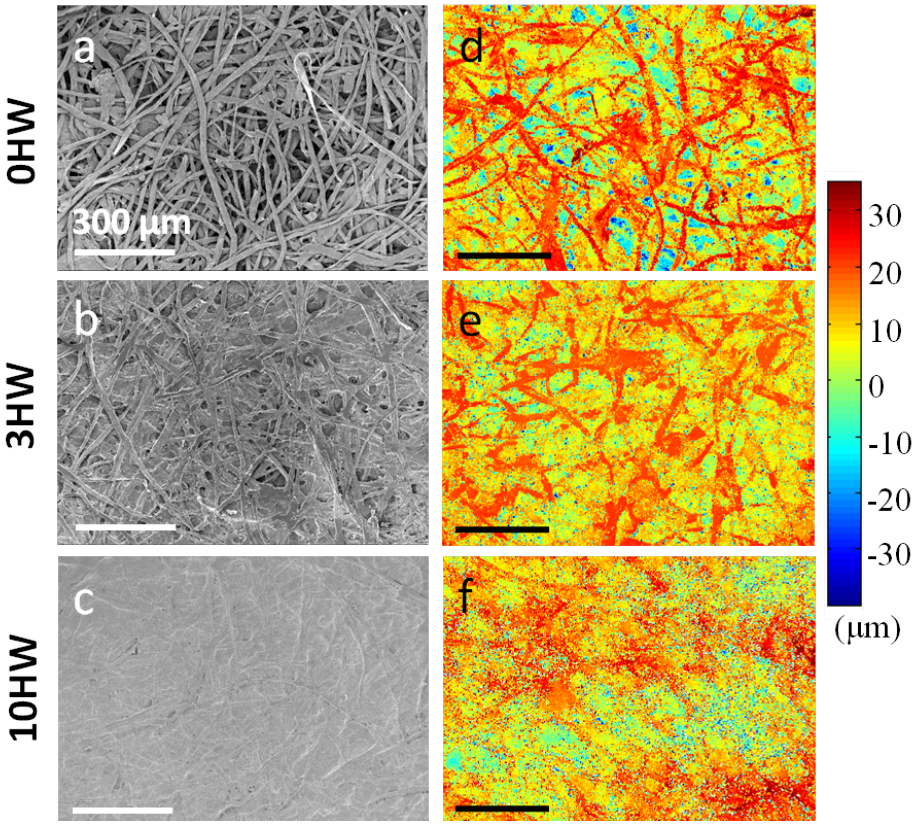

Figure 3.5: SEM images of 0, 3, and 10HW handsheets are shown in a)-c), respectively, demonstrating that increased refining smooths the handsheet surface. Complementary profilometer images are presented in d)-f). All scale bars correspond to 300 μm.

The next challenge to achieving superamphiphobic paper surfaces is to control the inherent wetting properties of the fibers. In previous work, our group has used plasma etching to selectively remove the amorphous phase of cellulose, leaving behind crystalline phase protrusions from the fiber surface. This process creates nano-scale roughness on the surface of individual fibers, and micrometer-scale roughness after extended etch times. When followed by plasma deposition of a fluorocarbon film from a pentafluoroethane precursor, the two-step process renders the surface superhydrophobic. [18] In this study, handsheets made from 0, 1, 3, 5 and 10HW pulp

were etched for different durations, followed by deposition of a 400 nm fluoropolymer film. After 15 minutes of etching (and fluoropolymer deposition), all handsheets exhibit superhydrophobic properties (see Figure 3.6a), but the wetting behavior for oils shows much greater diversity and dependence on etch time. Static contact angles of motor oil (γ_{lv} = 32.2 mN m^{-1}) [118] and *n*-hexadecane (γ_{lv} = 27.5 mN m^{-1}) on handsheets with various levels of refining are presented in Figures 3.6b and c as a function of etch time. While these two fluids have similar surface tensions, their contact angles are drastically different for the same processing conditions. Utilizing n-hexadecane as a test fluid, short etch times yield a large increase in contact angles, with a 15 min etch time changing 0, 1, 3 and 5HW handsheets from completely absorbing to slightly oleophobic. We believe that this increase in contact angle is due to the formation of a dual-scale, hierarchical surface when nano-scale roughness formed by the plasma etching is combined with the micrometer-scale roughness of the fiber network. Figure 3.7 shows SEM images of a 0HW handsheet etched for various times, with and without a fluoropolymer deposition. Clearly, as etch time is increased to 30 min, nanoscale roughness is formed on individual fibers, and after 90 min of etching, the fibers have been etched to a skeletonized version of the original fiber. The reduction of *n*-hexadecane contact angles to a zero value at the longer etch times is due to fiber destruction, causing the fibrils to collapse under the weight of a droplet; this results in a wetting transition from the Cassie-Baxter to the Wenzel state. In comparison with handsheets formulated from pulp subjected to other refining levels, 10HW handsheets behave quite differently. Figures 3.6a-c demonstrate that 10HW handsheets are relatively unaffected by plasma etching, neither increasing nor decreasing the contact angles significantly for either fluid. This atypical behavior results from the large number of fibrils that agglomerate to form a dense, continuous surface for the highly refined sample (see Figure 3.5c). In fact, the measured contact angles are similar to the equilibrium contact angles for n-hexadecane ($\theta^e_{(n-hexadecane)}$=

$42 \pm 2°$) on a flat silicon wafer after plasma deposition of the same fluoropolymer. Thus, while increased refining yields a greater number of small diameter fibrils, strong inter-fiber hydrogen bonding binds them together, resulting in a smooth, non-porous surface. To effectively utilize the refined fibrils to stabilize the Cassie-Baxter state, clustering must be inhibited.

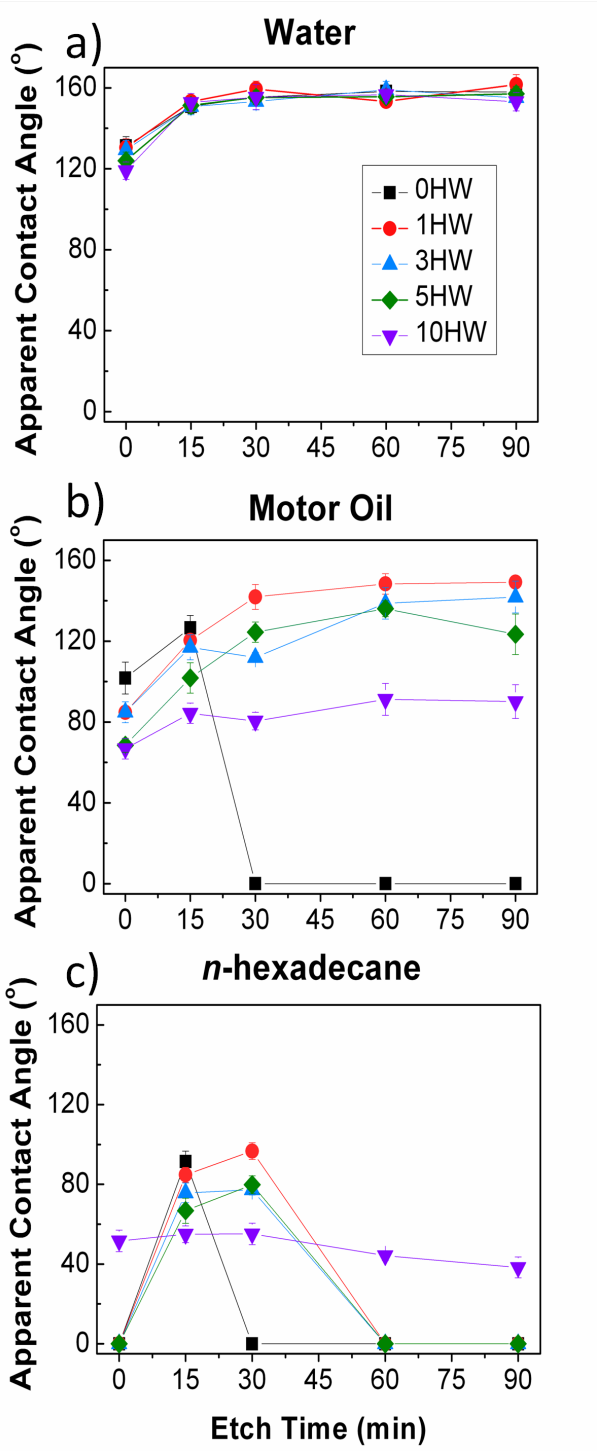

Figure 3.6: Apparent contact angle measurements of a) water, b) motor oil and c) n-hexadecane for handsheets made from pulp at various refining levels as a function of oxygen plasma etch time.

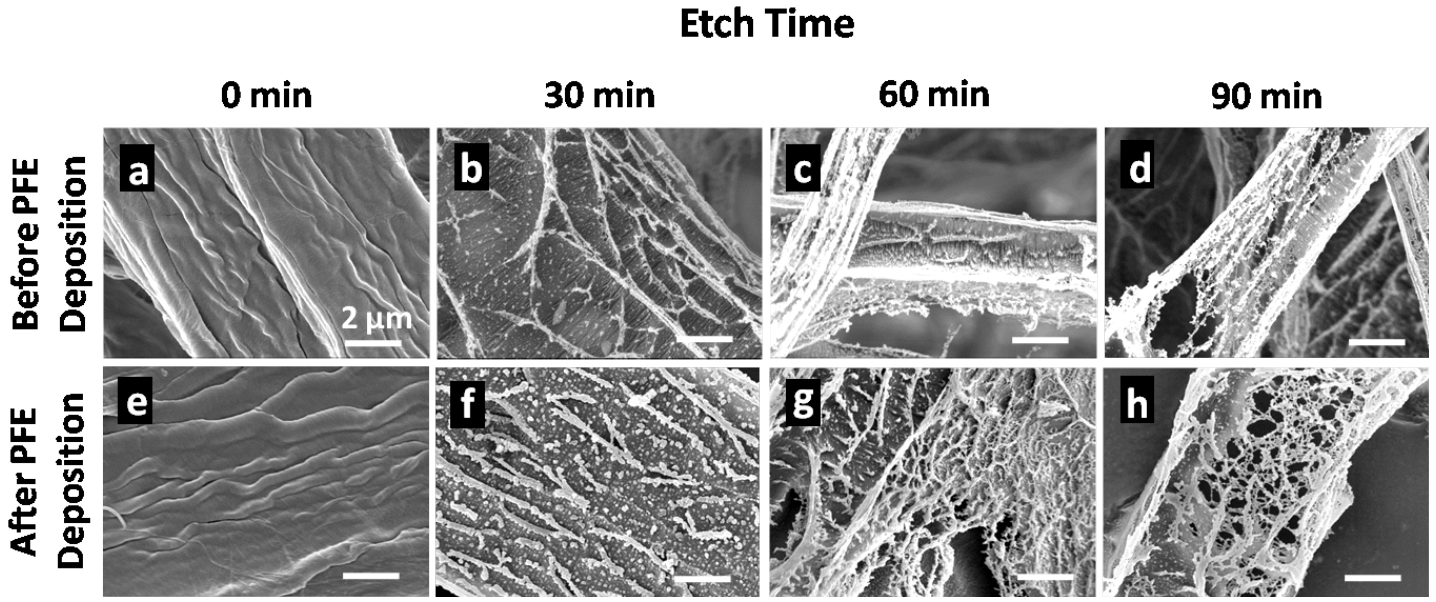

Figure 3.7: SEM images of fibers that have been etched for a) and e) 0 min, b) and f) 30 min c) and g) 60 min and d) and h) 90 min, before and after deposition of 400 nm of PFE.

3.3.3 Solvent Exchange Processing

To enhance the separation of fibers and fibrils (parameter D in Equation (3.1)), we employ a solvent exchange method, whereby the fibrous pulp is drained of water and then added to sec-butanol; the pulp is then drained of the sec-butanol and dried without subsequent exposure to water. Organic solvents have been demonstrated to prevent hydrogen bonding between cellulosic fibers. [118,119] In our case, sec-butanol is employed to prevent the fibrils created during the refining process from binding together, thereby significantly increasing the sheet porosity. However, by inhibiting fiber-fiber hydrogen bonding, a decrease in the strength of the handsheet is also observed; this effect will be quantified in subsequent studies. Comparison of Figures 3.8a and 3.5a underlines the dramatic difference between the structure of handsheets made from 10HW pulp when processed with sec-butanol and water, respectively. A higher magnification image of a sec-butanol processed handsheet (Figure 3.8b) clearly reveals the separation of micron and sub-micron scale fibers. Figure 3.9 presents the variation of contact angle with etch time on these handsheets for four liquids: water, ethylene glycol (γ_{lv} = 48.4 mN m^{-}1), motor oil and n-hexadecane. Without etching, deposition of a fluoropolymer layer is sufficient to render the sec-butanol-formed handsheets superhydrophobic, but the sheets readily absorb oils. After 5 minutes etch time followed by fluorocarbon deposition, stable contact angles can be measured for motor oil, and after 10 minutes etch time followed by fluorocarbon deposition, hexadecane droplets are repelled. Etching for 30 minutes followed by fluorocarbon deposition yields a surface that supports θ^* >150° for all four test fluids (θ^*_{water}=157 ± 3°, $\theta^*_{ethyleneglycol}$= 155 ± 5°, $\theta^*_{motoroil}$= 152 ± 4°, $\theta^*_{n-hexadecane}$= 154 ± 2°). Samples are observed to maintain high contact angles and repellency for 5 days. Figure 3.8c presents an SEM image of this surface and Figure 3.10 shows a picture of all four test fluids resting on a single handsheet. Slide-off angles (ω) of 6 μL fluid droplets on the surface depicted in Figures 3.8c and 3.10 are as follows: ω_{water}= 13

$\pm$ 3°, $\omega_{ethyleneglycol}$ = 19 $\pm$ 4°, $\omega_{motoroil}$ = 34 $\pm$ 6°; n-hexadecane droplets remain pinned on the surface even after inversion. Droplets of water, ethylene glycol and motor oil can be removed without leaving residual fluid on the sheet, but a stain of n-hexadecane remains on the surface when the droplet is withdrawn. The staining by n-hexadecane is likely due to the fact that although a high apparent contact angle is observed, the droplet resides in essentially a Wenzel wetting state, leading to higher adhesion to at least some of the supporting fibers. To our knowledge, this is the first report of a superamphiphobic fiber-based paper substrate that uses the inherent structure of the paper and control of the paper-making process to achieve specific wetting properties.

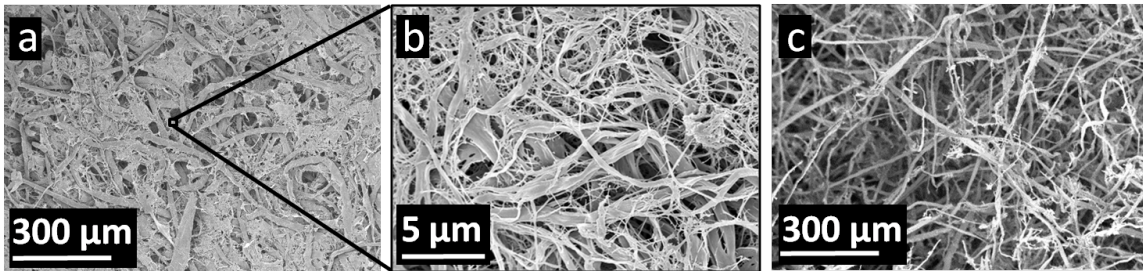

Figure 3.8: a) and b) show low and high resolution SEM images of a 10HW handsheets processed using sec-butanol before etching. c) presents an image of the same material after 30 minutes of plasma etching.

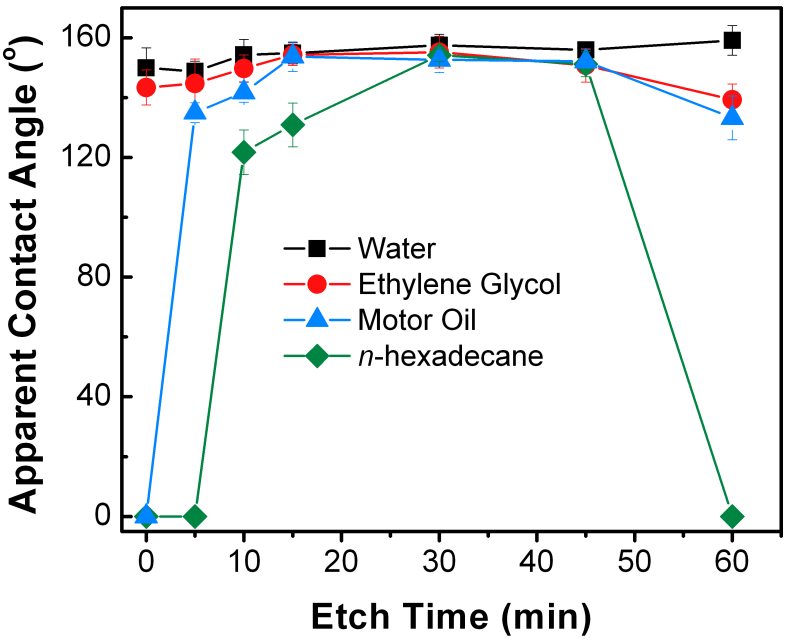

Figure 3.9: Contact angles of water, ethylene glycol, motor oil and n-hexadecane versus etch time for 10HW handsheets made with sec-butanol. After 30 minutes of etching, handsheets demonstrate superhydrophobic and superoleophobic properties for all fluids.

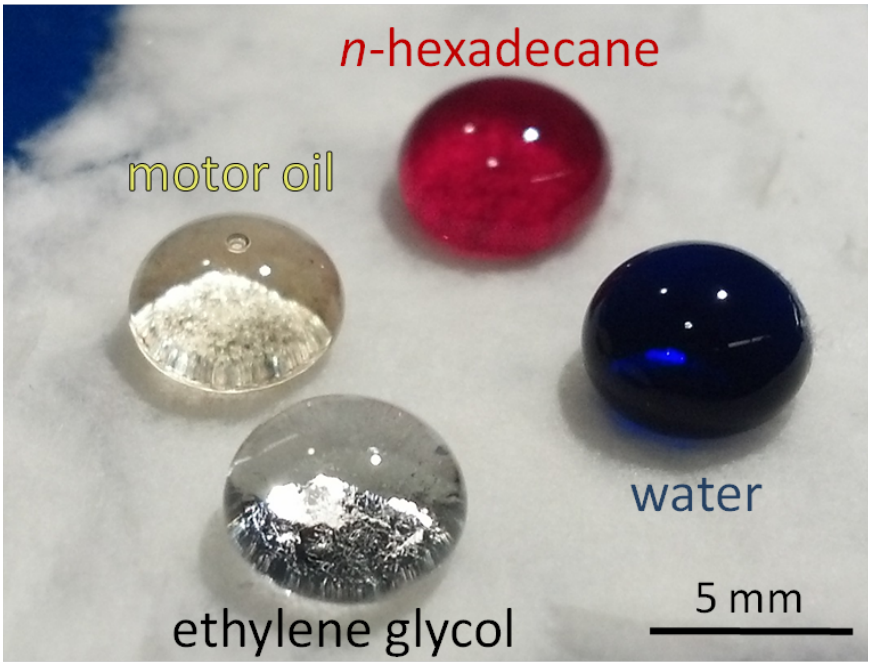

Figure 3.10: Droplets of four test fluids (water (dyed blue), ethylene glycol, motor oil and n-hexadecane (dyed red)) are shown resting on the same handsheet depicted in Figure 3.8c), exhibiting high contact angles for all fluids.

From SEM images, it is evident that both the solvent exchange and plasma processing steps increase the handsheet porosity. To quantify these effects, Table 3.1 presents profilometer measurements of 0, 3 and 10HW handsheets prepared with water and sec-butanol that have been used to establish the average roughness (R_a) and the areal coverage of the top layer of fibers. R_a is presented in lieu of fiber surface area since it is a measure of the surface properties of the paper substrate, whereas fiber surface area measures bulk properties, which may not always be representative of the topmost layer of the paper that dominates liquid-fiber contact. A dramatic increase in R_a is observed between 10HW handsheets drained with water and sec-butanol. This increase in Ra is critical to maintain the Cassie-Baxter wetting state, since low roughness enables the fluid to contact fibers below the surface layer, thereby causing

a transition to the Wenzel state. The surface porosity is indicated by measurements of the surface coverage, where lower values correspond to a more porous surface structure. Initially, the water and sec-butanol 10HW handsheets exhibit relatively similar coverage values. It is only after etching that the coverage is reduced, creating the necessary porosity to support low surface tension fluids in the Cassie-Baxter state. Although Equation (3.1) proved very useful in this research as a guide to establish the necessary fiber size and spacings needed for superoleophobicity, a quantitative comparison with our measurements is not straightforward and is beyond the scope of the work presented here. Determining the fiber spacings in a three-dimensional network of randomly oriented fibers with a broad size distribution and non-cylindrical shapes (see inset in Figure 3.4a) is a non-trivial task. SEM images and profilometer data presented above provide some insight, but do not characterize the three dimensional geometry in sufficient detail to enable modeling. Furthermore, it is unclear how to interpret this information, in light of the fact that wetting models have to date only been developed for structured substrates with well-defined length scales; [32,120] for example, the average fiber spacing and size may have little physical meaning with regards to quantitative predictions of wetting properties, which are likely dominated by the extremes of the size and spacing distribution rather than their means. Nevertheless, we can conclude that Equation (3.1) is useful for the development of less-structured fibrous substrates with great practical relevance for a variety of wetting scenarios.

Table 3.1: Average roughness (R_a) and areal coverage of the top layer of fibers for 0, 3 and 10HW handsheets under different processing conditions (water vs. sec-butanol, variable etch times). R_a values reflect the height difference between the surface layer and underlying fiber layers; areal coverage values represent the surface porosity of the handsheets.

Handsheet Type	Processing Fluid	Etch Time (min)	Roughness (R_a) (μm)	Areal Coverage of Top Layer of Fibers (%)
0HW	water	0	9.2 ± 0.5	77.3 ± 1.4
3HW	water	0	6.0 ± 0.6	85.2 ± 2.6
10HW	water	0	4.7 ± 1.1	99.8 ± 0.2
10HW	*sec*-butanol	0	31.7 ± 3.9	85.2 ± 0.7
10HW	*sec*-butanol	15	52.2 ± 5.4	69.5 ± 4.9
10HW	*sec*-butanol	30	53.6 ± 3.6	49.9 ± 8.7
10HW	*sec*-butanol	45	53.7 ± 3.6	54.5 ± 1.5

3.4 Conclusion

In summary, we have developed a novel method to design and create paper or cellulose-based natural materials that are superamphiphobic: simultaneously superhydrophobic and superoleophobic. Pulp refining creates the appropriate diameter fibers that help stabilize the Cassie-Baxter wetting state. However, when handsheets are fabricated by draining and drying from an aqueous pulp, strong fiber-fiber hydrogen bonding causes fibers to agglomerate, reducing the overall porosity. By forming handsheets using a mixture of sec-butanol and water, inter-fiber bonding is inhibited, allowing fiber separation. Finally, by etching the handsheets with an oxygen plasma, and then performing a plasma-assisted fluoropolymer deposition, superoleophobic properties

are achieved. Handsheets processed in this manner exhibit contact angles greater than 150° for water, ethylene glycol, motor oil and n-hexadecane. While the solvent processing assists in creating the necessary surface structures for superamphiphobicity, it also adversely affects the handsheet strength. Further studies are underway to enhance the paper strength through alteration of the solvent exchange sequence and/or subsequent processing of the handsheet. Development of superamphiphobic paper surfaces will facilitate novel applications where water and oil absorption must be inhibited simultaneously. Furthermore, the techniques, design parameters, and physical insight established in this study are applicable to other fibrous materials with randomized structures, such as nonwovens. That is, the results described in this paper permit control of wetting characteristics for virtually any fiber-based substrate by altering the fiber size and spacing during and after substrate fabrication.

CHAPTER IV

ALTERNATIVE TECHNIQUES FOR OLEOPHOBIC PAPER

4.1 Introduction

While the solvent processing used in Chapter 3 is capable of producing superamphiphobic paper, the solvent exchange method detrimentally effects the strength of the handsheet. The mechanism behind the success of the solvent treatment is the prevention of hydrogen bonding between fibers, thus allowing for increases in the sheet's porosity. Unfortunately, that same hydrogen bonding between fibers is also responsible for the mechanical strength of the sheet. The techniques employed in Chapter 3 modified the properties of the sheet as a whole, increasing porosity throughout the bulk. However, droplets resting in a Cassie-Baxter wetting state only come into contact with the top-most surface. In reality, a droplet in the meta-stable Cassie-Baxter state on paper will penetrate further, but nonetheless, fluids will only interact with the first few fiber layers. Thus, it stands to reason that modifications to only the top fiber layers can still yield increases in the oleophobicity of handsheets. By only altering the top layer of fiber, the strength of the sheet as a whole can be maintained by creating a stronger, denser base sheet that is simply laminated with a a more porous paper.

In this chapter we return our focus to handsheets made from the standard TAPPI procedure T 205 sp-02 (used in Chapter 2 and 3). The profilometer studies from Chapter 3 indicate that the fiber structure of standard water formed handsheets is too densely packed to properly support low surface tension fluids at high contact angles. Instead of modifying the bulk porosity, we focus on modification of only

the surface porosity, which should leave bulk strength unaffected. To achieve this, we remove the solvent processing step that reduces hydrogen bonding and return to studies of water formed sheets. A layering technique is then employed to add multiple surface layers of paper with variable weight loadings and porosity. In this manner, handsheets can be created that maintain their strength while the surface has increased fiber-fiber spacing.

4.2 Methodology

4.2.1 Handsheet Formation

Standard handsheets (HS) are formed from an even weight mixture of hardwood and softwood southern kraft pulp following T 205 sp-02 without any modifications.

The multi-layered handsheets are formed from a single base sheet of standard (1.2 g) basis weight, and then one or more low density sheets are layered on top of the base sheet. The sheets are all made from unrefined southern hardwood kraft pulp (0HW). The formation of the base sheet is performed following TAPPI standard T 205 sp-02, whereby 1.2 g of hardwood pulp is added to a water column and then drained onto a wire mesh. The wet sheet is then removed from the mesh by pressing dry blotter paper on the back and couch rolling. The sheets are then hydraulically pressed onto stainless steel plates and dried overnight. The multilayer sheet were formulated following the TAPPI T 205 sp-02 standard with the following changes: 0.04 g of pulp were used to form the sheet and instead of using blotting paper and a pre-formed standard 1.2 g handsheet was used lieu of blotter paper to remove the low weight layer sheet from the mesh. This is repeated if more than one layer of low density pulp is desired.

4.2.2 Plasma Etching and Fluoropolymer Deposition

Techniques and equipment set up can be found in other chapters of this thesis (2.2.1 and 3.2.2).

4.2.3 Contact Angle Measurements

Static contact angle measurements were performed using a Ramé Hart contact angle goniometer (Model 290, Succasunna, NJ). Static contact angles were measured using 4 μL fluid droplets of n-hexadecane.

4.2.4 Profilometer Measurements

Techniques and equipment set up can be found in other chapters of this thesis (2.2.7 and 3.2.6).

4.3 Results and Discussion

Figure 4.1 shows R_a measurements attained using optical profilometery of a variety of sheet types. There is a slight increase from a standard handsheet (HS) to a handsheet made from unrefined pulp (0HW). When a porous 0.04 g handsheet is layered on top of a 0HW handsheet, the roughness increase is more significant (0HW 0.04). Further addition of a non-porous layer on top of the existing layer has little effect on the roughness (0HW 0.04x2).

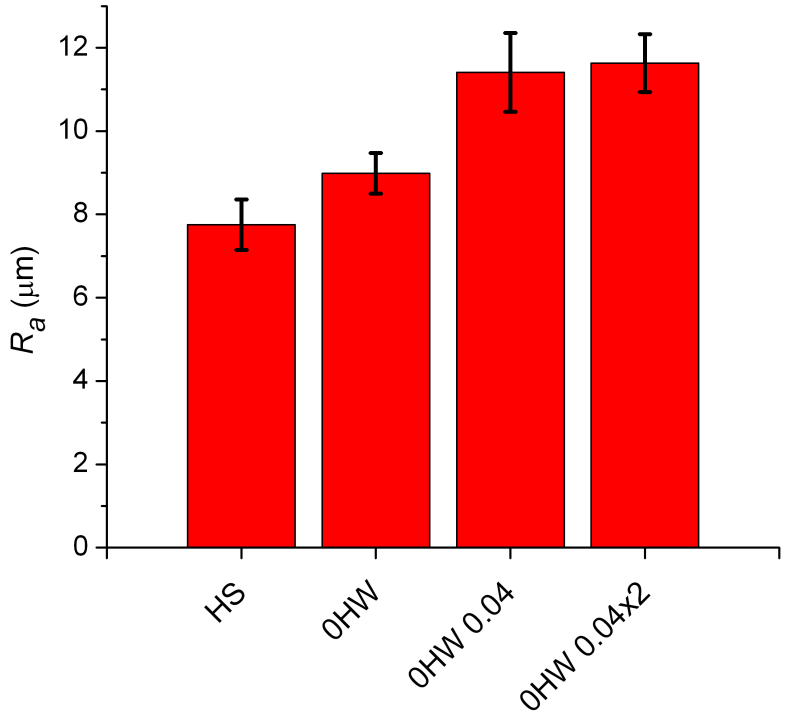

Figure 4.1: Average roughness R_a measurements obtain using optical profilometery of handsheets made from a 50/50 mixture of softwood and hardwood pulp (HS), unrefined hardwood pulp (0HW), unrefined hardwood pulp with 1 (0HW 0.04) and 2 (0HW 0.04x2) layers of porous handsheets made from 0.04 g of 0HW pulp.

Figure 4.2 shows the *n*-hexadecane contact angles of several types of handsheets coated with $\sim$ 450 nm of fluoropoylmer, versus oxygen plasma etch time. Before etching, all handsheets are oleophilic, readily absorbing *n*-hexadecane. After increasing the etch time to 15 minutes, all sheets show an increase in contact angle. Standard handsheets (HS) are still considered oleophilic (contact angle <90°), and 0HW handsheets are marginally oleophobic ($\theta_{n-hexadecane}$= 91.5 $\pm$ 5.2°). The multi-layered sheets experience a more significant increase in contact angle, with both 0HW 0.04 and 0HW 0.04x2 sheet having *n*-hexadecane contact angles of $\sim$100°. At 15 minutes of etching, the contact angles of each sheet type correlates with the initial roughness

values shown in Figure 4.1. The plasma etching is believed to accentuate the already existing fiber structure by creating nanoscale structures on the individual fibers. Continued etching results in minimal contact angle changes for the HS, 0HW 0.04 and 0HW 0.04x2, and causes the 0HW handsheets to become oleophilic again. Chapter 3 discusses likely explanations for this drop off in contact angle, primarily being a function of the fact that 0HW is unrefined and therefore has fewer interfiber connections to resist the plasma etch process. The pulp used to make HS paper samples has been refined to a small degree. However, 0HW 0.04 and 0HW 0.04x2 sheets have not experienced refining for any of the layers. The contact angle differences after 30 minutes of etching between the 0HW and the layered 0HW handsheets is likely the result of the added roughness of the porous layer. In order for a high contact angle to be maintained, the droplet must remain in a Cassie-Baxter state. Fluid contact with a lower layer of fibers would cause a spontaneous transition to the Wenzel state and result in wetting of the fluid. At 30 minutes of etching, the primary structure of tifbers will have begun to degrade. In 0HW handsheets, this results in the collapse of the top layer, reducing the height between the top and subsequent layers and making a Wenzel state transition more likely. The layered handsheets (0HW 0.04 and 0HW 0.04x2) have an increased R_a (Figure 4.1), which not only measures porosity, but pore depth as well. Thus, the layered sheets are capable of withstanding the same surface fiber layer collapse due to the greater distance to the next continuous fiber layer.

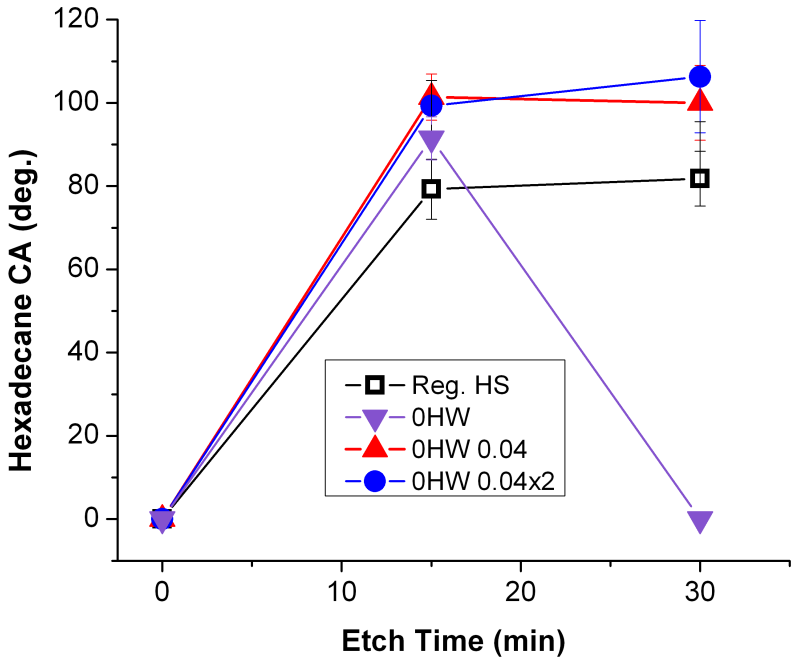

Figure 4.2: n-hexadecane contact angles on handsheets made from a 50/50 mixture of softwood and hardwood pulp (HS), unrefined hardwood pulp (0HW), unrefined hardwood pulp with 1 (0HW 0.04) and 2 (0HW 0.04x2) layers of porous handsheets made from 0.04 g of 0HW pulp etched in the oxygen plasma and then coated with $\sim$ 450 nm of fluoropoylmer.

4.4 Conclusion

While further studies are required to fully understand and exploit the benefits of this multi-layered paper technique, the results are promising. The addition of a single, porous, low density layer of fibers is capable of increasing the oleophobicity of a sheet of paper without detrimentally decreasing the strength. A single low density layer increases the R_a values of the paper, and when combined with 15 minutes oxygen plasma etching and fluoropolymer deposition, yields a $\theta_{n-hexadecane}$= 101.4 $\pm$ 5.5°, a roughly 20° increase over a standard handsheet. A remaining concern is the bonding

strength of the attached layer since it is only bonded two dimensionally the paper's surface. It is likely that this surface layer is more susceptible to delamination or wearing away.

CHAPTER V

DIAMOND-LIKE CARBON COATINGS FOR SUPERHYDROPHOBIC PAPER

5.1 Introduction

Chapters 3 and 4 both focus strongly on the modification of the physical surface structures to modify and increase fluid contact angles. According to the Cassie-Baxter [34] and Wenzel [33] equations, modifications in surface chemistry also play a large role in defining the contact angle. Specifically, low surface energy surfaces are required for superhydrophobic surfaces. The attainment of a low surface energy is traditionally accomplished via the deposition or coating of a hydrophobic polymer, typically fluorine based. However, health and environmental concerns have recently increased reluctance in many industries towards the use of fluorinated polymers. Researchers have therefore created superhydrophobic paper utilizing highly hydrophobic non-fluorinated coating materials, such as waxes and silicon based coatings. [50, 56] However, the range of potential coating materials is narrowed significantly by the desired combination of strong hydrophobicity and fluorine-free chemistry.

Alternatively, it has been demonstrated that even hydrophilic surface coatings with an equilibrium water contact angle (θ_e) of $\sim 75^\circ$ can yield superhydrophobicity when combined with the appropriate surface structures; in particular, approaches have focused on well-defined, repeat structures. [121–123] Ma *et al.* reported on the use of hydrophilic poly(methyl methacrylate) (PMMA) ($\theta_e \sim 68^\circ$) to create superhydrophobic surfaces. [124] However, chemical surface reorientation of the PMMA was required to increase θ_e to $\sim 88^\circ$ before superhydrophobic properties were observed. Even natures most frequently cited superhydrophobic surface, the lotus leaf,

is reportedly coated with a hydrophilic wax ($\theta_e = 74°$). [125] The ability to utilize a hydrophilic coating to create a superhydrophobic surface widens the choice for a multitude of new surface coatings with different chemical functionalities. Specifically, for the paper industry, low cost and recyclability of surface coatings is often critical. Matching these economic criteria with coating performance for hydrophobic barriers becomes increasingly difficult when fluorinated polymers are no longer considered. The economic and environmental feasibility of superhydrophobic paper may be realized at an industrial scale by including hydrophilic polymer coatings to the pool of potential materials. Furthermore, alternative coatings that provide superhydrophobic properties to hydrophilic paper substrates would enable applications that were once infeasible; for example, in the biomedical field, superhydrophobic disposable substrates could be envisioned that have surface coatings functionalized to react with a test fluid for diagnostic purposes.

As a coating material, diamond-like-carbon (DLC) has been studied extensively due to its chemical and physical stability and recyclability. [126, 127] Defined as having a molecular structure with at least 50% sp^3 bonding, DLC has found use as a coating for prosthetics because of its unique combination of favorable properties: biocompatibility, strong wear resistance and high hardness values. [127, 128] From a chemical standpoint, undoped, purely carbonaceous DLC has a relatively high surface energy ($\sim$40 mN/m) and is inherently hydrophilic. Nevertheless, DLC coatings have been utilized to create superhydrophobic surfaces on well-defined, repeating, inorganic, rigid structures that require cleanroom techniques for manufacturing. [78] Other researchers have reported water contact angles >150° by coating cotton with DLC via exposure to a CH_4 plasma, but they were unable to produce similar contact angles on paper; likely due to a lack of surface roughness. [129] While high static contact angles have been achieved and reported, none of the previous studies on DLC or other hydrophilic coatings have demonstrated low hysteresis properties for these

substrates.

In this manuscript we report the fabrication of low hysteresis superhydrophobic DLC-coated paper. A paper substrate is distinctly different from many of the previously studied surfaces, which all have structural features with sizes and spacings that are well defined by the processing steps. In contrast, paper consists of heterogeneously-sized fibers that are randomly oriented and spaced as a result of the papermaking process. Plasma deposition of DLC onto paper from an acetylene (C_2H_2) precursor induces hydrophobicity, but the resultant surface displays high hysteresis. Therefore an oxygen plasma etch is utilized to create additional nanoscale structures on each fiber; at relatively short times the etch process results in an increase in nanoscale structure and the advancing contact angle, but the paper remains a high hysteresis surface. By further increasing the etch time the microscale roughness is increased, creating a hierarchical structured surface that when coated with a hydrophilic DLC film, exhibits wetting properties similar to those of fluoropolymer-coated surfaces.

5.2 Experimental

5.2.1 Plasma Processing

Paper samples were created in house according to the TAPPI standardized method T205 sp-02 using an equal weight ratio of southern softwood kraft and southern hardwood kraft pulp. Paper samples were fabricated in this manner to eliminate the effects of additives and fillers that are commonly used in the industry for commercial substrates. After fabrication, paper samples were etched in an eight inch stainless steel parallel plate vacuum rf plasma system (Kurt J. Lesker Co., Jefferson Hills, PA). The sample stage is 2.5 inches in diameter and was heated to 110°C for all experiments using Omegalux CSH-102100 cartridge heaters (Omega Engineering Inc., Stamford, CT). The rf power was provided at a frequency of 13.56 MHz. Prior to either the

etching or deposition step, the system was brought to a base pressure of $2.5\text{x}10^{-2}$ torr. Oxygen plasma etching was conducted at an oxygen flow rate of 20 standard cubic centimeters per minute (SCCM) and a pressure of 0.5 torr. DLC deposition was performed using a mixture of acetylene (C_2H_2) and argon at a 10 SCCM : 30 SCCM flow ratio and 0.5 torr pressure. A deposition time of 2 minutes yielded a coating layer $\sim$ 80 nm in thickness (determined by ellipsometry from a DLC film deposited onto a silicon wafer). For control experiments, fluoropolymer deposition was conducted using a pentafluoroethane (PFE) (Praxair) precursor at 20 SCCM and Ar at 75 SCCM, with a reactor pressure of 1.0 torr. Further descriptions regarding the deposition process and reactor configuration have been published previously. [18] All flow rates were controlled via MKS Instruments (Wilmington, MA) type 1179A flow controllers.

5.2.2 Contact Angle Measurements

Contact angles were measured on a Rame-Hart contact angle goniometer (Model 290, Succasunna, NJ). Static contact angles were measured using 4 μL water droplets. Advancing contact angles were obtained by initially placing a 4 μL droplet on the surface and increasing the volume by 0.5 μL increments until a final volume of 10 μL was obtained. Receding contact angles were measured by decreasing the volume of a 10 μL droplet by 1 μL increments until a final volume of 4 μL was obtained.

5.2.3 Physical Characterization

Atomic force microscopy (AFM) measurements were collected with a Veeco Dimension 3100 Scanning Probe Microscope on paper prior to DLC coating. Standard AFM probes (Micromasch, Ladys Island, SC) with spring constants of 40 N/m and tip radius of $\sim$ 8 nm were utilized in tapping mode. Average roughness (R_a) values reported here represent an average over four 5 x 5 μm area scans. Optical profilometry was performed using a Wyko NT3300 Profilometer. Measurements were analyzed

using the Vison32 software (Veeco Instruments Inc.); the Ra values calculated from profilometry measurements represent an average over four 1.2 x 0.9 mm scans. Scanning Electron Microscopy (SEM) of unmodified and plasma modified paper surfaces was performed using a Zeiss Ultra60 FE-SEM at an electron energy of 5.0 keV. All samples were sputter coated with Ag/Pd prior to imaging.

5.2.4 Chemical Characterization

X-ray Photoelectron Spectroscopy (XPS) analyses were conducted using a Thermo Fisher Scientific K-Alpha XPS with a 400 m micro-focused monochromatic Al K X-ray source. Attenuated Total Reflectance Fourier Transform Infrared Spectroscopy (ATR-FTIR) measurements were performed with a Bruker Hyperion 1000 spectrometer.

5.3 Results and Discussion

Variations in chemical properties and sp^2/sp^3 bonding ratios have previously been shown to affect the equilibrium contact angle of DLC surfaces. [127] To determine the chemical structure of our plasma deposited surfaces, characterizations were performed with Attenuated Total Reflectance Fourier Transform Infrared Spectroscopy (ATR-FTIR) and X-Ray Photoelectron Spectroscopy (XPS) (Supporting Information). The ATR-FTIR spectra (Figure 5.1) show dominant sp^3 bonding. Peak assignments can be found in Table 5.1. XPS spectra in Figure 5.2 indicate a carbonaceous surface with oxygen surface contamination (96% C and 4% O).

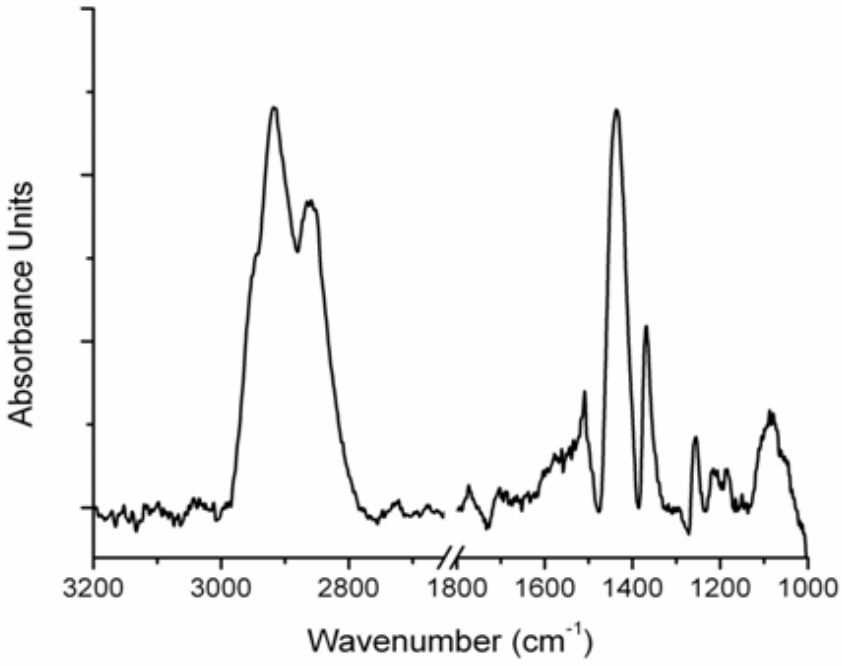

Figure 5.1: ATR-FTIR Spectra of DLC deposited on a silicon wafers.

Table 5.1: Wave number assignments for the spectra show in Figure 5.1.

Wavenumber	**Configuration**
(cm-1)	
2955	sp^3 CH_3 asym
2920	sp^3 CH_2 asym
2860	sp^3 CH_2 sym
1580	sp^2 aromatic
1515	sp^2/sp^3 C-C
1437	sp^2 CH aromatic
1370	sp^3 CH_3 sym

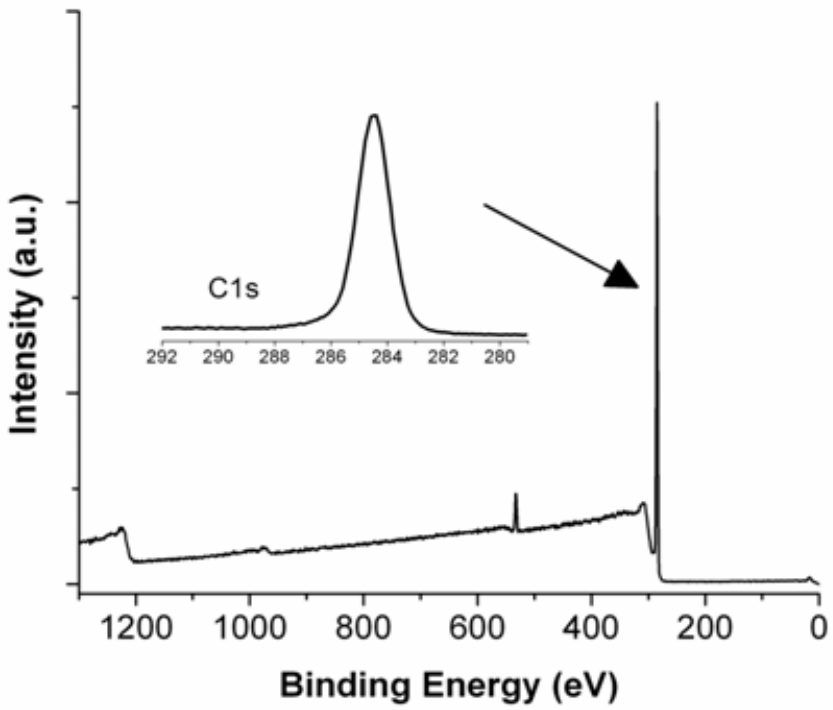

Figure 5.2: XPS spectra of DLC coated onto silicon. Inset depicts the C1s high resolution scan.

The equilibrium contact angle (θ_e) of DLC-deposited on a flat silicon wafer was 68.2 $\pm$ 1.5°; by definition, this is considered a hydrophilic surface (Figure 5.3a). To our knowledge, this is the lowest equilibrium contact angle that has been used to create a superhydrophobic surface. Nevertheless, deposition of ~80 nm (R_a = 1.79 $\pm$ 0.38 nm) of DLC onto paper provides an increase in the static contact angle, from 0°(untreated paper readily absorbs water) to 118.6 $\pm$ 4.6°. In order to further increase the contact angle, roughness must be added in combination with the surface coating. Figure 5.4 and Figure 5.5 present the static and advancing and receding contact angles, respectively, of paper samples that were etched in an oxygen plasma for varying times and then coated with DLC. The increase in θ_A from θ_e when DLC is coated onto unetched paper is due to the inherent roughness of the paper surface from the fiber

structure. However, the unetched DLC-coated paper displays extremely high contact angle hysteresis, with advancing and receding contact angles of $124.3 \pm 4.1°$and $<10°$, respectively. As a consequence, the non-wetting water droplets strongly adhere to the substrate. Previously, our group has shown that the addition of nanoscale roughness to cellulose fiber networks that already provide an inherent micrometer-scale roughness, can both decrease the contact angle hysteresis and increase the static contact angle. [18] For the current study, we again used an oxygen plasma etch process to generate nanoscale roughness on the cellulose fibers; as a result, the advancing water contact angle increased to values above 150°after only 5 minutes. Further etching did not affect the advancing contact significantly, but yielded a steady increase in the receding contact angle (Figure 5.5). After 60 minutes of plasma etching, a low-hysteresis superhydrophobic surface was created ($\theta_A = 162.0 \pm 6.3°$; hysteresis $8.7 \pm 1.9°$); Figure 5.3b shows an image of a water droplet on that substrate.

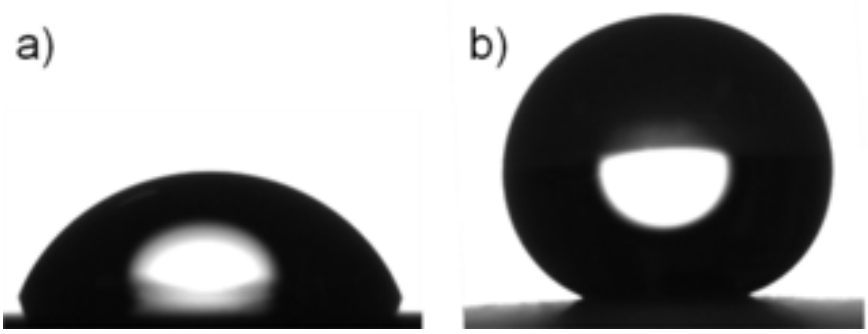

Figure 5.3: Water droplets on a) silicon wafer with DLC coating ($\theta = 68.2°$), and b) paper handsheet that was etched for 60 min and coated with DLC ($\theta = 162.0°$).

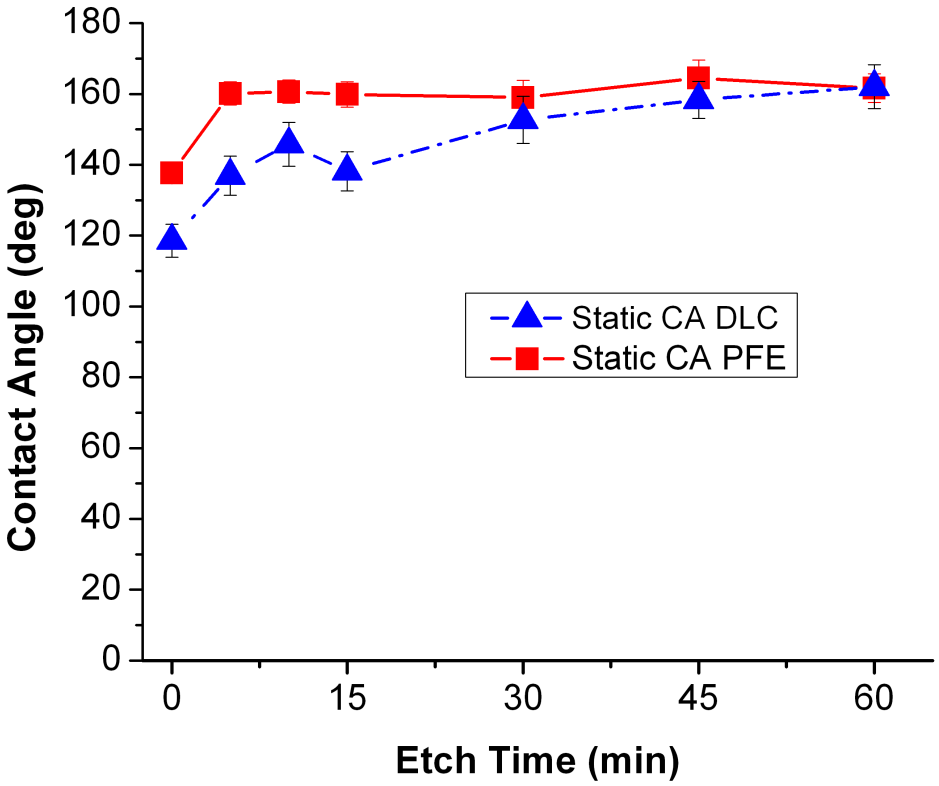

Figure 5.4: Static contact angles of paper substrates coated with DLC (blue triangles) and PFE (red squares) films as a function of plasma etch time.

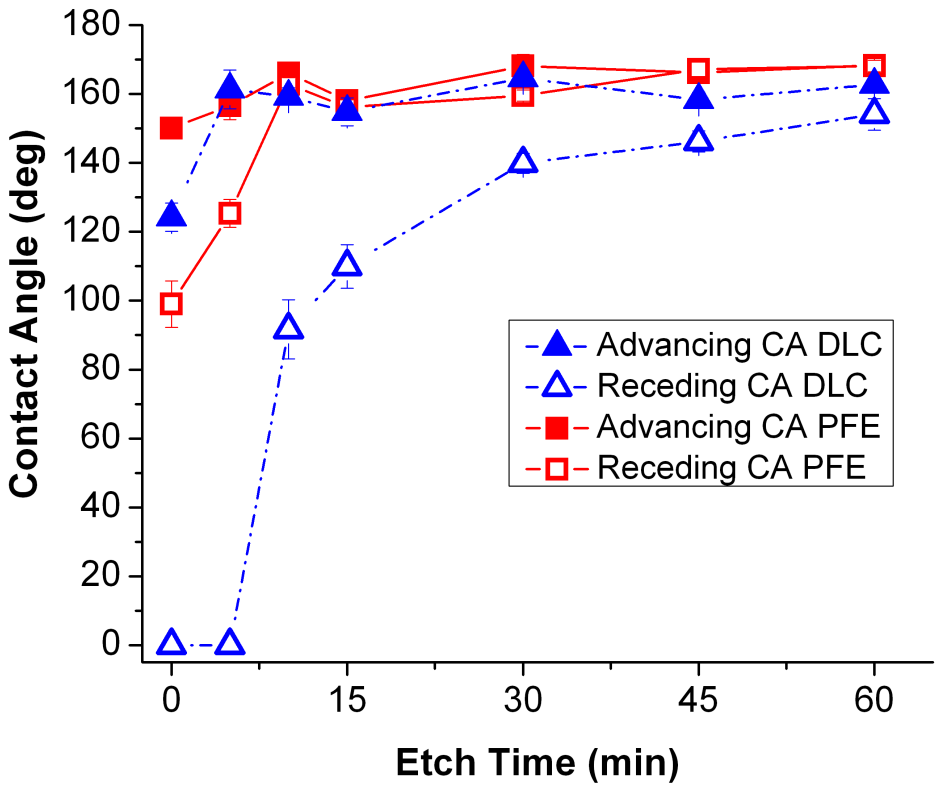

Figure 5.5: Advancing (solid) and receding (hollow) contact angle data for DLC (triangles) and PFE (squares) coated paper samples as a function of etch time in oxygen plasma.

For comparison, Figures 5.4 and 5.5 also present contact angle values of a fluorinated polymer coating that was plasma-deposited from a pentafluoroethane (PFE) precursor. This fluorinated surface has been previously studied in our group and has a θ_e of $\sim$105°on a silicon wafer and a contact angle of $\sim$140°when deposited on unetched paper. [18] The static contact angles for the two surfaces are similar in value for all etch times, with a difference of approximately 20°for the unetched sample, decreasing to insignificant differences after 30 minutes of plasma etching. A more rapid convergence is observed for the advancing contact angle, where only 5 minutes

of etching is needed to achieve equivalent advancing contact angles for DLC- and PFE-coated paper. However, the difference between the receding contact angles is much greater, with the DLC-coated surface displaying similar contact angles to those measured on PFE-coated surfaces only after 60 minutes of etching.

To understand the evolution of the contact angle with increasing etch time and gain insight into differences between the DLC- and PFE-coated surfaces, it is helpful to examine the Cassie-Baxter model [34] (Equation 5.3), which is often used to describe wetting properties of low hysteresis superhydrophobic surfaces. Droplets in the Cassie-Baxter wetting state are assumed to contact both the solid surface as well as air pockets entrapped among the rough surface structures.

$$cos\theta_A = fcos\theta_e - (1 - f) \tag{5.1}$$

In Equation 5.3, θ_A represents the apparent, measured contact angle, θ_e is the equilibrium contact angle and f is the fraction of the droplet that is in direct contact with the solid surface. By increasing the roughness of a surface, the contact area of the droplet in contact with the solid is reduced. Under certain conditions, this can lead to an increase in the apparent contact angle relative to the equilibrium contact angle, even if θ_e <90°. For example, using $\theta_e = 68$ for the DLC surface and inserting the desired θ_A of 150°, an f value of 0.09 can be calculated, indicating that a high level of roughness is necessary to yield superhydrophobic properties. In contrast, for PFE, an f value of 0.18 is required.

Figure 5.6 shows SEM images of paper fibers that were etched in the oxygen plasma. An increase in nanoscale roughness is clearly observed between an unetched fiber (Figure 5.6a) and fibers that have been exposed to the oxygen plasma for various lengths of time (b) 15 min, c) 30 min and d) 60 min). The SEM images also demonstrate that beyond 15 minutes of etching the surface structures show little additional roughness evolution. This observation is in supported by average roughness

(R_a) values obtained though AFM analyses, which are presented in Figure 5.7. A sharp increase in roughness is observed during the initial stages of etching, while after 5 minutes of etching, there is no statistically significant further increase in R_a. The increase in nano-scale roughness is responsible for the initial rapid increase of the advancing contact angle of DLC-coated paper observed in Figure 5.5. The stagnant nature of the roughness after 5 minutes is likely due to the fact that the plasma etch process removes the various surface features at the same rate, thus exposing layers deeper within the fiber, but maintaining the same roughness level. Furthermore, the consistent roughness after 5 minutes correlates well with the advancing contact angles of DLC in Figure 5.5. It must also be noted that there are rather large uncertainties in the Ra measurements via AFM. This is due to a combination of effects: paper inherently has submicron scale wrinkles when dried (Figure5.6a), and the plasma etch process affects each fiber differently depending on the exact physical structure of the area sampled (amorphous to crystalline ratio) and the specific orientation of the fiber in relation to the plasma. Despite the error, both SEM images and average R_a values from AFM experiments indicate that extended etching does not significantly increase the nanoscale roughness of the fibers.

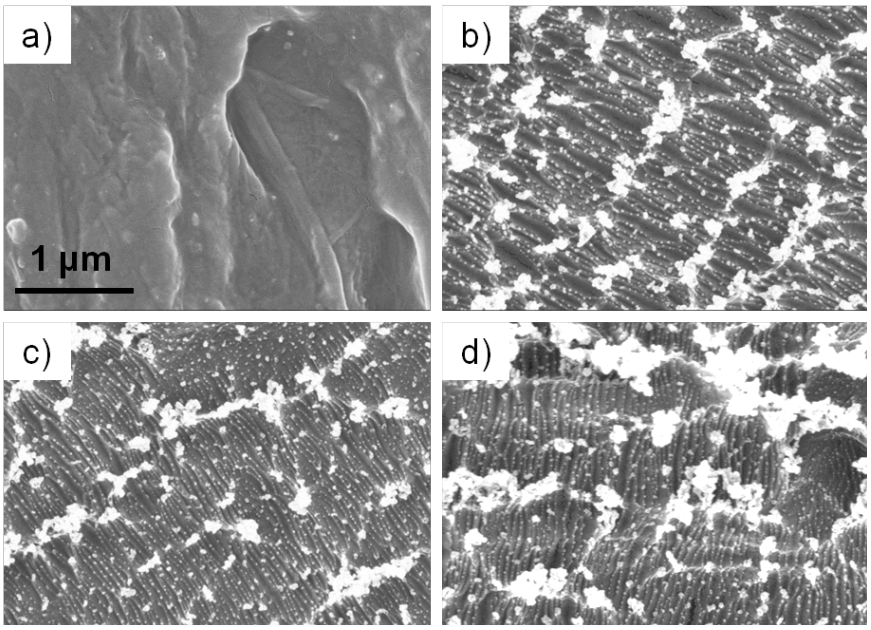

Figure 5.6: High magnification SEM images of a) an unetched paper fiber, and fibers that have been plasma etched for b) 15 min, c) 30 min and d) 60 min.

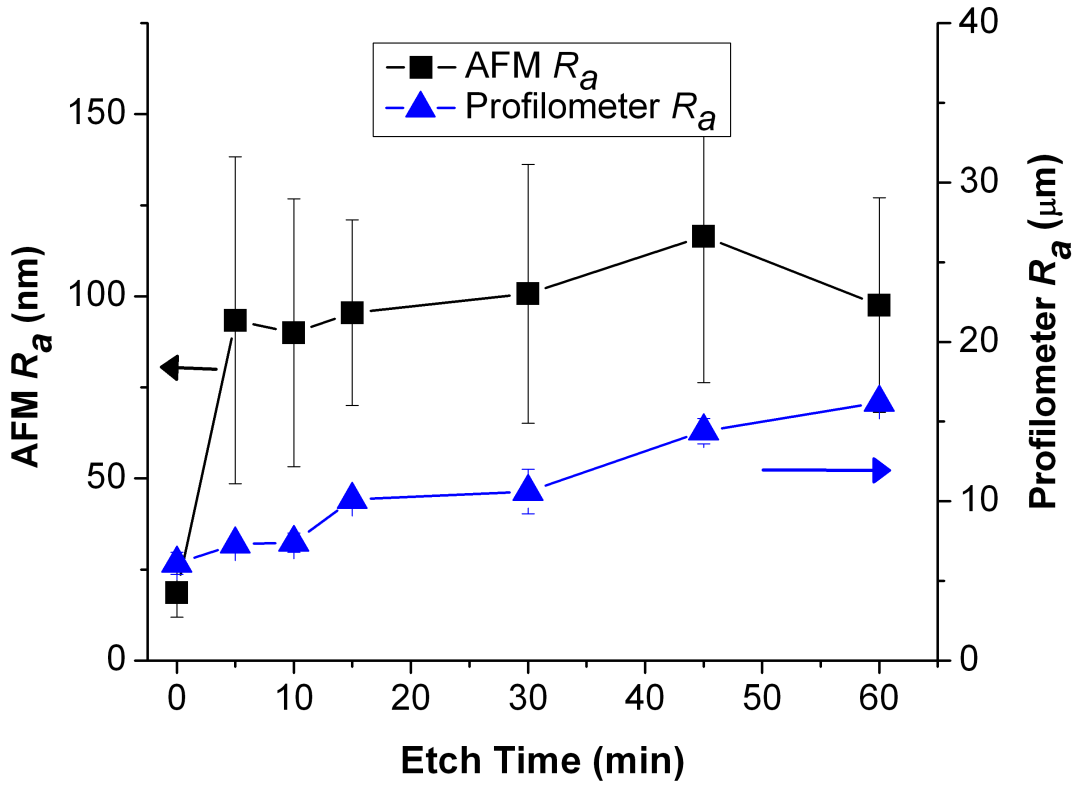

Figure 5.7: Average roughness (R_a) measurements collected with AFM (squares; left axis) and optical profilometry (triangles; right axis) for paper substrates as a function of etch time.

While nanoscale differences are not observed for the longer etch times, a change in the microscale structure can clearly be seen. Figure 5.8 shows lower magnification images of paper substrates that were etched for the same times as in Figure 5.5. The SEM images in Figure 5.8 show the formation of smaller diameter fibers as the etch time is increased. Measurements from optical profilometry, which quantifies roughness on a much larger lengthscale than does AFM, are also presented in Figure 5.7 (right axis). The increase in the proportion of smaller diameter fibers, and thus Ra at the microscale, is a result of the oxygen plasma etch process. Continual removal of the

amorphous phase of the cellulose fibers during plasma etching deteriorates the fibers, eventually resulting in a structure where only the crystalline framework of the original fibers remains. Because the formation of microscale structures requires the removal of a significant amount of material, the R_a values measured via profilometry increase at a much slower rate when compared to those of the nanoscale structure obtained through AFM. A nearly linear increase is observed from $R_a = 6.1 \pm 0.7$ μm (0 min etch) to 16.2 ± 0.3 μm (60 min etch). This slow increase in micron scale roughness correlates with the receding contact angle measurements of DLC-coated paper shown in Figure 5.5.

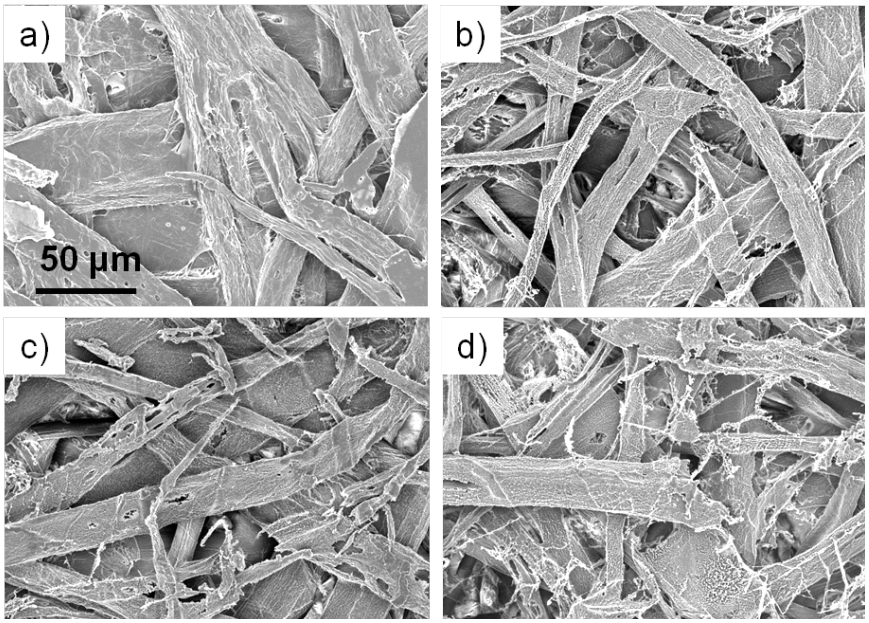

Figure 5.8: Low magnification SEM images of a) unetched paper and paper that has been plasma etched for b) 15 min, c) 30 min and d) 60 min.

Comparing Figure 5.7 to the contact angles in Figure 5.5, it is apparent that a certain level of dual scale roughness is necessary to yield low hysteresis superhydrophobic behavior from a hydrophilic surface coating. The sharp increase in advancing contact angle after 5 minutes of etching corresponds to the formation of nanoscale roughness,

while the slower rise of the receding contact angle correlates with the gradually increasing microscale roughness. It is also apparent that with the use of a hydrophobic fluorinated surface (PFE), decreased roughness values can be invoked so that only a marginal increase in microscale structure is sufficient to obtain a low hysteresis superhydrophobic surface. These experimental observations correlate well with predictions from the basic Cassie-Baxter model (Equation), where a lowered θ_e requires that a smaller percentage of the fluid be in contact with the solid, i.e. higher roughness: DLC coatings require more roughness than the inherently hydrophobic PFE to achieve superhydrophobicity.

The surface of plasma-treated paper differs from many of the previous studies that have used hydrophilic coatings to create superhydrophobic surfaces. The lack of hierarchical structure is likely the reason behind the inability of previous investigations to attain low hysteresis properties. Much like the lotus leaf, whose surface is composed of microscale bumps that are covered with nanoscale hairs of wax, the etched paper used in this work also has hierarchical surface structures in the form of nanoscale structures on the fibers combined with the microscale roughness of the fiber network itself. Moreover, paper substrates are distinct from the well-defined, rigid, inorganic structures used by other authors in that the surface structure is a heterogenous and randomized network of flexible fibers.

5.4 Conclusions

We have demonstrated the ability to create low hysteresis superhydrophobic paper surfaces by applying a thin hydrophilic DLC surface coating. We accomplished this by first using an oxygen plasma etch to selectively remove the amorphous phase of cellulose and thus create nanoscale surface structures on each fiber. However, this level of structure is only sufficient to increase the advancing contact angle, leaving the receding contact angle unaffected and thus leading to strong adhesion of water

droplets. Continued plasma etching of the paper substrates modifies the microscale structure as well, partially etching away the larger fibers to create smaller diameter fibrils, thus enhancing the microscale roughness. After 60 minutes of etching, a hierarchical structure is created, which after deposition of DLC, yields low hysteresis superhydrophobic properties that are similar to paper substrates coated with fluoropolymer layers. To our knowledge this is the most hydrophilic (lowest θ_e) surface to date to exhibit such wetting properties.

CHAPTER VI

SUPERHYDROPHOBIC STAINLESS STEEL

Reproduced from L.Li, V. Breedveld and D.W. Hess, *ACS Applied Materials & Interfaces*, 2013, 4(9) pp. 4549-4556

6.1 Introduction

The same fundamental design parameters of surface roughness and low surface energy that were utilized to create superhydrophobic paper surfaces can also be applied to other materials. Specifically, we investigate the creation of superhydrophobic stainless steel through the etching of the surface combined with a subsequent fluoropolymer deposition. Superhydrophobic metals are of great interest for industrial applications due to their special wetting properties, such as self-cleaning [12,35], drag reduction [130–132] and corrosion resistance [106, 133]; these features generally require that the high static contact angle is combined with low droplet adhesion (as defined by a low contact angle hysteresis). [35, 133, 134] Copper, aluminum, titanium and numerous metallic alloys have been surface modified to attain superhydrophobic properties. [25, 134] In order to ensure that these metals display superhydrophobic properties, surface roughness at the proper length scale and a low surface energy are required. Techniques used for the creation of surface roughness on metals include electroless deposition [135], sol-gel methods [26] and anodization. [136] Fluorinated molecules are commonly used to achieve the necessary low surface energy. Since the discovery in 1905 that iron alloyed with chromium is resistant to acid attack, stainless steel (SS) has been employed for applications in a wide range of fields, including petrochemical, construction, maritime and aviation industries. [137, 138] Its broad use is the result of a unique and useful combination of high corrosion resistance and

excellent mechanical strength. Industries where metal-fluid contact is common would benefit greatly from superhydrophobic stainless steel surfaces. For example the food industry frequently uses SS vessels to store and mix fluids. The anti-fouling and corrosion resistant properties afforded by superhydrophobic surfaces will reduce the need for cleaning, and thus reduce equipment/process down-time. The low hysteresis properties attained in our studies will also allow complete dewetting of tanks and pipes, thereby reducing loss of product due to residual surface wetting and adhesion. Furthermore, low hysteresis superhydrophobic surfaces have been demonstrated to reduce fluid drag in pipe flow. [130] Despite this wide range of potential applications, fabrication of superhydrophobic stainless steel has been relatively unstudied when compared to the other metals listed above. The majority of published work either uses ablation with a femtosecond laser to create the appropriate surface roughness [136, 139, 140], which is not an easily scalable process, or coats the SS with another material to add roughness, [26, 76, 141, 142] a process that often lacks mechanical durability.

To find a more scalable process to create robust SS surfaces with superhydrophobic properties, we exploit the fact that surfaces of solid materials are often heterogeneous with regards to chemical composition and/or structure. If the heterogeneity occurs at suitable length scales, and if a selective etching method can be found, it is then possible to create surface roughness. Using this paradigm, our group has produced low hysteresis superhydrophobic paper substrates: selective etching of the amorphous phase of cellulose in an oxygen plasma, while leaving the crystalline phase, creates surface roughness at the required length scale. [18] The same approach has been applied to other polymer surfaces. [143] The key advantage of generating roughness directly on a material, as opposed to adding it through deposition of particles or residues, is the inherent mechanical stability of the structures that are formed via etching. Other researchers have used selective etching with an etchant mixture of ferric trichloride, hydrochloric acid and phosphoric acid to attack the less stable crystalline dislocation

defects that exist in 304 SS; subsequent coating of the surface with a fluorosilane led to superhydrophobic properties. [144] Although their work demonstrated that etching with ferric chloride can generate superhydrophobic surfaces on 304 SS, no characterization of the chemical and physical effects of the etch process on superhydrophobic properties was presented. Furthermore, the dependence of surface properties on etch parameters was not reported, nor were other SS alloys studied. In order to tailor and control SS wetting properties for specific applications and to ensure that the surface inhibits corrosion, it is necessary to relate the etch process to SS surface structure, chemical composition, and wetting characteristics in more detail.

Stainless steel is a broad term used to describe iron-based metals that contain greater than 12% chromium and have resistance to corrosive environments. SS alloyed compositions vary greatly based upon the desired application, with different alloy mixtures imparting varying corrosion resistance, hardness and mechanical strength. Iron-chromium-nickel alloys are known as the 300 series of SS, and are the most commonly used. 304 SS is composed of 18 wt.% chromium and 8 wt.% nickel, with iron making up the majority of the remaining composition. 316 SS has a similar composition, with the primary difference being the addition of 2-3 wt.% molybdenum.

In this manuscript we present a simple method to fabricate superhydrophobic stainless steel surfaces by invoking hydrofluoric (HF) acid etching. Instead of the deposition of a secondary material to establish roughness, chemical etching is used to create surface roughness that maintains the mechanical and corrosive properties of the SS. Although HF acid is known to attack stainless steels, characterization of the surfaces formed by the concentrated acid etch has not been reported. The ability of this method to create roughness on two commonly used SS alloys, 304 and 316, is demonstrated. Alloy composition differences between these two grades of SS cause varied etch rates and surface structures, leading to different wetting properties. Our

current study focuses both on the superhydrophobic properties that our process generates and on the chemical changes needed to initially create the appropriate roughness. The etching process selectively attacks grain boundaries through intergranular corrosion and thus leads to the formation of micron and submicron scale roughness. On 316 SS we demonstrate the enrichment of molybdenum on the surface grains after HF etching. By passivating the etched samples in nitric acid, the advantageous corrosion resistant properties of SS are re-established. Despite the fact that the effect of chemical passivation on stainless steels has been studied previously, the combination of passivation with a HF acid etch to form the appropriate surface roughness to create superhydrophobic stainless steels has not been explored to date. Specifically, the passivation step causes separation of the martensitic-austenitic phase boundaries on 304 SS samples, creating a multiscale roughness that greatly differs from the roughness created in the etch step. Subsequent plasma deposition of a covalently bonded fluoropolymer layer then yields high water contact angles and low hysteresis on both SS grades.

6.2 Experimental Methodology

6.2.1 Etching and Passivation

304 SS samples were obtained from Trinity Brand Industries and 316 SS samples were obtained from Maudlin Products, both in the form of 8 x 12 x 0.02 in shim sheets. Etching was performed at 25°C and 50°C using a 48-51% hydrofluoric acid solution (ARISTAR, ACS Grade). Unpassivated samples were rinsed with de-ionized (DI) water immediately after removal from the HF acid etch bath. The passivated samples, immediately after removal from the HF acid etch bath, were placed in a DI water bath, rinsed with DI water, and placed in a 50% nitric acid (ARISTAR, ACS Grade, 68-70%) bath at 50°C for 30 minutes, following the procedure described by ASTM standard A380-06. After completion of passivation, samples were again rinsed

with DI water.

6.2.2 Hydrophobic Film Deposition

After the final DI water rinse, both unpassivated and passivated samples were placed in a parallel plate RF (13.56 MHz) plasma reactor, where deposition of fluoropolymer was carried out at 110°C and 120W using a mixture of pentafluoroethane precursor (Praxair) at 20 SCCM and argon at 75 SCCM. The thickness of the fluoropolymer layer is 100 nm, which yields complete coverage of the surface. Detailed reactor configuration and experimental deposition parameters have been described previously.31 The result of the deposition is a highly crosslinked fluoropolymer layer that is covalently bonded to the SS surface.

6.2.3 Contact Angle Measurements

Static and dynamic contact angles were measured on a Rame-Hart contact angle goniometer (Model 100, Netcong, NJ). Static contact angles were measured by placing 4 μL droplets of DI water onto the substrate. Advancing contact angle measurements were performed starting with a 4 μL droplet and increasing the droplet volume by 1 μL increments until the droplet volume was 10 μL. Receding contact angle measurements were then performed by decreasing the volume of the 10 μL droplet in 0.5 μL steps until reaching the initial volume of 4 μL.

6.2.4 Profilometer Measurements

Average roughness (R_a) was measured using a Wyko NT2000 Optical Profilometer. Measurements were analyzed using the Vison32 (Veeco Instruments Inc.) analysis software. The average roughness was calculated per the ANSI B46.1 standard.

6.2.5 Surface Analyses

X-ray Photoelectron Spectroscopy (XPS) analyses were conducted using a Thermo Electron Corporation K-Alpha XPS system employing a micro-focused monochromatic Al K X-ray source, with a 400 μm spot size. Samples were prepared for XPS by heating in a vacuum oven at 150°C overnight. Scanning Electron Microscopy (SEM) images were taken with a Zeiss Ultra60 FE-SEM at an electron energy of 10.0 keV. Energy Dispersive X-ray Spectroscopy (EDX) was performed using an integrated INCA EDX detector (Oxford Instruments) at an electron energy of 15keV.

6.3 Results and Discussion

For the sake of clarity, samples treated with the HF etch, passivation and fluoropolymer coating steps will be denoted by (E), (P) and (F), respectively. For example, a sample designated 304(EF) SS has been etched and coated with a fluoropolymer, but not received the passivation treatment.

6.3.1 Hydrofluoric Acid Etching

In order to fully characterize and understand the superhydrophobic surfaces generated by our process, the means by which surface roughness is created must first be examined. The mechanisms of the etch and passivation steps define the size, distribution, roughness and stability of the structures. Therefore, prior to presenting contact angle measurement data, we discuss in detail the chemical and physical effects of the etching and passivation steps on the stainless steels. Hydrofluoric (HF) acid is commonly used for the pickling of stainless steel; in this process, a mixture of nitric and HF acids is used to remove surface contamination. The cleaning process occurs through competing HF etching and nitric acid passivation reactions, which continue until the surface has been cleaned. In contrast, when SS samples are etched in a corrosive environment without an oxidizer, as in our HF acid etch, the chemical reaction

continues without hindrance, eventually leading to a roughened surface. During the HF acid etch process, SS samples change from their well-known, shiny silver appearance to black due to the added surface roughness and changes in chemical surface composition. Simultaneously, the HF acid solution turns green, a color that is characteristic of iron and chromium fluorides. XPS analyses of the surface composition of 304(E) and 316(E) SS after varied etch times are presented in Figures 6.1 and 6.2. In both cases, decreases in oxygen and iron atomic percentages are observed with longer etch times, while the fluorine concentration increases, indicating the formation of metallic fluorides. The deviation observed in Ni concentration in both samples is within the measurement variability of $\pm$ 1.5 atomic % for all sample sets.

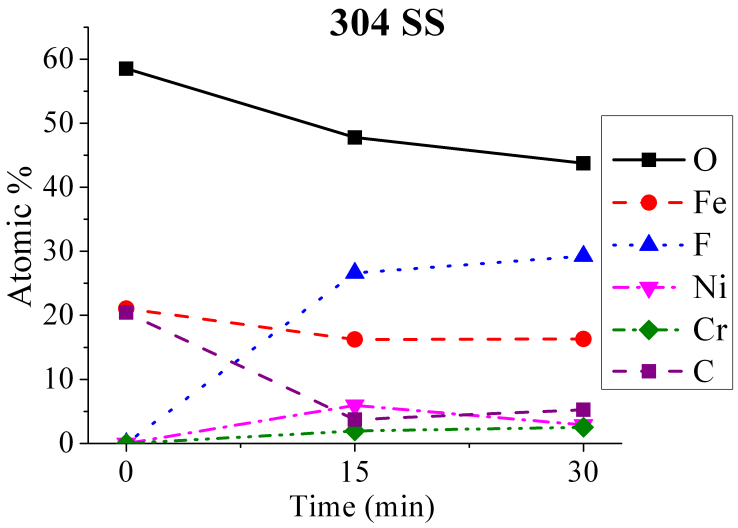

Figure 6.1: XPS analysis of 304(E) SS after 0, 15 and 30 minutes of etching at 50°C.

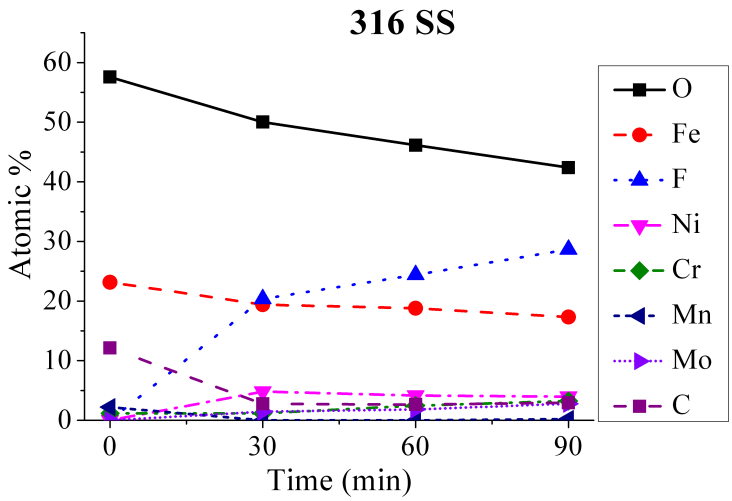

Figure 6.2: XPS analysis of 316(E) SS after 0, 30, 60 and 90 minutes of etching at 50°C.

Figure 6.3 presents XPS spectral scans for chromium and iron on 304(E) SS after various HF etch times at 50°C. Before etching, elemental chromium (574.0 eV) and iron (707.2 eV) are present on the surface along with Cr_2O_3 (577.1 eV) and Fe_2O_3 (710.9 eV). With an increase in etch time, the elemental metal peaks disappear, which corresponds to their conversion to oxides and fluorides. Close inspection of the XPS spectra reveals the development of shoulders at higher binding energies with increased etch time for both Cr and Fe. Deconvolution of the spectra indicates that these shoulders correspond to the formation of CrF_3 and FeF_3 at 579.1 and 714.2 eV, respectively. The Gaussian-Lorentzian deconvolution curves for the samples etched for 30 min are shown in Figure 6.3. Previous studies that described the etching of 304 SS in 40% HF at 40°C have reported similar XPS results. [145]

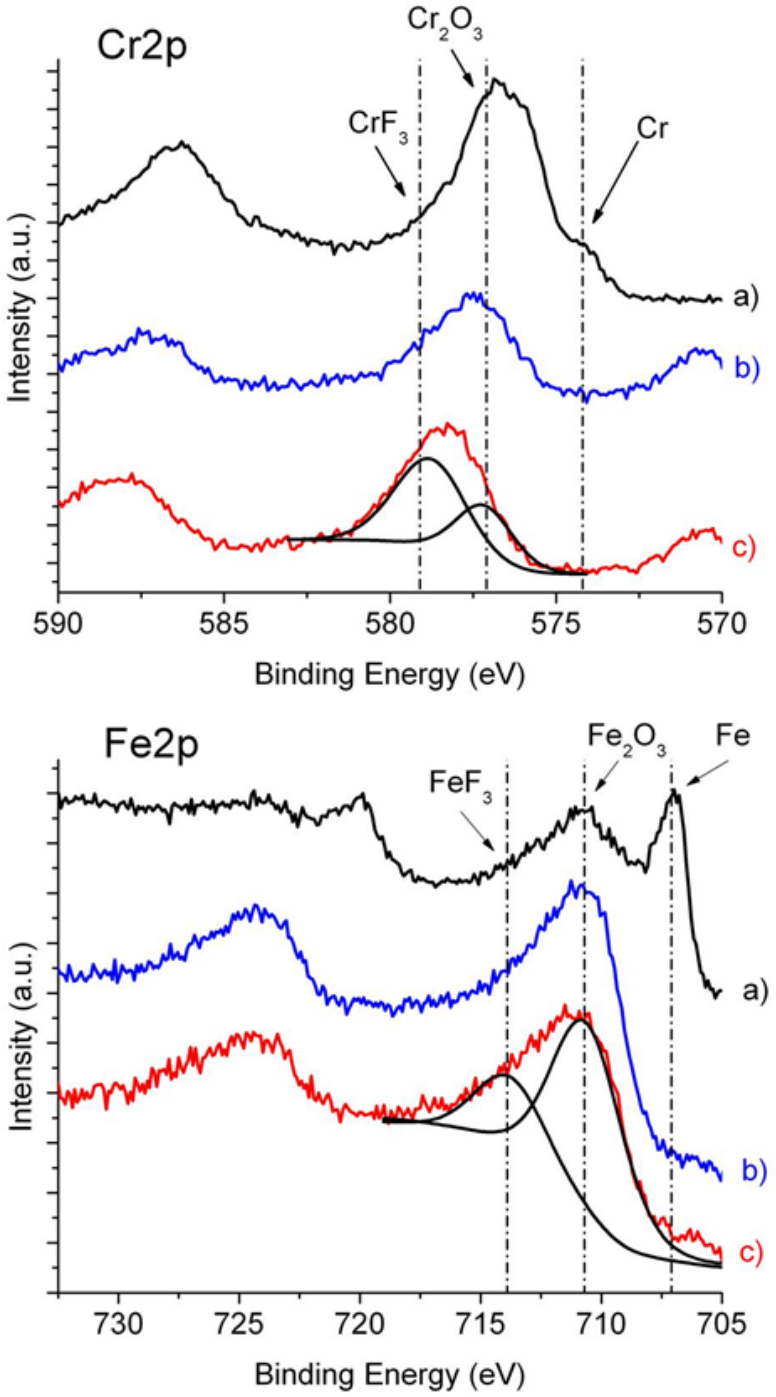

Figure 6.3: XPS scans of Cr2p and Fe2p on 304(E) SS: a) before etching, and after b) 15 minutes, and c) 30 minutes of etching. Peaks in the 585-590 eV and 720-725 eV range correspond to the $2p_{1/2}$ peaks of Cr and Fe, respectively.

Through the redeposition of metallic fluorides and oxides, roughness is created at micron and submicron lengths. Figure 6.4a presents an image of petal-like structures on 304(E) SS etched for 5 minutes in HF acid at 50°C; these structures, which are reminiscent of fractal geometries, have been shown to be characteristic of iron oxide. [146] Similar structures are also, to a lesser extent, present on etched 316(E) SS samples, with formation mainly occurring between grains. The effects of fractal structures on the superhydrophobic surface properties have been previously modeled and observed. [58,147] Although further studies are needed to characterize the fractal nature of our samples and determine the specific role that such structures play in the superhydrophobicity, these studies are beyond the scope of the current investigation. Iron fluoride, chromium fluoride and chromium oxide have been reported to have granular crystalline structures, similar to those shown in Figure 6.4b. [148,149] The precipitation of both FeF_3 and CrF_3 from acidic baths has been demonstrated previously for the case of SS pickling. Specifically, if a pickling bath is not continuously replenished, precipitation of metal fluorides can occur [150], with FeF_3 being of greater concern due to the high concentration of iron in SS. No intentional solution agitation was used during our etch process, which allowed concentration gradients to form near the surface of the stainless steel during the reaction with HF. When the solution becomes locally supersaturated, fluorides and oxides can precipitate to form the observed surface roughness.

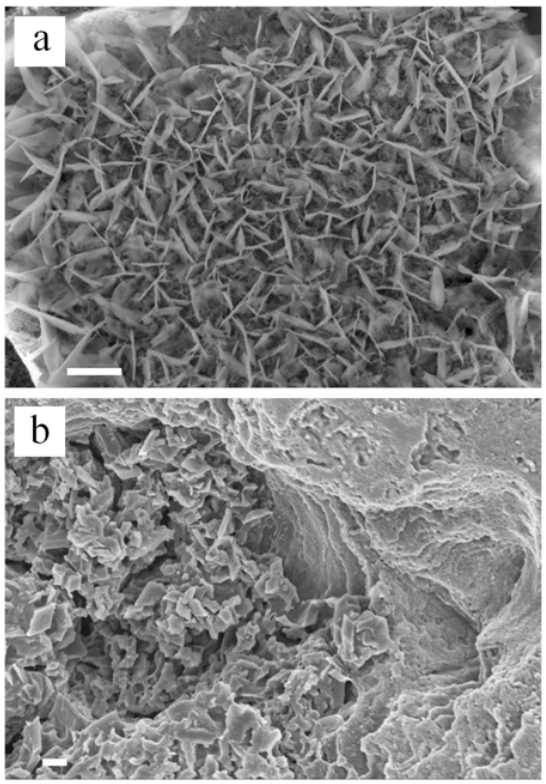

Figure 6.4: 304(E) SS etched for 5 min at 50°C with: a) petal like structures that are indicative of Fe_2O_3, b) granular structures of FeF_3 and CrF_3. White scale bars correspond to 1 μm.

While the aforementioned structures form rapidly on 304 SS, their evolution occurs at a much slower rate on 316 SS. The predominant difference between the two grades of SS is the presence of molybdenum in 316 SS, which, without passivation, is not present on the topmost surface. [151] Figure 6.2 shows an increase in molybdenum concentration from 0% before etching, to maximum of 3.0% after 90 minutes of etching. Energy dispersive X-ray (EDX) analysis on the same sample (data not shown) demonstrates further enrichment throughout the underlying layer with a molybdenum concentration of 6.7%; it should be noted that XPS analysis only probes the top 10 nm surface layer, whereas EDX samples up to 5 μm in depth, thus allowing

EDX to give a more complete analysis of the composition of the structures formed. The surface enrichment of molybdenum is a consequence of its resistance to HF acid etching. [152,153] Figure 6.5 shows spatial EDX mapping of the surface of a 90 minute HF acid etched 316(E) SS sample. The mapping shows increased molybdenum on the remaining grains, while the grain boundary regions show increased chromium and iron concentrations.

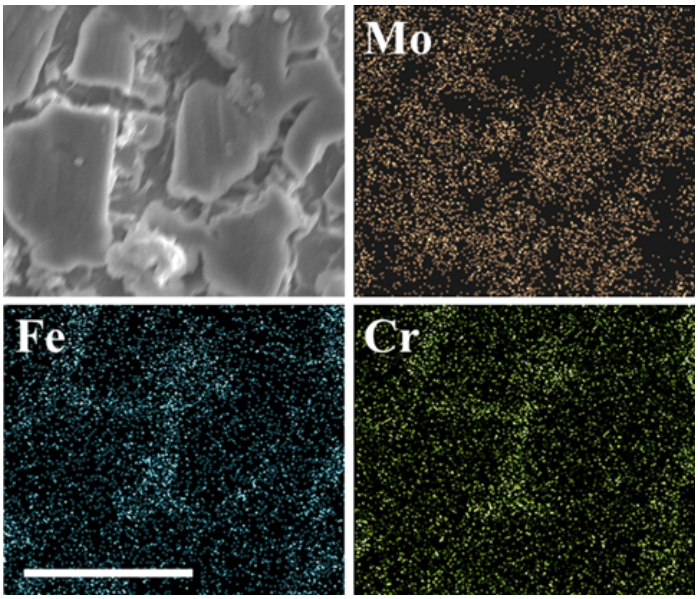

Figure 6.5: EDX mapping of molybdenum, iron and chromium on 316(E) SS etched for 90 min. The images show enrichment of molybdenum on the remaining grains, while iron and chromium are depleted in those areas. White scale bar represents 20 μm.

6.3.2 Passivation

In an oxygenated atmosphere, SS spontaneously forms a passivating chromium oxide layer, imparting corrosion resistance to SS. During the HF etch, the passivation layer is removed, exposing an iron rich surface that cannot re-establish passivation at ambient conditions. Figures 6.1 and 6.2 show a minimal chromium surface concentration

on both SS types after etching in HF, while the percentage in the bulk alloy is 18 wt. %. The lack of chromium at the surface inhibits formation of a passive oxide layer, resulting in a weakly adherent iron oxide and fluoride layer. When exposed to ambient conditions, unpassivated and uncoated SS samples therefore form an orange-colored iron oxide layer within one day of the HF etch. In addition, after the etch step, SS surfaces are covered by metal oxide and metal fluoride particles that display weak adhesion to the surface. Even a high velocity water jet from a standard wash bottle is sufficient to remove the precipitated structures from the surface. Both of these characteristics, lack of corrosion resistance and poor mechanical stability, are undesired outcomes of the HF etching process. By exposing the etched samples to nitric acid, the corrosion resistant properties of SS are restored.

The nitric acid bath treatment restores the SS passivation layer through the consumption of exogenous iron, as well as iron and chromium fluorides on the surface, thus allowing chromium to form a passive oxide layer on the surface. Figures 6.6 and 6.7 show the effect of passivation on 304 and 316 SS etched at 50°C, respectively, with a noticeable difference in surface roughness before and after passivation. Figures 6.6a-e show SEM images of 304(E) and (EP) SS etched in HF acid at 50°C, with and without passivation. Figure 6.6a shows an unetched 304 sample, while samples 304(E) SS in Figures 6.6b and 6.6c were etched in HF for 15 and 30 minutes, respectively, and Figures 6.6d and 6.6e display samples 304 (EP) SS that were etched for the same times and subsequently passivated in nitric acid. For both etch times, the passivation step effectively removes micrometer scale granular and crystalline roughness, exposing a flake-like structure.

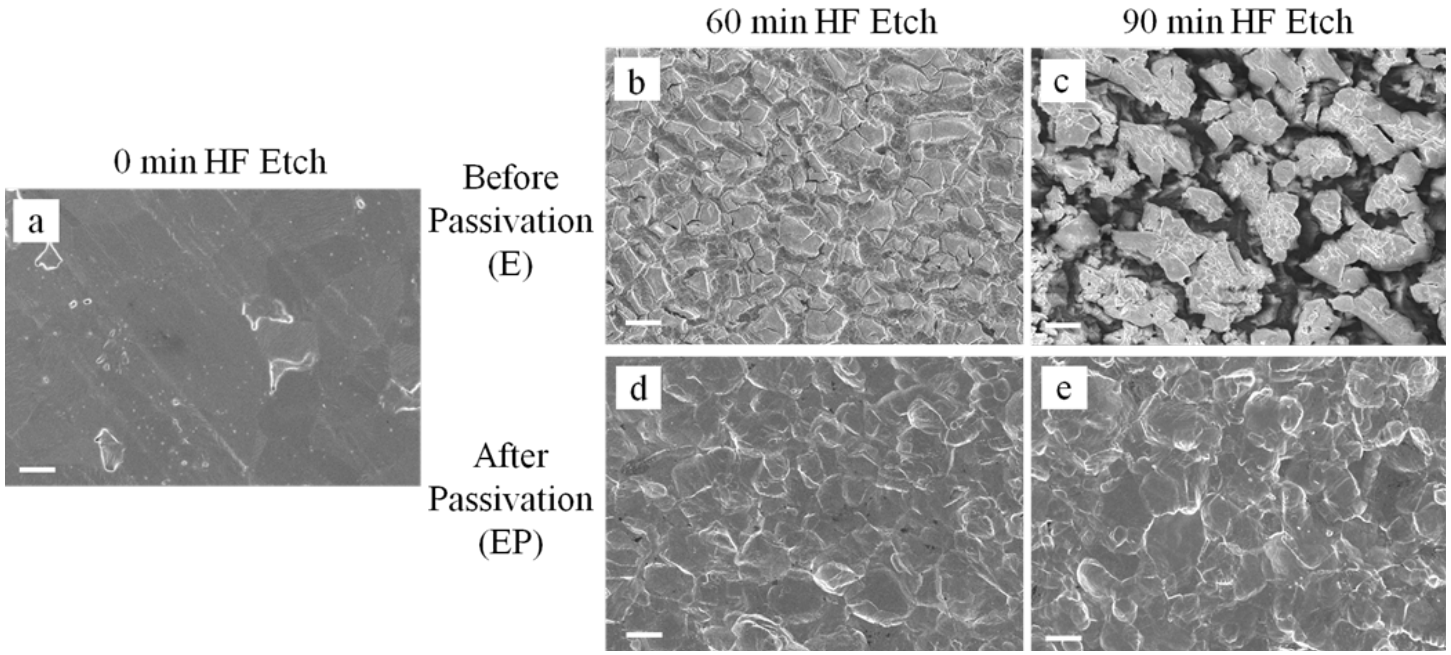

Figure 6.6: SEM images of unpassivated (E) and passivated (EP) HF acid etched (50°C) 304 SS for 0, 15 and 30 min etch times. White bars correspond to 10μm.

Figure 6.7a shows SEM images of an untreated sample of 316 SS. Figures 6.7b and 6.7d, and Figures 6.7c and 6.7e, show the surface before and after passivation after 60 and 90 minutes of etching, respectively. In both sets of images, it is evident that the passivation step removes much of the microscale roughness, exposing a large granular structure that greatly differs from the structures seen on 304(EP) SS (Figure 6.6). Again, intergranular corrosion appears to be the primary method of chemical attack, as is evident in Figures 6.7b and 6.7c.

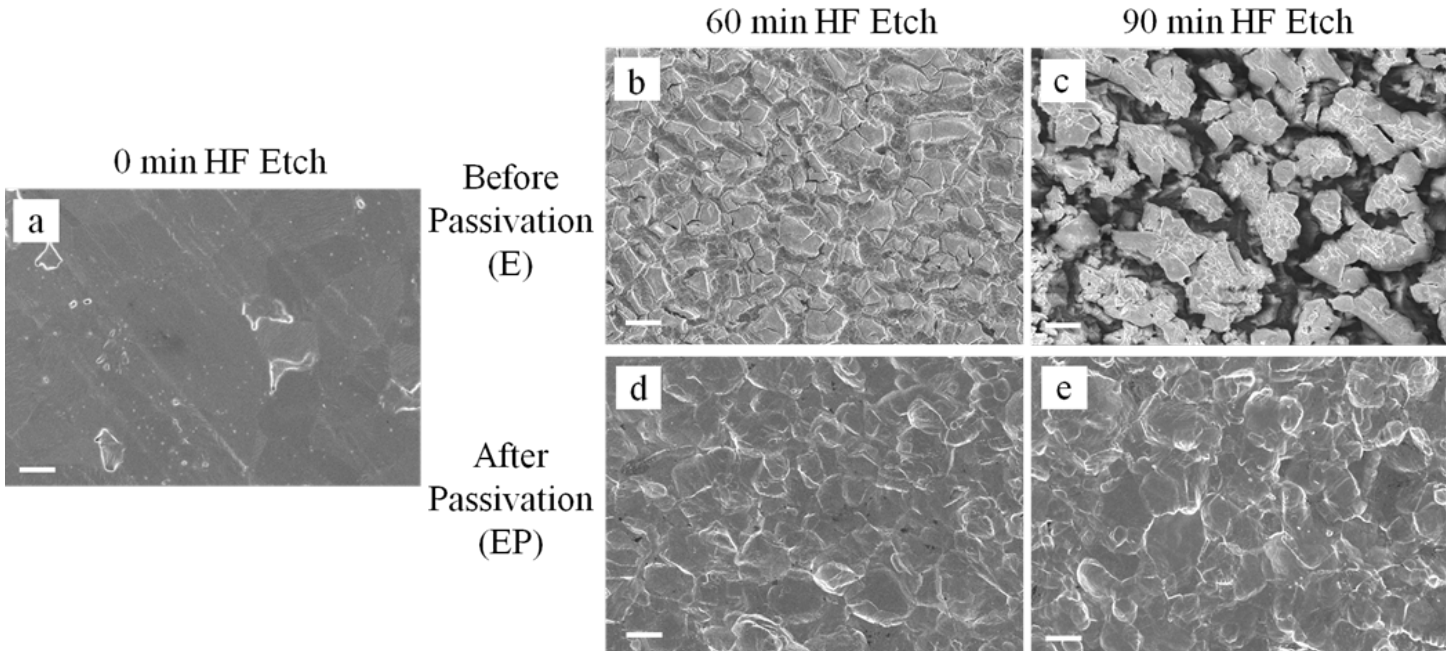

Figure 6.7: SEM images of unpassivated (E) and passivated (EP) HF acid etched (50°C) 316 SS for 0, 30, 60 and 90 min etch times. White bars correspond to 10 μm.

Samples of 316 SS experience a near complete removal of the surface structures. Nitric acid is known to readily dissolve molybdenum under the experimental conditions used here. [154] The surface structures that remain after passivation of 316 SS are the grains of the underlying SS. A higher magnification image of the surface of 316(EP) SS is shown in Figure 6.8a, with individual grains clearly visible. In contrast, the surface of 304(EP) SS remains roughened even after passivation. While the surface structure has been drastically changed by the passivation, it maintains its micron and sub-micron scale roughness, as shown in Figure 6.8b. XPS analysis after passivation (not shown) demonstrates the disappearance of the fluoride peaks for both iron and chromium, indicating that surface passivation has occurred on both SS types. Removal of the weakly adherent metallic fluorides in the passivation step reexposes the native SS, thus recovering the inherent mechanical strength of the underlying SS in the surface structures. More detailed physical durability testing of the surfaces is planned for future studies. The structures observed on 304(EP) SS after passivation have been reported before, albeit without a conclusive explanation of the mechanism. [155] It is our interpretation that the flake-like structure of passivated 304 SS is attributed to the cold rolling manufacturing process of the 304 SS shim sheets, which creates microstructures of deformation-induced martensite inclusions within austenitic grains. [156] The weakening of the microstructure boundaries during the HF acid etch allows nitric acid to selectively remove the martensitic phase. Well defined etch lines along these grain boundaries are visible in Figure 6.8. It has also been demonstrated that under the same cold rolling conditions 316 SS forms significantly less martensite, explaining structural differences after passivation. [156]

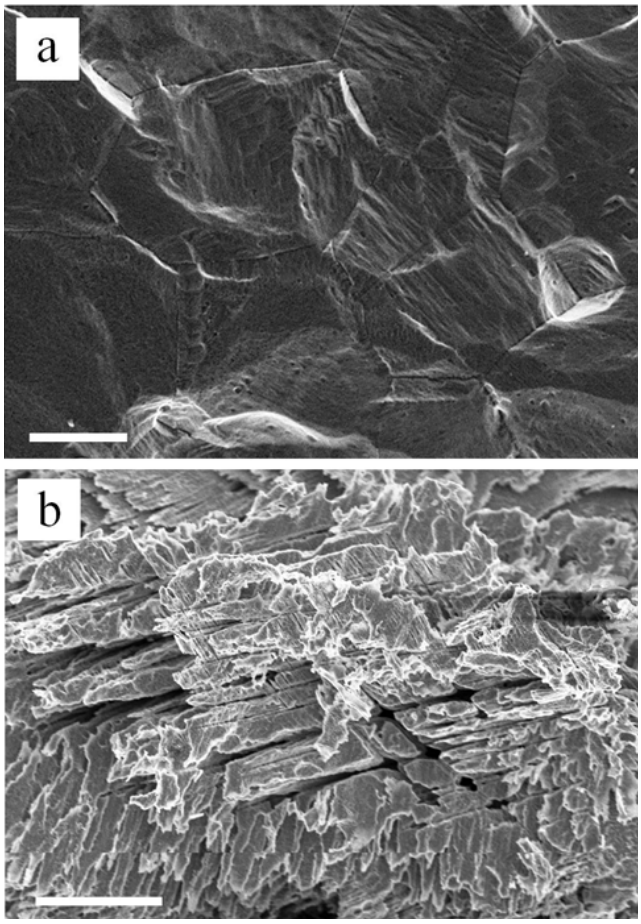

Figure 6.8: High magnification images of: a) 90 min etched 316(EP) SS, and b) 30 min etched 304(EP) SS at 50°C. White bars correspond to 5 μm.

6.3.3 Reestablishment of Chemical Passivity

Passivated samples were further tested for passivity using a standardized copper sulfate test (ASTM A380-06), during which a mixture of DI water, copper sulfate and sulfuric acid is placed on the surface of the metal. The existence of unalloyed iron on the surface would lead to the formation of metallic copper on the surface, which can readily be detected visually. Since this test was negative on our etched and passivated (EP) SS samples, it can be concluded that the passivation step successfully removes exogenous iron from the surface. While extensive electrochemical corrosion

studies are outside the scope of this study, preliminary experiments were conducted to demonstrate the establishment of a corrosion resistant, passivated surface. Similar thicknesses of plasma-deposited fluoropolymer films to those used in our studies have been shown to increase the corrosion resistance of carbon steel substrates. [157] In this study, samples of 304 and 316 (EP) and (EPF) stainless steels were placed in a 5 wt.% sodium chloride solution at 50°C. We observed that both (EP) and (EPF) samples of stainless steels exhibited corrosion resistance analogous to that of untreated samples, with all samples resisting surface discoloration for 15 days. In strong contrast, samples of 304 and 316(EF) stainless steels showed poor corrosion resistance. The samples discolored rapidly and spalled off the weakly adherent particle layer in less than 12 hrs, thus exposing the underlying SS to continued corrosion. These preliminary tests highlight the importance of the passivation step in recovering the desirable corrosion resistance of stainless steel.

6.3.4 Contact Angle Measurements on 304 Stainless Steel

The previous sections focused on chemical modifications due to the etch and passivation steps; that is, samples were analyzed prior to fluoropolymer deposition (with the corrosion tests as the only exception). In the following (Sections 6.3.4 and 6.3.5), we shift focus to the effects of surface structure on contact angle; as a consequence, samples with fluoropolymer coating are mainly discussed, except for a few relevant control samples.

Before processing, as received samples of 304 SS display a contact angle of 87.4°± 3.0. After passivation, without HF acid etch or fluoropolymer deposition, 304(P) SS shows a reduced contact angle of 75.2 ± 2.4°. This decrease is likely the result of removal of surface contamination imparted by the SS cold rolling process during passivation. Figure 6.9 shows the static contact angles, hysteresis and mean roughness of 304 (EF) and (EPF) SS etched with HF acid at 50°C as a function of etch

time. Without the fluoropolymer coating, both (E) and (EP) samples are hydrophilic (contact angle>20°) at all etch times due to changes in chemical and physical surface properties. Fluoropolymer thickness is not expected to play a significant role in the observed roughness due to the length scale of the deposition layer (100 nm) compared to the roughness measured (micrometer scale). The etch reaction proceeds rapidly upon immersion of the sample in the HF acid bath, with vigorous bubbling and immediate surface roughening; 5 minutes of etching increased the contact angle from 110.4± 3.7°to 155.3 ± 3.3°after fluoropolymer deposition.

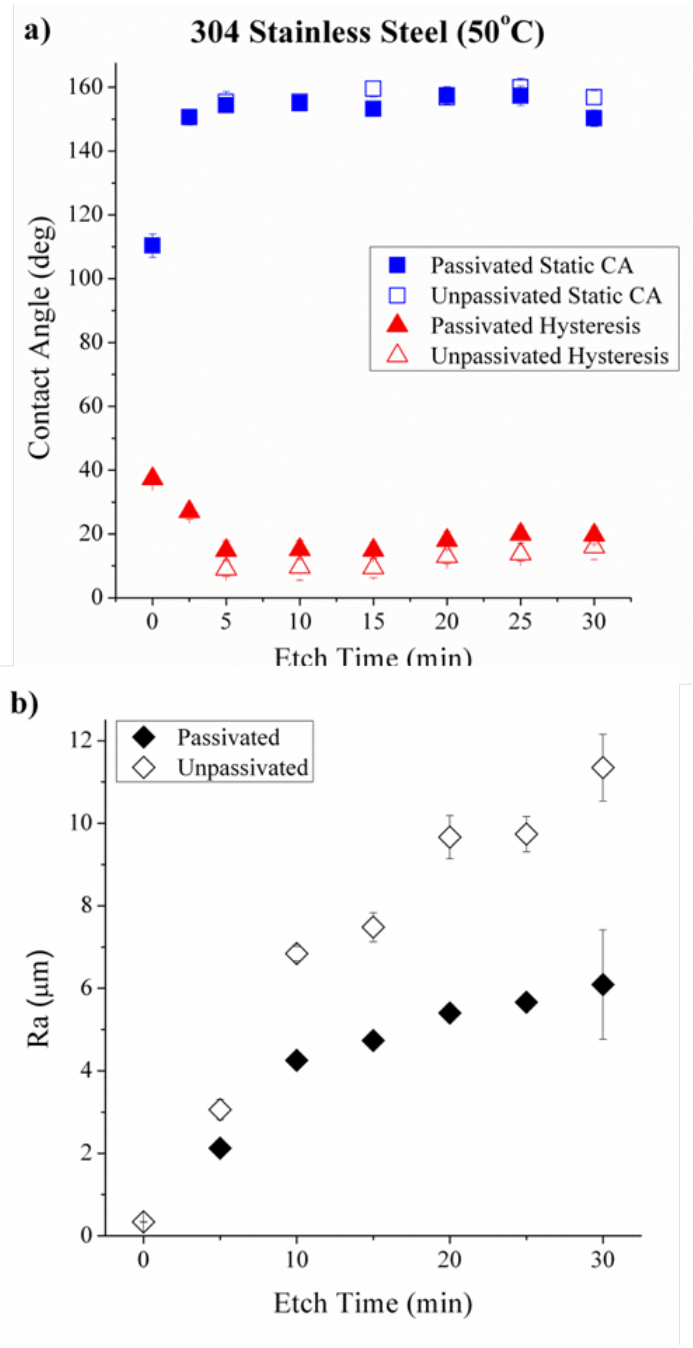

Figure 6.9: a) Static contact angles and hysteresis, and b) mean roughness measurements of passivated (EPF) and unpassivated (EF) 304 SS as function of duration of HF acid etch (50°C).

Figure 6.9b indicates that as etch time is increased, the mean roughness also increases, with unpassivated samples having a greater roughness at all etch times. As previously discussed, the passivation step removes the roughness created by the redeposition of metallic fluorides, exposing the martensitic-austenitic phase boundaries shown in Figure 6.8b. When comparing Figures 6.9a and 6.9b, it is clear that the prolonged etch and increased mean roughness have little effect on the static contact angle. After the first 5 minutes of etching, neither extended etching nor chemical passivation has an appreciable effect on the static contact angle. Unlike the static contact angle, the hysteresis increases slightly after passivation. The hysteresis reaches a minimum after 5 minutes of etching both before and after passivation, and then slowly increases with increasing etch time. Fabrication of superhydrophobic 304 SS through HF acid etch was also performed at room temperature (25°C). Figure 6.10 presents contact angle data of (EF) and (EPF) samples and the mean surface roughness for different etch times.

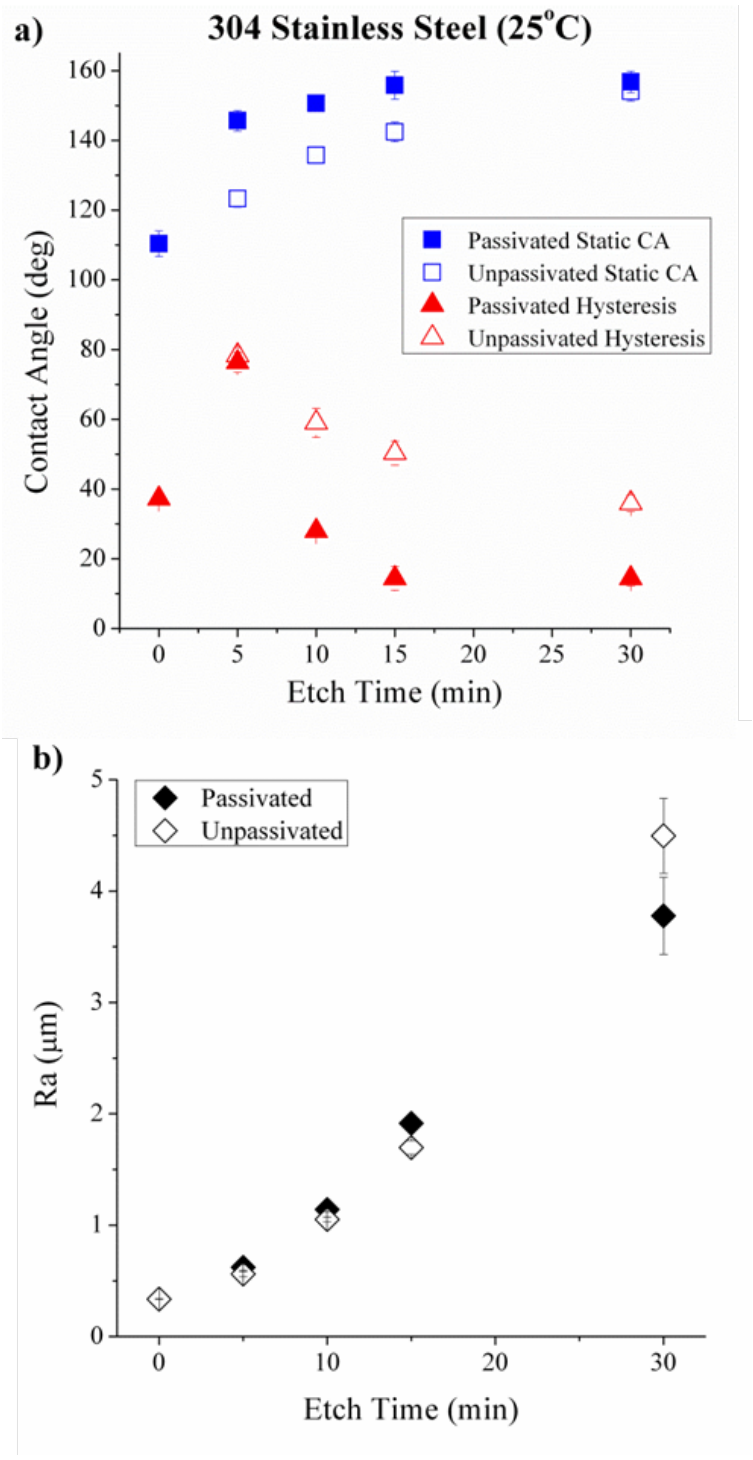

Figure 6.10: a) Static contact angles and hysteresis, and b) mean roughness measurements of passivated (EPF) and unpassivated (EF) 304 SS as function of duration of HF acid etch (25°C).

When compared to 304 SS samples etched at 50°C, the (EF) samples etched at 25°C exhibit a slower increase in contact angle and slower decrease in hysteresis. (EPF) samples, however, still rapidly attain high contact angles and low hysteresis. Although the R_a values after 30 min of etch and passivation vary greatly at the two different temperatures (6.09 μm $\pm$ 1.33 at 50°C and 3.78 μm $\pm$ 0.35 at 25°C), the static and dynamic contact angles are similar. It appears that the passivated samples are less affected by etch temperature. This is believed to be due to the fact that the acid etch weakens the martensitic-austenitic phase boundaries and thereby allows the nitric acid passivation to separate the phases and create the specific surface structures required for high contact angles. As shown in Figure 6.8b, the passivation step creates a flake-like structure from the unpassivated granular structure, thus allowing high contact angles even at relatively low mean roughness values.

6.3.5 Contact Angle Measurements on 316 Stainless Steel

Figure 6.11a shows static contact angles and hysteresis values of 316(EP) and (EPF) SS, while Figure 6.11b shows the mean roughness. Apparently due to manufacturing contamination issues, the contact angle of as received 316 SS was highly variable; after passivation and removal of surface contamination, the contact angle was 60.2 $\pm$ 2.8°. Fluoropolymer deposition increases the contact angle of 316(F) SS sample to 103.9 $\pm$ 3.4°. Similar to 304 SS, without fluoropolymer deposition, the acid etch and passivation steps render the 316 grade SS samples hydrophilic (contact angle <20°) for all etch times. The reaction of 316 SS in HF acid occurs at a visibly slower rate, requiring longer times before signs of etching are evident, for instance through the observation of bubble formation. Comparison of R_a values for 304 and 316 SS (Figures 6.9b and 6.11b) indicates that surface roughness generation on 316 SS occurs at a markedly slower rate than that observed for 304 SS. After 90 min of HF acid etch, a sample of 316(EF) SS has R_a = 2.5 μm $\pm$ 0.5, while after only 5 min of etching,

a sample of 304(EF) SS has already exceeded that value (R_a = 3.06 μm $\pm$ 0.25). The reduced rate of surface roughness formation on 316 SS, along with the granular structure of the roughness, explains the lowered contact angles when compared to 304 SS for similar etch times. The increased hysteresis observed in 316 SS samples is most likely due to wetting in the Wenzel state, while 304 SS samples have the characteristics of a Cassie-Baxter state. [35] For both unpassivated and passivated samples it is obvious that as etch time is increases, the static contact angle increases as well, with the maximum average contact angle reaching 146.6 $\pm$ 3.2° after 90 min of etching for the unpassivated sample (after fluoropolymer deposition). Unlike 304 SS, passivation of 316 SS notably decreases the static contact angle by an average of 9.1°.

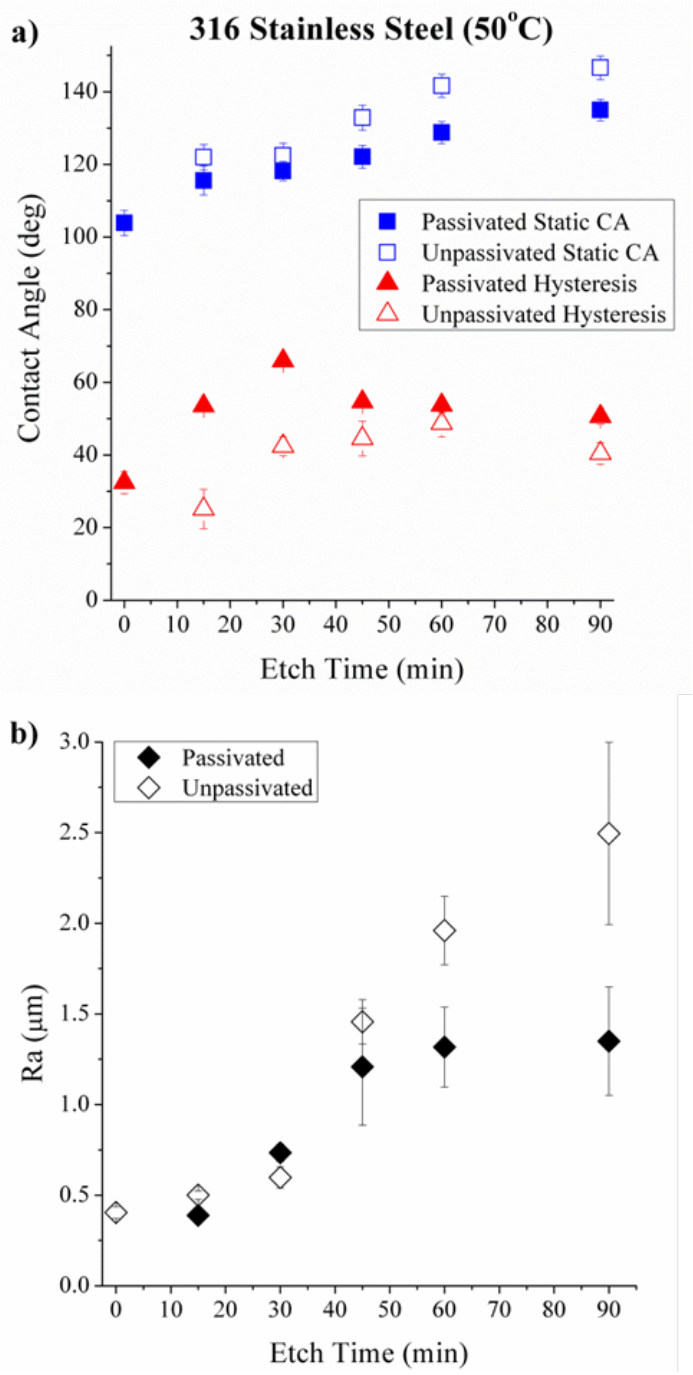

Figure 6.11: a) Static contact angles and hysteresis, and b) mean roughness measurements of passivated (EPF) and unpassivated (EF) 316 SS as function of duration of HF acid etch (50°C).

6.4 Conclusions

By etching 304 and 316 SS samples in HF acid, followed by passivation in nitric acid and fluoropolymer deposition, we have demonstrated the ability to create superhydrophobic SS surfaces that maintain the corrosive properties of untreated stainless steels, while changing the wetting properties significantly. Both types of SS are initially etched through intergranular corrosion. As etch times increase, 304 SS forms micrometer and sub-micrometer scale surface roughness due to the formation of iron and chromium oxides and fluorides, with a sample of 304(EF) SS achieving a contact angle of 159.9 $\pm$ 2.8° and a hysteresis of 13 $\pm$ 2.2° after 25 min of etching at 50°C. The ability to etch 304 SS at 25°C was also demonstrated, attaining a contact angle of 156.7 $\pm$ 3.0° and a hysteresis of 14.4 $\pm$ 2.2° with the (EF) treatments. Due to the molybdenum content in 316 SS, the etch rate is significantly reduced, resulting in decreased roughness. For a sample of 316(EF), the reduced etch rate leads to a maximum contact angle of 146.6 $\pm$ 3.2° with a hysteresis of 40.4 $\pm$ 2.9° after 90 min of etching. However, after HF acid etching, both types of SS are no longer corrosion resistant, since the passivation layer has been removed by the etch process.

Chemical passivation in nitric acid was employed to restore the beneficial corrosion resistant properties that are characteristic of SS. Through the removal of iron and metallic fluorides, the passive chromium oxide layer is restored, while the remaining surface roughness leads to sustained high contact angles and low hysteresis. A static contact angle of 157.3 $\pm$ 2.8° was found on 304(EPF) SS that was etched for 25 min at 50°C. The three-step process described provides a simple method of fabricating superhydrophobic stainless steel surfaces, while maintaining corrosion resistance.

CHAPTER VII

CONCLUSIONS AND FUTURE WORK

Superhydrophobic and superoleophobic surfaces have only recently been developed to a point that enables commercialization. However, hurdles remain; the durability of these surfaces is often poor, fabrication is tedious and expensive, environmentally harmful chemicals are required. To support development and utilization of these surfaces, this thesis focuses on understanding the physical and chemical requirements of superhydrophobic and superoleophobic surfaces and novel ways to satisfy them.

In Chapter 2 we functionalize superhydrophobic paper with wax dots to create microfluidic devices capable of sampling small fluid volumes from bulk droplets. While hydrophobic, the printed wax dots remain less hydrophobic and have a higher hysteresis than the surrounding superhydrophobic paper onto which they are printed. The difference in wetting between the wax and paper causes selective adhesion of fluid droplets to the printed design. We take advantage of this effect by contacting wax patterns printed on a superhydrophobic sheet of paper with a bulk droplet resting on another superhydrophobic sheet. By separating the printed sheet from the droplet, a sample volume is preferentially adhered to the wax pattern. It is further shown that the volume sampled can be controlled via the hysteresis of the wax dot. A higher hysteresis dot exerts a greater adhesion force onto the droplet, allowing it to sample a larger volume. The hysteresis of the wax is modified through two different mechanisms: physical and chemical. Physically, the hysteresis was changed through the addition of roughness to the wax by pressing the dots against various grades of sand paper, which consiste of different particle sizes, and thus represent different roughness levels. Chemically, the hysteresis was modified by implementing different

types of waxes; paraffin, carnauba and stearic acid and mixtures thereof were used.

Chapter 3 demonstrates that the ability to extend the repellency of paper to fluids other than water and thus repel lower surface tension fluids like oils. This nontrivial task is accomplished through a combination of fiber refining, solvent exchange and plasma processing. The fiber refining tears the larger diameter fibers apart, creating smaller diameter fibrils. These fibrils help to support lower surface tension fluids in the meta-stable Cassie-Baxter state that is required of superoleophobic surfaces. When formed with water, paper sheets made from this mechanically refined pulp clump together and form a non-porous surface structure due to the interfiber bonding. To allow the separation of these fibrils, a solvent exchange process is used, whereby the water implemented in the paper processing is replaced by sec-butanol, and then dried. The sec-butanol inhibits fiber-fiber hydrogen bonding, allowing a more porous structure to form. Finally, use of oxygen plasma etching to create nano-structure is combined with a fluoropolymer deposition to create superamphiphobic paper. These superamphiphobic paper substrates exhibit contact angles $>150^\circ$ for water, ethylene glycol, motor oil and n-hexadecane.

To avoid the loss of strength associated with the solvent exchange processed used in Chapter 3 a layering process is applied in Chapter 4. Using a standard water processed handsheet as a base, a porous, low weight sheet is attached to the surface. The addition of this layer increases the average roughness of the sheet and when combined with etching and fluoropolymer deposition yields a greater increase in n-hexadecane contact angles when compared to non-layered sheets.

For the first time, superhydrophobic surfaces on paper were created by use of a non-fluorinated hydrophilic coating (Chapter 5). Coating paper with a plasma deposited diamond-like carbon (DLC) thin film ($\theta_e = 68.2 \pm 1.5^\circ$) yields a slightly hydrophobic surface with an advancing water contact angle of $118.6 \pm 4.7^\circ$. While

hydrophobic, the unetched paper surface exhibits a high hysteresis, with the receding contact angle <20°. As discussed, the oxygen plasma etching creates nanoscale structures. Short etch times provide slight increases in both the advancing and receding contact angles, however the surface remains high hysteresis. By increasing the etch times micron level structures begin to form. The physical changes of both micron and nanoscale fiber structures increase the advancing and receding contact angles, eventually overcoming the inherent hydrophilicity of the DLC and forming a superhydrophobic surface analogous to those created using fluoropolymers.

Following the same fundamental parameters that were used to create superhydrophobic surfaces, Chapter 6 uses stainless steel as a substrate. A hydrofluoric acid bath is utilized to etch the two most widely used stainless steels, 304 and 316. The acid etch forms surface roughness through intergranular corrosion, combined with the redeposition of metallic oxides and fluorides. 304 type stainless steel etches at a much faster rate relative to 316 due to the presence of molybdenum in 316. As a result of this variation in etch rate, the formation of roughness and thus the contact angle increase of etched 304 occurs much more rapidly when compared to 316. After coating the stainless steel samples with a plasma deposited fluoropolymer layer, maximum water contact angles of 159.9° and 146.6° are attained for 304 and 316, respectively. Unfortunately, after the etch process the stainless steels are no longer resistant to surface corrosion. To reestablish this corrosion resistant layer, a passivation treatment is performed on hydrofluoric acid etched samples using nitric acid. After passivation, samples of 304 and 316 exhibit maximum water contact angles of 157.3° and 134.9°.

To summarize what has been learned, general comments will be made regarding the requirements for the unique wetting properties reported in this thesis. Many of the surfaces that are studied in this thesis require that fluids reside in the Cassie-Baxter wetting state (Figure 1.1b and Equation 5.3). In this state, the fluid is in partial contact with both the solid surface and air pockets between the fluid and substrate.

The higher the roughness levels, the smaller the fraction of fluid in direct contact with the solid substrate and, consequently, the higher the apparent contact angle. In addition to roughness, the Cassie-Baxter equation dictates that the apparent contact angle is also a function of the equilibrium contact angle which defines wetting on a flat substrate. This parameter depends on both the surface energy of the solid and on the surface tension of the studied fluid. Of course, the Cassie-Baxter equation only offers a basic model for surfaces exhibiting high fluid repellency, but it captures important aspects of the observed phenomena and provides significant insight into fluid wetting. Adding a thin fluorinated surface layer to paper handsheets with fiber diameters of 20-30 μm and average surface roughness (R_a) values of $\sim$6 μm was found to yield static water contact angles of $\sim 140°$(Figure 5.4). While this is a relatively high contact angle, the inability to reach the 150° benchmark of superhydrophobicity is caused by the relatively high contact area between the water drop and individual fibers. Through the creation of nanoscale roughness on individual fibers using plasma etching ($R_a \approx 100$ nm), a water contact angle above 150° can easily be generated. The combination of nanoscale roughness on the fiber surface with the micronscale roughness provided by the fibrous network significantly decreases the solid surface area that contacts a resting water droplet. While this level of roughness is sufficient to yield high contact angle for paper coated with a fluoropolymer, the higher surface energy of DLC surfaces requires that even less solid be in contact with a water droplet resting on the surface. The work in this thesis has shown that the difference in equilibrium contact angles ($\theta_e^{PFE} \approx 110°$ and $\theta_e^{DLC} \approx 68°$) can be compensated for by decreased fiber diameters, which are generated through prolonged oxygen etching. Based on SEM images (Figure 5.8) a combination of thin fibers (diameter <5 μm) with larger diameter fibers (>20 μm) and nanoscale fiber roughness decreases the contact area of the water enough to raise the contact angle above 150° even for DLC coated paper. To obtain a low hysteresis surface, even greater roughness is required,

regardless of the coating properties. For the stainless steel surfaces studied, R_a values of >3 μm are required to reach water contact angles of 150°. The surfaces of the etched stainless steel differ greatly from the fiber based structures of paper, and thus lead to different requirements of the roughness values.

The design parameters outlined above do not accurately describe fiber wetting when oils are used as the test fluid. Increased etched times to enhance roughness display a detrimental effect on the n-hexadecane contact angle (Figure 3.6). While the formation of nanoscale increases the contact angle, the critical design parameter for highly oil repellent surfaces is the average spacing of fibers. Based on calculations from the Cassie-Baxter equation (Equation 3.1), using fibers diameters of 10-20 μm, fiber-fiber spacings must be $\sim$200 μm. SEM images (Figure 3.8c) indicate that the superoleophobic paper surfaces produced in this thesis indeed have average spacings consistent with these lengthscales. It is important to note that these fiber spacings, and the resulting pore sizes, are much larger than those normally seen in the paper industry. The solvent exchange process employed in this thesis demonstrates the ability to achieve such porous paper substrates, but does so at great expense to the paper's strength. Alternatively, low density layers of paper can be layered on top of standard water formed paper to yield increases in the surface porosity without reducing the bulk strength. However, without further modifications to the forming techniques, the fiber-fiber spacings of the layered sheets are insufficient to yield high oil contact angles.

7.1 Future Work and Recommendations

While significant work has been completed to functionalize paper substrates and create superhydrophobic and superoleophobic surfaces, this thesis also provides inspiration and support for future work.

Although the superoleophobic surfaces created in this study are while extremely

water and oil repellent, they are mechanically fragile. The solvent processing that we rely on to prevent hydrogen bonding and yield the correct fiber spacing also dramatically decreases the strength of the paper. It is this fiber-fiber bonding that creates the strength of the water formed paper products. In the end, it is not only the bulk strength of the sheet that is diminished, the surface structure that yields the correct spacing for superamphiphobicity lacks mechanical stability as well. Often, removal of a deposited droplet from the surface will also remove the fibers that were in contact with it. To create stronger more robust superamphiphobic paper sheets, two approaches can be considered: the sheets can be processed using an alternative solvent, even water, while other techniques are used to dictate the spacing, or a post-processing technique can be utilized to fix the spacing created by the solvent exchange processing. Fiber-fiber spacings can be defined using chemical additives to the pulp phase. In this thesis, Chapter 4 has shown promising results laminating highly porous, low weight sheets to the surfaces of standard handsheets. Since these sheets are formed with water, they retain the strength of not only the bulk sheet, but the structures as well. Future studies are required to increase the contact angle above 150°.

Additionally, the superamphiphobic paper substrates detailed in Chapter 3 are high hysteresis surfaces for the lower surface tension fluids. Recently it has been shown by Kota *et al.* that surfaces with a hierarchical structure can exhibit roll-off behavior for fluids such as *n*-hexadecane. [112] In principle, the plasma etching process creates this type of structure with nano-scale structures formed by selective etching of the amorphous phase of cellulose. However, these low hystersis properties are not observed on our substrates. Part of the problem that prevents implementation of the information from Kota's work is limited the ability to controllably define the fiber-fiber spacing. Further development of the ability to establish fiber-fiber spacing is required if low hysteresis superamphiphobic paper is be achieved.

The work conducted using DLC to create superhydrophobic paper also has a promising future. These superhydrophobic substrates can be functionalized using metal doped DLC. Incorporation of metals such as iron, aluminum and silver into DLC films can increase the equilibrium water contact angle, [158, 159] and yield improvements in the robustness and stability of superhydrophobic surfaces. Further, incorporation of metals into a superhydrophobic surface may create an electrically conductive paper based material, which could have a wide variety of applications. For silver doped DLC in particular, superhydrophobic paper surfaces could be created that resist bacterial growth, taking advantage of the inherent antibacterial properties of silver.

REFERENCES

[1] M. Ek, G. Gellerstedt, and G. Henriksson, Pulp and Paper Chemistry and Technology: Paper Products Physics and Technology. Germany: Walter de Gruyter & Co, 2009, vol. 4.

[2] M. A. Hubbe, "Paper's resistance to wetting- a review of internal sizing chemicals and their effects," Bioresources, vol. 2, no. 1, pp. 106–145, 2007.

[3] D. Holik, Handbook of Paper and Board. Weinhem: Wiley, 2006.

[4] J. Asuncion, The Complete Book of Papermaking. New York: Lark Books, 2001.

[5] D. Barona and A. Amirfazli, "Producing a superhydrophobic paper and altering its repellency through ink-jet printing," Lab on a Chip, vol. 11, no. 5, pp. 936–940, 2011.

[6] J. BeMiller and R. Whistler, Starch: Chemistry and Technology, 3rd ed. Elseveir, 2009.

[7] F. Aloi, R. Trksak, and V. Mackwicz, "The effect of base sheet properties and wet end chemistry on surface-sized paper," in TAPPI 2001 Papermakers Conference, 2001.

[8] H. H. Espy, "The mechanism of wet-strength development in paper - a review," Tappi Journal, vol. 78, no. 4, pp. 90–99, 1995.

[9] H. Yang and Y. Deng, "Preparation and physical properties of superhydrophobic papers," Journal of Colloid and Interface Science, vol. 325, no. 2, pp. 588–593, 2008.

[10] X. M. Li, D. Reinhoudt, and M. Crego-Calama, "What do we need for a superhydrophobic surface? a review on the recent progress in the preparation of superhydrophobic surfaces," Chemical Society Reviews, vol. 36, no. 8, pp. 1350–1368, 2007.

[11] P. Roach, N. J. Shirtcliffe, and M. I. Newton, "Progess in superhydrophobic surface development," Soft Matter, vol. 4, no. 2, pp. 224–240, 2008.

[12] R. Furstner, W. Barthlott, C. Neinhuis, and P. Walzel, "Wetting and self-cleaning properties of artificial superhydrophobic surfaces," Langmuir, vol. 21, no. 3, pp. 956–961, 2005.

[13] M. Callies and D. Quere, "On water repellency," Soft Matter, vol. 1, no. 1, pp. 55–61, 2005.

[14] H. Mertaniemi, V. Jokinen, L. Sainiemi, S. Franssila, A. Marmur, O. Ikkala, and R. Ras, "Superhydrophobic tracks for low-friction, guided transport of water droplets," Advanced Materials, vol. 23, pp. 2911–2914, 2011.

[15] D. Quere, "Wetting and roughness," Annual Review of Materials Research, vol. 38, pp. 71–99, 2008.

[16] F. Xia and L. Jiang, "Bio-inspired, smart, multiscale interfacial materials," Advanced Materials, vol. 20, no. 15, pp. 2842–2858, 2008.

[17] A. Carre, "Polar interactions at liquid/polymer interfaces," Journal of Adhesion Science and Technology, vol. 21, no. 10, pp. 961–981, 2007.

[18] B. Balu, V. Breedveld, and D. W. Hess, "Fabrication of "roll-off" and "sticky" superhydrophobic cellulose surfaces via plasma processing," Langmuir, vol. 24, no. 9, pp. 4785–4790, 2008.

[19] Z. G. Guo, F. Zhou, and W. M. Liu, "Preparation of biomimetic superhydrophobic silica film by sol-gel technique," Acta Chimica Sinica, vol. 64, no. 8, pp. 761–766, 2006.

[20] H. Tavana, A. Amirfazli, and A. W. Neumann, "Fabrication of superhydrophobic surfaces of n-hexatriacontane," Langmuir, vol. 22, no. 13, pp. 5556–5559, 2006.

[21] A. Tuteja, W. Choi, M. L. Ma, J. M. Mabry, S. A. Mazzella, G. C. Rutledge, G. H. McKinley, and R. E. Cohen, "Designing superoleophobic surfaces," Science, vol. 318, no. 5856, pp. 1618–1622, 2007.

[22] A. Nakajima, K. Hashimoto, T. Watanabe, K. Takai, G. Yamauchi, and A. Fujishima, "Transparent superhydrophobic thin films with self-cleaning properties," Langmuir, vol. 16, no. 17, pp. 7044–7047, 2000.

[23] J. Bravo, L. Zhai, Z. Z. Wu, R. E. Cohen, and M. F. Rubner, "Transparent superhydrophobic films based on silica nanoparticles," Langmuir, vol. 23, no. 13, pp. 7293–7298, 2007.

[24] A. Safaee, D. K. Sarkar, and M. Farzaneh, "Superhydrophobic properties of silver-coated films on copper surface by galvanic exchange reaction," Applied Surface Science, vol. 254, no. 8, pp. 2493–2498, 2008.

[25] B. T. Qian and Z. Q. Shen, "Fabrication of superhydrophobic surfaces by dislocation-selective chemical etching on aluminum, copper, and zinc substrates," Langmuir, vol. 21, no. 20, pp. 9007–9009, 2005.

[26] F. Z. Zhang, L. L. Zhao, H. Y. Chen, S. L. Xu, D. G. Evans, and X. Duan, "Corrosion resistance of superhydrophobic layered double hydroxide films on aluminum," Angewandte Chemie-International Edition, vol. 47, no. 13, pp. 2466–2469, 2008.

[27] J. Fresnais, J. P. Chapel, and F. Poncin-Epaillard, "Synthesis of transparent superhydrophobic polyethylene surfaces," Surface & Coatings Technology, vol. 200, no. 18-19, pp. 5296–5305, May 2006.

[28] G. McHale, N. J. Shirtcliffe, and M. I. Newton, "Contact-angle hysteresis on super-hydrophobic surfaces," Langmuir, vol. 20, no. 23, pp. 10 146–10 149, 2004.

[29] Y. Xiu, L. Zhu, D. W. Hess, and C. P. Wong, "Hierarchical silicon etched structures for controlled hydrophobicity/superhydrophobicity," Nano Letters, vol. 7, no. 11, pp. 3388–3393, 2007.

[30] J. Y. Shiu, C. W. Kuo, P. L. Chen, and C. Y. Mou, "Fabrication of tunable superhydrophobic surfaces by nanosphere lithography," Chemistry of Materials, vol. 16, no. 4, pp. 561–564, 2004.

[31] M. Morra, E. Occhiello, and F. Garbassi, "Contact-angle hysteresis in oxygen plasma treated poly(tetrafluoroethylene)," Langmuir, vol. 5, no. 3, pp. 872–876, 1989.

[32] A. Tuteja, W. J. Choi, G. H. McKinley, R. E. Cohen, and M. F. Rubner, "Design parameters for superhydrophobicity and superoleophobicity," Mrs Bulletin, vol. 33, no. 8, pp. 752–758, 2008.

[33] R. N. Wenzel, "Resistance of solid surfaces to wetting by water," Industrial and Engineering Chemistry, vol. 28, pp. 988–994, 1936.

[34] A. B. D. Cassie and S. Baxter, "Wettability of porous surfaces," Transactions of the Faraday Society, vol. 40, pp. 0546–0550, 1944.

[35] A. Lafuma and D. Quere, "Superhydrophobic states," Nature Materials, vol. 2, no. 7, pp. 457–460, 2003.

[36] A. M. Pirttila and A. Frank, Endophytes of Forest Trees. Springer, 2011.

[37] B. Balu, J. S. Kim, V. Breedveld, and D. W. Hess, "Tunability of the adhesion of water drops on a superhydrophobic paper surface via selective plasma etching," Journal of Adhesion Science and Technology, vol. 23, no. 2, pp. 361–380, 2009.

[38] D. Nystrom, J. Lindqvist, E. Ostmark, A. Hult, and E. Malmstrom, "Superhydrophobic bio-fibre surfaces via tailored grafting architecture," Chemical Communications, no. 34, pp. 3594–3596, 2006.

[39] G. Decher and J. D. Hong, "Buildup of ultrathin multilayer films by a self-assembly process .1. consecutive adsorption of anionic and cationic bipolar amphiphiles on charged surfaces," Makromolekulare Chemie-Macromolecular Symposia, vol. 46, pp. 321–327, 1991.

[40] G. Decher, "Fuzzy nanoassemblies: Toward layered polymeric multicomposites," Science, vol. 277, no. 5330, pp. 1232–1237, 1997.

[41] E. Sutermeister, Chemistry of pulp and paper making. Nabu Press, 1920.

[42] Z. S. Hu, X. Y. Zen, J. Gong, and Y. L. Deng, "Water resistance improvement of paper by superhydrophobic modification with microsized caco(3) and fatty acid coating," Colloids and Surfaces a-Physicochemical and Engineering Aspects, vol. 351, no. 1-3, pp. 65–70, 2009.

[43] M. Lex and O. Tamms, "Kaolin fillers under changing papermaking conditions," Wochenblatt Fur Papierfabrikation, vol. 131, no. 5, pp. 233–237, 2003.

[44] B. Mesic, C. Kugge, and L. Jarnstrom, "Superhydrophobic paper coating containing non-conventional clay," Tappi Journal, 2010.

[45] J. d. Clark, Pulp Technology and Treatment for Paper. San Francisco, CA: Miller Freeman, 1985.

[46] H. Teisala, M. Tuominen, M. Aromaa, J. M. Makela, M. Stepien, J. J. Saarinen, M. Toivakka, and J. Kuusipalo, "Development of superhydrophobic coating on paperboard surface using the liquid flame spray," Surface & Coatings Technology, vol. 205, no. 2, pp. 436–445, 2010.

[47] K. Hashimoto, H. Irie, and A. Fujishima, "Tio2 photocatalysis: A historical overview and future prospects," Japanese Journal of Applied Physics Part 1-Regular Papers Brief Communications & Review Papers, vol. 44, no. 12, pp. 8269–8285, 2005.

[48] H. Teisala, M. Tuominen, M. Stepien, J. Haapanen, J. M. Makela, J. J. Saarinen, M. Toivakka, and J. Kuusipalo, "Wettability conversion on the liquid flame spray generated superhydrophobic tio2 nanoparticle coating on paper and board by photocatalytic decomposition of spontaneously accumulated carbonaceous overlayer," Cellulose, vol. 20, no. 1, pp. 391–408, 2013.

[49] L. H. Huang, K. F. Chen, C. X. Lin, R. D. Yang, and R. A. Gerhardt, "Fabrication and characterization of superhydrophobic high opacity paper with titanium dioxide nanoparticles," Journal of Materials Science, vol. 46, no. 8, pp. 2600–2605, 2011.

[50] S. H. Li, H. B. Xie, S. B. Zhang, and X. H. Wang, "Facile transformation of hydrophilic cellulose into superhydrophobic cellulose," Chemical Communications, no. 46, pp. 4857–4859, 2007.

[51] S. H. Li, S. B. Zhang, and X. H. Wang, "Fabrication of superhydrophobic cellulose-based materials through a solution-immersion process," Langmuir, vol. 24, no. 10, pp. 5585–5590, 2008.

[52] S. J. Li, Y. Q. Wei, and J. G. Huang, "Facile fabrication of superhydrophobic cellulose materials by a nanocoating approach," Chemistry Letters, vol. 39, no. 1, pp. 20–21, 2010.

[53] G. R. J. Artus, S. Jung, J. Zimmermann, H. P. Gautschi, K. Marquardt, and S. Seeger, "Silicone nanofilaments and their application as superhydrophobic coating," Advanced Materials, vol. 18, no. 20, pp. 2758–+, 2006.

[54] A. Y. Fadeev and T. J. McCarthy, "Self-assembly is not the only reaction possible between alkyltrichlorosilanes and surfaces: Monomolecular and oligomeric covalently attached layers of dichloro- and trichloroalkylsilanes on silicon," Langmuir, vol. 16, no. 18, pp. 7268–7274, 2000.

[55] C. Quan, O. Werner, L. Wagberg, and C. Turner, "Generation of superhydrophobic paper surfaces by a rapidly expanding supercritical carbon dioxide-alkyl ketene dimer solution," Journal of Supercritical Fluids, vol. 49, no. 1, pp. 117–124, 2009.

[56] O. Werner, C. Quan, C. Turner, B. Pettersson, and L. Wagberg, "Properties of superhydrophobic paper treated with rapid expansion of supercritical co(2) containing a crystallizing wax," Cellulose, vol. 17, no. 1, pp. 187–198, 2010.

[57] S. Shibuichi, T. Yamamoto, T. Onda, and K. Tsujii, "Super water- and oil-repellent surfaces resulting from fractal structure," Journal of Colloid and Interface Science, vol. 208, no. 1, pp. 287–294, 1998.

[58] S. Shibuichi, T. Onda, N. Satoh, and K. Tsujii, "Super water-repellent surfaces resulting from fractal structure," Journal of Physical Chemistry, vol. 100, no. 50, pp. 19 512–19 517, 1996.

[59] M. B. O. Riekerink, J. G. A. Terlingen, G. H. M. Engbers, and J. Feijen, "Selective etching of semicrystalline polymers: Cf4 gas plasma treatment of poly(ethylene)," Langmuir, vol. 15, no. 14, pp. 4847–4856, 1999.

[60] B. Balu, A. D. Berry, D. W. Hess, and V. Breedveld, "Patterning of superhydrophobic paper to control the mobility of micro-liter drops for two-dimensional lab-on-paper applications," Lab on a Chip, vol. 9, no. 21, pp. 3066–3075, 2009.

[61] B. Balu, A. D. Berry, K. T. Patel, V. Breedveld, and D. W. Hess, "Directional mobility and adhesion of water drops on patterned superhydrophobic surfaces," Journal of Adhesion Science and Technology, vol. 25, no. 6-7, pp. 627–642, 2011 2011.

[62] D. Buser, N. Broggini, M. Wieland, R. K. Schenk, A. J. Denzer, D. L. Cochran, B. Hoffmann, A. Lussi, and S. G. Steinemann, "Enhanced bone apposition to a chemically modified sla titanium surface," Journal of Dental Research, vol. 83, no. 7, pp. 529–533, 2004.

[63] D. L. Cochran, D. Buser, C. M. ten Bruggenkate, D. Weingart, T. M. Taylor, J. P. Bernard, F. Peters, and J. P. Simpson, "The use of reduced healing times on iti (r) implants with a sandblasted and acid-etched (sla) surface: Early results from clinical trials on iti (r) sla implants," Clinical Oral Implants Research, vol. 13, no. 2, pp. 144–153, 2002.

[64] E. Fadeeva, V. K. Truong, M. Stiesch, B. N. Chichkov, R. J. Crawford, J. Wang, and E. P. Ivanova, "Bacterial retention on superhydrophobic titanium surfaces fabricated by femtosecond laser ablation," Langmuir, vol. 27, no. 6, pp. 3012–3019, 2011.

[65] E. Fadeeva, S. Schlie, J. Koch, A. Ngezahayo, and B. N. Chichkov, "The hydrophobic properties of femtosecond laser fabricated spike structures and their effects on cell proliferation," Physica Status Solidi a-Applications and Materials Science, vol. 206, no. 6, pp. 1348–1351, 2009.

[66] A. Vilcnik, I. Jerman, A. S. Vuk, M. Kozelj, B. Orel, B. Tomsic, B. Simonic, and J. Kovac, "Structural properties and antibacterial effects of hydrophobic and oleophobic sol-gel coatings for cotton fabrics," Langmuir, vol. 25, no. 10, pp. 5869–5880, 2009.

[67] T. J. Berger, J. A. Spadaro, S. E. Chapin, and R. O. Becker, "Electrically generated silver ions - quantitative effects on bacterial and mammalian-cells," Antimicrobial Agents and Chemotherapy, vol. 9, no. 2, pp. 357–358, 1976.

[68] Q. L. Feng, J. Wu, G. Q. Chen, F. Z. Cui, T. N. Kim, and J. O. Kim, "A mechanistic study of the antibacterial effect of silver ions on escherichia coli and staphylococcus aureus," Journal of Biomedical Materials Research, vol. 52, no. 4, pp. 662–668, 2000.

[69] J. R. Morones, J. L. Elechiguerra, A. Camacho, K. Holt, J. B. Kouri, J. T. Ramirez, and M. J. Yacaman, "The bactericidal effect of silver nanoparticles," Nanotechnology, vol. 16, no. 10, pp. 2346–2353, 2005.

[70] B. Tomsic, B. Simoncic, B. Orel, L. Cerne, P. F. Tavcer, M. Zorko, I. Jerman, A. Vilcnik, and J. Kovac, "Sol-gel coating of cellulose fibres with antimicrobial and repellent properties," Journal of Sol-Gel Science and Technology, vol. 47, no. 1, pp. 44–57, 2008.

[71] B. Bhushan and Y. C. Jung, "Natural and biomimetic artificial surfaces for superhydrophobicity, self-cleaning, low adhesion, and drag reduction," Progress in Materials Science, vol. 56, no. 1, pp. 1–108, 2011.

[72] M. S. Khalil-Abad and M. E. Yazdanshenas, "Superhydrophobic antibacterial cotton textiles," Journal of Colloid and Interface Science, vol. 351, no. 1, pp. 293–298, 2010.

[73] A. W. Martinez, S. T. Phillips, M. J. Butte, and G. M. Whitesides, "Patterned paper as a platform for inexpensive, low-volume, portable bioassays," Angewandte Chemie, International Edition in English, vol. 46, no. 8, pp. 1318–1320, 2007.

[74] A. W. Martinez, S. T. Phillips, and G. M. Whitesides, "Three-dimensional microfluidic devices fabricated in layered paper and tape," Proceedings of the National Academy of Sciences, USA, vol. 105, no. 50, pp. 19 606–19 611, 2008.

[75] Y. M. Zheng, X. F. Gao, and L. Jiang, "Directional adhesion of superhydrophobic butterfly wings," Soft Matter, vol. 3, no. 2, pp. 178–182, 2007.

[76] L. Feng, Z. Y. Zhang, Z. H. Mai, Y. M. Ma, B. Q. Liu, L. Jiang, and D. B. Zhu, "A super-hydrophobic and super-oleophilic coating mesh film for the separation of oil and water," Angewandte Chemie, International Edition in English, vol. 43, no. 15, pp. 2012–2014, 2004.

[77] W. L. Song, F. Xia, Y. B. Bai, F. Q. Liu, T. L. Sun, and L. Jiang, "Controllable water permeation on a poly(n-isopropylacrylamide)-modified nanostructured copper mesh film," Langmuir, vol. 23, no. 1, pp. 327–331, 2007.

[78] C. X. Wang, T. J. Yao, J. Wu, C. Ma, Z. X. Fan, Z. Y. Wang, Y. R. Cheng, Q. Lin, and B. Yang, "Facile approach in fabricating superhydrophobic and superoleophilic surface for water and oil mixture separation," ACS Applied Materials & Interfaces, vol. 1, no. 11, pp. 2613–2617, 2009.

[79] S. T. Wang, Y. L. Song, and L. Jiang, "Microscale and nanoscale hierarchical structured mesh films with superhydrophobic and superoleophilic properties induced by long-chain fatty acids," Nanotechnology, vol. 18, no. 1, 2007.

[80] S. H. Wang, M. Li, and Q. H. Lu, "Filter paper with selective absorption and separation of liquids that differ in surface tension," Acs Applied Materials & Interfaces, vol. 2, no. 3, pp. 677–683, 2010.

[81] A. K. Sen, Coated Textiles: Principles and Applications. Boca Raton, FL: Taylor & Francis Group, 2008.

[82] W. X. Hou and Q. H. Wang, "Stable polytetrafluoroethylene superhydrophobic surface with lotus-leaf structure," Journal of Colloid and Interface Science, vol. 333, no. 1, pp. 400–403, 2009.

[83] J. N. Israelachvili, Intermolecular and Surface Forces (3rd Edition). Amsterdam: Elsevier, 2010.

[84] Y. L. Chen, C. A. Helm, and J. N. Israelachvili, "Molecular mechanisms associated with adhesion and contact-angle hysteresis of monolayer surface," Journal of Physical Chemistry, vol. 95, no. 26, pp. 10 736–10 747, 1991.

[85] C. F. Wang, T. F. Wang, C. S. Liao, S. W. Kuo, and H. C. Lin, "Using pencil drawing to pattern robust superhydrophobic surfaces to control the mobility of water droplets," Journal of Physical Chemistry, vol. 115, no. 33, pp. 16 495–16 500, 2011.

[86] J. Leopoldes, A. Dupuis, D. G. Bucknall, and J. M. Yeomans, "Jetting micron-scale droplets onto chemically heterogeneous surfaces," Langmuir, vol. 19, no. 23, pp. 9818–9822, 2003.

[87] L. J. Sokoll and D. W. Chan, "Clinical analyzers. immunoassays," Analytical Chemistry, vol. 71, no. 12, pp. 356R–362R, 1999.

[88] S. Ferris, H. Cowles, Jr., and L. Henderson, "Composition of paraffin wax," Industrial and Engineering Chemistry, vol. 21, no. 11, p. 3, 1929.

[89] L. E. Vandenburg and E. Wilder, "The structural constituents of carnauba wax," Journal of the American Oil Chemists' Society, vol. 47, no. 12, p. 514, 1970.

[90] R. Dettre and R. E. JohnsonJr, "Contact angle hysteresis," American Chemical Society, vol. 43, no. 43, pp. 136–144, 1964.

[91] B. Bhushan, M. Nosonovsky, and Y. C. Jung, "Towards optimization of patterned superhydrophobic surfaces," Journal of the Royal Society Interface, vol. 4, no. 15, pp. 643–648, 2007.

[92] E. J. King and R. J. Garner, "The colorimetric determination of glucose," Journal of Clinical Pathology, vol. 1, no. 1, pp. 30–33, 1947.

[93] Y. Liu, Y. H. Xiu, D. W. Hess, and C. P. Wong, "Silicon surface structure-controlled oleophobicity," Langmuir, vol. 26, no. 11, pp. 8908–8913, 2010.

[94] J. M. Xi, L. Feng, and L. Jiang, "A general approach for fabrication of superhydrophobic and superamphiphobic surfaces," Applied Physics Letters, vol. 92, no. 5, p. 053102, 2008.

[95] R. T. R. Kumar, K. B. Mogensen, and P. Boggild, "Simple approach to superamphiphobic overhanging silicon nanostructures," Journal of Physical Chemistry C, vol. 114, no. 7, pp. 2936–2940, 2010.

[96] A. Ahuja, J. A. Taylor, V. Lifton, A. A. Sidorenko, T. R. Salamon, E. J. Lobaton, P. Kolodner, and T. N. Krupenkin, "Nanonails: A simple geometrical approach to electrically tunable superlyophobic surfaces," Langmuir, vol. 24, no. 1, pp. 9–14, 2008.

[97] M. Im, H. Im, J. H. Lee, J. B. Yoon, and Y. K. Choi, "A robust superhydrophobic and superoleophobic surface with inverse-trapezoidal microstructures on a large transparent flexible substrate," Soft Matter, vol. 6, no. 7, pp. 1401–1404, 2010.

[98] Y. Lu, W. W. Shi, L. Jiang, J. H. Qin, and B. C. Lin, "Rapid prototyping of paper-based microfluidics with wax for low-cost, portable bioassay," Electrophoresis, vol. 30, no. 9, pp. 1497–1500, 2009.

[99] H. Jin, M. Kettunen, A. Laiho, H. Pynnonen, J. Paltakari, A. Marmur, O. Ikkala, and R. H. A. Ras, "Superhydrophobic and superoleophobic nanocellulose aerogel membranes as bioinspired cargo carriers on water and oil," Langmuir, vol. 27, no. 5, pp. 1930–1934, 2011.

[100] C. Aulin, J. Netrval, L. Wagberg, and T. Lindstrom, "Aerogels from nanofibrillated cellulose with tunable oleophobicity," Soft Matter, vol. 6, no. 14, pp. 3298–3305, 2010.

[101] C. Aulin, S. H. Yun, L. Wagberg, and T. Lindstrom, "Design of highly oleophobic cellulose surfaces from structured silicon templates," ACS Applied Materials & Interfaces, vol. 1, no. 11, pp. 2443–2452, 2009.

[102] X. L. Wang, H. Y. Hu, Q. Ye, T. T. Gao, F. Zhou, and Q. J. Xue, "Superamphiphobic coatings with coralline-like structure enabled by one-step spray of polyurethane/carbon nanotube composites," Journal of Materials Chemistry, vol. 22, no. 19, pp. 9624–9631, 2012.

[103] M. H. Jin, X. J. Feng, L. Feng, T. L. Sun, J. Zhai, T. J. Li, and L. Jiang, "Superhydrophobic aligned polystyrene nanotube films with high adhesive force," Advanced Materials, vol. 17, no. 16, pp. 1977–+, 2005.

[104] H. J. Lee, C. R. Willis, and C. A. Stone, "Modeling and preparation of a super-oleophobic non-woven fabric," Journal of Materials Science, vol. 46, no. 11, pp. 3907–3913, 2011.

[105] T. Darmanin and F. Guittard, "Super oil-repellent surfaces from conductive polymers," Journal of Materials Chemistry, vol. 19, no. 38, pp. 7130–7136, 2009.

[106] H. Q. Liu, S. Szunerits, W. G. Xu, and R. Boukherroub, "Preparation of superhydrophobic coatings on zinc as effective corrosion barriers," Acs Applied Materials & Interfaces, vol. 1, no. 6, pp. 1150–1153, 2009.

[107] A. Steele, I. Bayer, and E. Loth, "Inherently superoleophobic nanocomposite coatings by spray atomization," Nano Letters, vol. 9, no. 1, pp. 501–505, 2009.

[108] J. Yang, Z. Z. Zhang, X. H. Men, X. H. Xu, and X. T. Zhu, "A simple approach to fabricate superoleophobic coatings," New Journal of Chemistry, vol. 35, no. 3, pp. 576–580, 2011.

[109] W. Choi, A. Tuteja, S. Chhatre, J. M. Mabry, R. E. Cohen, and G. H. McKinley, "Fabrics with tunable oleophobicity," Advanced Materials, vol. 21, no. 21, pp. 2190–2195, 2009.

[110] S. S. Chhatre, A. Tuteja, W. Choi, A. Revaux, D. Smith, J. M. Mabry, G. H. McKinley, and R. E. Cohen, "Thermal annealing treatment to achieve switchable and reversible oleophobicity on fabrics," Langmuir, vol. 25, no. 23, pp. 13 625–13 632, 2009.

[111] B. Leng, Z. Shao, G. de With, and W. Ming, "Superoleophobic cotton textiles," Langmuir, vol. 25, no. 4, pp. 2456–2460, 2009.

[112] A. K. Kota, Y. X. Li, J. M. Mabry, and A. Tuteja, "Hierarchically structured superoleophobic surfaces with ultralow contact angle hysteresis," Advanced Materials, vol. 24, no. 43, pp. 5838–5843, 2012.

[113] H. F. Hoefnagels, D. Wu, G. de With, and W. Ming, "Biomimetic superhydrophobic and highly oleophobic cotton textiles," Langmuir, vol. 23, no. 26, pp. 13 158–13 163, 2007.

[114] S. Michielsen and H. J. Lee, "Design of a superhydrophobic surface using woven structures," Langmuir, vol. 23, no. 11, pp. 6004–6010, 2007.

[115] A. Marmur, "Wetting on hydrophobic rough surfaces: To be heterogeneous or not to be?" Langmuir, vol. 19, no. 20, pp. 8343–8348, 2003.

[116] C. F. Jin, Y. F. Jiang, T. Niu, and J. G. Huang, "Cellulose-based material with amphiphobicity to inhibit bacterial adhesion by surface modification," Journal of Materials Chemistry, vol. 22, no. 25, pp. 12 562–12 567, 2012.

[117] TAPPI, "Laboratory beating of pulp (pfi mill method); t 248 sp-08; tappi (technical association of the pulp and paper industry), peachtree corners, ga," 2008.

[118] D. A. Steenkamer, S. H. McKnight, D. J. Wilkins, and V. M. Karbhari, "Experimental characterization of permeability and fiber wetting for liquid molding," Journal of Materials Science, vol. 30, no. 12, pp. 3207–3215, 1995.

[119] A. Robertson, "Interactions of liquids with cellulose," Tappi, vol. 53, no. 7, pp. 1331–1339, 1970.

[120] M. L. Blow and J. M. Yeomans, "Superhydrophobicity on hairy surfaces," Langmuir, vol. 26, no. 20, pp. 16 071–16 083, 2010.

[121] L. Feng, Y. L. Song, J. Zhai, B. Q. Liu, J. Xu, L. Jiang, and D. B. Zhu, "Creation of a superhydrophobic surface from an amphiphilic polymer," Angewandte Chemie-International Edition, vol. 42, no. 7, pp. 800–802, 2003.

[122] E. Hosono, S. Fujihara, I. Honma, and H. S. Zhou, "Superhydrophobic perpendicular nanopin film by the bottom-up process," Journal of the American Chemical Society, vol. 127, no. 39, pp. 13 458–13 459, 2005.

[123] L. Cao, H.-H. Hu, and D. Gao, "Design and fabrication of micro-textures for inducing a superhydrophobic behavior on hydrophilic materials," Langmuir, vol. 23, no. 8, pp. 4310–4314, 2007.

[124] Y. Ma, X. Cao, X. Feng, Y. Ma, and H. Zou, "Fabrication of super-hydrophobic film from pmma with intrinsic water contact angle below 90 degrees," Polymer, vol. 48, no. 26, pp. 7455–7460, 2007.

[125] Y. T. Cheng and D. E. Rodak, "Is the lotus leaf superhydrophobic?" Applied Physics Letters, vol. 86, no. 14, p. 144101, 2005.

[126] A. Grill, "Diamond-like carbon: state of the art," Diamond and Related Materials, vol. 8, no. 2-5, pp. 428–434, 1999.

[127] J. Robertson, "Diamond-like amorphous carbon," Materials Science & Engineering R-Reports, vol. 37, no. 4-6, pp. 129–281, 2002.

[128] S. C. H. Kwok, W. Jin, and P. K. Chu, "Surface energy, wettability, and blood compatibility phosphorus doped diamond-like carbon films," Diamond and Related Materials, vol. 14, no. 1, pp. 78–85, 2005.

[129] J. H. Kim, G. M. Liu, and S. H. Kim, "Deposition of stable hydrophobic coatings with in-line ch4 atmospheric rf plasma," Journal of Materials Chemistry, vol. 16, no. 10, pp. 977–981, 2006.

[130] N. J. Shirtcliffe, G. McHale, M. I. Newton, and Y. Zhang, "Superhydrophobic copper tubes with possible flow enhancement and drag reduction," ACS Applied Materials & Interfaces, vol. 1, no. 6, pp. 1316–1323, 2009.

[131] J. Ou and J. P. Rothstein, "Direct velocity measurements of the flow past drag-reducing ultrahydrophobic surfaces," Physics of Fluids, vol. 17, no. 10, p. 103606, 2005.

[132] C. H. Choi and C. J. Kim, "Large slip of aqueous liquid flow over a nanoengineered superhydrophobic surface," Physical Review Letters, vol. 96, no. 6, p. 066001, 2006.

[133] M. L. Ma and R. M. Hill, "Superhydrophobic surfaces," Current Opinion in Colloid and Interface Science, vol. 11, no. 4, pp. 193–202, 2006.

[134] K. S. Liu and L. Jiang, "Metallic surfaces with special wettability," Nanoscale, vol. 3, no. 3, pp. 825–838, 2011.

[135] W. C. Wu, M. Chen, S. Liang, X. L. Wang, J. M. Chen, and F. Zhou, "Superhydrophobic surface from cu-zn alloy by one step o-2 concentration dependent etching," Journal of Colloid and Interface Science, vol. 326, no. 2, pp. 478–482, 2008.

[136] B. Wu, M. Zhou, J. Li, X. Ye, G. Li, and L. Cai, "Superhydrophobic surfaces fabricated by microstructuring of stainless steel using a femtosecond laser," Applied Surface Science, vol. 256, no. 1, pp. 61–66, 2009.

[137] H. M. Cobb, The History of Stainless Steel. Materials Park: ASM International, 2010.

[138] H. S. Khatak and R. Baldev, Corrosion of Austenitic Stainless Steel: Mechanism, Mitigation and Monitoring. Materials Park: ASM International, 2002.

[139] A.-M. Kietzig, S. G. Hatzikiriakos, and P. Englezos, "Patterned superhydrophobic metallic surfaces," Langmuir, vol. 25, no. 8, pp. 4821–4827, 2009.

[140] M. Groenendijk and J. Meijer, "Microstructuring using femtosecond pulsed laser ablation," Journal of Laser Applications, vol. 18, no. 3, pp. 227–235, 2006.

[141] L. J. Chen and J. W. Zhao, "Preparation of cu-coated stainless steel surfaces for superhydrophobic investigation," Journal of Dispersion Science and Technology, vol. 31, no. 9, pp. 1245–1248, 2010.

[142] L. J. Chen, M. Chen, H. D. Hui, and J. M. Chen, "Preparation of super-hydrophobic surface on stainless steel," Applied Surface Science, vol. 255, no. 5, pp. 3459–3462, 2008.

[143] J. P. Youngblood and T. J. McCarthy, "Ultrahydrophobic polymer surfaces prepared by simultaneous ablation of polypropylene and sputtering of poly(tetrafluoroethylene) using radio frequency plasma," Macromolecules, vol. 32, no. 20, pp. 6800–6806, 1999.

[144] N. J. Yu, Y. F. Yu, Y. F. Li, S. P. Song, S. B. Huo, and X. Y. Han, "Preparation and characterization of super-hydrophobic surfaces on aluminum and stainless steel substrates," Surface Review and Letters, vol. 17, no. 3, pp. 375–381, 2010.

[145] H. L. Xu, Y. Li, D. Q. Jiang, and X. P. Yan, "Hydrofluoric acid etched stainless steel wire for solid-phase microextraction," Analytical Chemistry, vol. 81, no. 12, pp. 4971–4977, 2009.

[146] L. S. Zhong, J. S. Hu, H. P. Liang, A. M. Cao, W. G. Song, and L. J. Wan, "Self-assembled 3d flowerlike iron oxide nanostructures and their application in water treatment," Advanced Materials, vol. 18, no. 18, pp. 2426–2431, 2006.

[147] R. D. Hazlett, "Fractal applications - wettability and contact-angle," Journal of Colloid and Interface Science, vol. 137, no. 2, pp. 527–533, 1990.

[148] K. M. Forsberg and A. C. Rasmuson, "Crystallization of metal fluoride hydrates from mixed hydrofluoric and nitric acid solutions, part i, iron (iii) and chromium (iii)," Journal of Crystal Growth, vol. 312, no. 16-17, pp. 2351–2357, 2010.

[149] L. F. Chen, Z. Song, X. Wang, S. V. Prikhodko, J. C. Hu, S. Kodambaka, and R. Richards, "Three-dimensional morphology control during wet chemical synthesis of porous chromium oxide spheres," ACS Applied Materials & Interfaces, vol. 1, no. 9, pp. 1931–1937, 2009.

[150] J. L. Galvez, J. Dufour, C. Negro, and F. Lopez-Mateos, "Determination of iron and chromium fluorides solubility for the treatment of wastes from stainless steel mills," Chemical Engineering Journal, vol. 136, no. 2-3, pp. 116–125, 2008.

[151] T. V. Rao, R. W. Vook, W. Meyer, and A. Joshi, "Effect of surface treatments on near-surface composition of 316-nuclear grade stainless-steel," Journal of Vacuum Science & Technology A, vol. 4, no. 3, pp. 1604–1607, 1986.

[152] B. Craig and D. Anderson, Handbook of Corrosion Data. Materials Park: ASM International, 1995.

[153] C. K. Gupta, Extractive Metallurgy of Molybdenum. Boca Raton: CRC Press, 1992.

[154] G. Kreysa and M. Schtze, Eds., DECHEMA Corrosion Handbook - Revised and Extended 2nd Edition. Frankfurt: DECHEMA, 2008.

[155] M. Mayuzumi, J. Ohta, and T. Arai, "Effects of cold work, sensitization treatment, and the combination on corrosion behavior of stainless steels in nitric acid," Corrosion, vol. 54, no. 4, pp. 271–280, 1998.

[156] M. Hadji and R. Badji, "Microstructure and mechanical properties of austenitic stainless steels after cold rolling," Journal of Materials Engineering and Performance, vol. 11, no. 2, pp. 145–151, 2002.

[157] A. Delimi, E. Galopin, Y. Coffinier, M. Pisarek, R. Boukherroub, B. Talhi, and S. Szunerits, "Investigation of the corrosion behavior of carbon steel coated with fluoropolymer thin films," Surface & Coatings Technology, vol. 205, no. 16, pp. 4011–4017, 2011.

[158] J. S. Chen, S. P. Lau, Z. Sun, G. Y. Chen, Y. J. Li, B. K. Tay, and J. W. Chai, "Metal-containing amorphous carbon films for hydrophobic application," Thin Solid Films, vol. 398, pp. 110–115, 2001.

[159] H. W. Choi, R. H. Dauskardt, S. C. Lee, K. R. Lee, and K. H. Oh, "Characteristic of silver doped dlc films on surface properties and protein adsorption," Diamond and Related Materials, vol. 17, no. 3, pp. 252–257, 2008.